Nanoplasmonics with Dispersive and Lossy Media

by

Ryan Peck

B.Sc., University of the Fraser Valley, 2015

M.Sc., University of Windsor, 2017

A Dissertation Submitted in Partial Fulfillment of the

Requirements for the Degree of

DOCTOR OF PHILOSOPHY

in the Department of Physics and Astronomy

Nanoplasmonics with Dispersive and Lossy Media

by

Ryan Peck

B.Sc., University of the Fraser Valley, 2015

M.Sc., University of Windsor, 2017

Supervisory Committee

Dr. Reuven Gordon, Co-Supervisor
(Department of Physics and Astronomy)

Dr. Alex Brolo, Co-Supervisor
(Department of Physics and Astronomy)

Dr. Irina Paci, Outside Member
(Department of Chemistry)

ABSTRACT

This thesis focuses on the physics of nanoplasmonic systems for dispersive and lossy media. Gold nanoparticles in P3HT (poly(3-hexylthiophene)) and PMMA (poly(methyl methacrylate)) are analyzed both theoretically and experimentally. It is found in both cases that the presence of P3HT narrows the linewidth of the gold plasmon peak. This is a counter-intuitive result, and this narrowing of the linewidth by a lossy material is analyzed in detail. It is found that dispersion in both the real and imaginary parts of the permittivity of the surrounding medium can significantly affect the linewidth. Another plasmonic phenomena was also researched. An atomic energy level model of erbium was constructed and used to solve a rate equation to calculate the far-field emission enhancement from an erbium atom nearby a gold nanorod when the dark mode is excited. Normally a small emission enhancement is expected in the far field since dark modes do not couple strongly to radiation, but in experiments this dark field emission enhancement was seen to be significant [1]. The results of the calculation were compared to this previous experimental result. Although the incident power dependence of the calculated 980 nm emission line agreed with experiments, the 650 nm emission line power dependence and the calculated emission enhancement did not, and so more work needs to be done with this model to explain the experimental results.

Contents

Supervisory Committee **ii**

Abstract **iii**

Table of Contents **iv**

List of Tables **viii**

List of Figures **xi**

List of Abbreviations **xxv**

Acknowledgements **xxvi**

1 Introduction **1**

1.1 Introduction 1

1.1.1 History of Light and Nanotechnology 1

1.1.2 Achievements of Nanotechnology 10

1.1.3 Plasmonic Solar Cells 14

1.2 Motivation 16

1.3 Agenda 17

2 Literature Review **19**

2.1 Nanoplasmonic linewidth 19

2.2 Reducing Linewidths 29

2.3 Loss in Plasmonics 32

2.4 Mie Theory in Lossy Media 33

2.5 Dispersion in Nanoplasmonics 39

3 Theory **42**

3.1 Drude-Lorentz Model 42

3.1.1 Plasmons 46

3.1.2 Dispersion and Loss 52

3.1.3 Linewidth 56

3.1.4 Extinction 57

3.2 Scattering in Lossy Dispersive Media 63

3.3 Circuit Model for Lossy Dispersive Media 67

3.4 Green Function Theory 70

3.5 Green Function Analysis 72

3.5.1 Perovskite Green Function Analysis 82

3.5.2 Organic Photovoltaics 84

3.5.3 Erbium Upconversion Enhancement 89

3.6 Conclusion 94

4 Simulations **97**

4.1 Gold Nanoparticle Scattering in P3HT 97

4.2 Nanorod Emission Enhancement 104

4.3 Conclusion 107

5 Experiments **108**

5.1 Sample Preparation 108

5.2 Measurements 110

5.3 Conclusion 125

6 Conclusions **126**

6.1 Conclusions 126

6.2 Comparisons 128

6.3 Future Work 133

A Additional Information **137**

A.1 Linewidth Dependence on Metal Properties 137

A.2 Electron-Phonon Relaxation Rate 141

A.3 Finite Thickness Embedding Media 147

A.4 Nanoparticle Size 148

A.5 Nanoparticle Permittivity 150

A.6 P3HT Scattering Data 154

A.7 Un-normalized Scattering Spectra 155

A.8 Kramers-krönig Relations 155

Bibliography **157**

List of Tables

Table 3.1 Summary of plasmon peaks calculated from Green function spectra for 20 nm gold in various infinite and homogeneous embedding media. The scattering spectra for the permittivities listed in this table were calculated using Mie series expansions. When only five terms were used in the series expansions, the resulting linewidths were accurate to three decimal digits. The displayed linewidths were calculated using 23 terms and there is negligible numerical error in these values. 75

Table 3.2 Summary of plasmon peaks calculated from Green function spectra for 20 nm gold in different perovskites. The scattering spectra for the permittivities listed in this table were calculated using Mie series expansions. 82

Table 3.3 These were the values of the coefficients in the rate equation used to calculate the plasmonic enhancement factor at the bright and dark modes. The values shown here are the coefficient values before modification from field enhancement of the bright and dark modes. 96

Table 6.1 Linewidths calculated for 20 nm gold nanoparticles in PMMA and P3HT for each different method used in this thesis. 126

Table A.1 Summary of plasmon peak data from Fig A.1 (a) for a 20 nm gold nanoparticle in layers of PMMA of various thickness. . . 148

Table A.2 Summary of plasmon peak data from Fig A.1 (b) for a 20 nm gold nanoparticle in layers of P3HT of various thickness. . . . 148

Table A.3 Summary of plasmon peak data from Fig A.2 (a) for different size gold nanoparticles in PMMA. 149

Table A.4 Summary of plasmon peak data from Fig A.2 (b) for a different size gold nanoparticles in P3HT. 150

Table A.5 Summary of plasmon peaks calculated from Green function spectra for various gold-like metals in infinite and homogeneous PMMA. A row marked with 'X' means there was no plasmon peak for this calculation. The constant values of -5.23 and $1.97i$ were used because at the plasmon peak for gold and PMMA the permittivity of gold is $\epsilon_{\text{gold}} = -5.23 + 1.97i$. . . . 151

Table A.6 Summary of plasmon peaks calculated from Green function spectra for various gold-like metals in infinite and homogeneous P3HT. A row marked with 'X' means there was no plasmon peak for this calculation. The constant values of -13.3 and $1.02i$ were used because at the plasmon peak for gold and P3HT the permittivity of gold is $\epsilon_{\text{gold}} = -13.3 + 1.02i$. 151

List of Figures

Figure 1.1 Lycurgus cup [2]. In the left image, the light source is on the same side as the camera, and green reflected light is seen. In the right image, the light source and camera are on opposite sides of the cup, and red transmitted light is seen. The difference in colour between the two images is due to the presence of metal nanoparticles in the cup. 2

Figure 1.2 "IBM" spelled out with xenon atoms [3]. 4

Figure 1.3 Microwave negative index metamaterial, made of split-ring resonators and silver wires [4]. 11

Figure 1.4 Schematic showing how SERS works [5]. 12

Figure 1.5 Molecules can be trapped by focusing a laser focused to a point, yielding a large intensity gradient [6]. 13

Figure 1.6 Particles or nanostructures can be added at any place in the cell, each increasing power conversion efficiency by a different method [7]. (a) Large particles at the top increase scattering in the cell. (b) Small particles inside the absorbing layer increase absorption. (c) nanostructuring of the bottom contact keeps light trapped in the absorbing layer. 14

Figure 3.1 Equivalent circuit for a metal nanosphere in an infinite homogeneous medium. The role of the AC current source is adopted by the displacement current resulting from the oscillating incident light. 50

Figure 3.2 Relative permittivities of gold, P3HT, and PMMA. (a) The real permittivities. The vertical solid blue line corresponds to the plasmon resonance of gold and P3HT at 612 nm determined from the Clausius-Mossotti factor described below. The vertical dashed red line corresponds to the plasmon resonance of gold and PMMA at 514 nm determined from the Clausius-Mossotti factor. (b) The imaginary permittivities. The imaginary part of the permittivity of PMMA is nearly zero. 62

(a) 62

(b) 62

Figure 3.3 Cross Sections from Rayleigh scattering formulas, Eqs. (3.32)-(3.35). (a) The absorption cross section of a 10 nm gold sphere embedded in P3HT and 10 nm gold in PMMA. (b) The scattering cross section of a 10 nm gold sphere embedded in P3HT and 10 nm gold in PMMA. For both (a) and (b) the vertical solid blue line represents the gold and P3HT plasmon resonance and the vertical dashed red line shows the gold and PMMA plasmon resonance. The black horizontal double arrow lines show the full width at half the maximum of each of the peaks. The gold nanoparticle has a geometric cross section of 7.85×10^{-17} m^2 (πa^2 for a 10 nm diameter gold nanoparticle). 63

(a) 63

(b) 63

Figure 3.4 Extinction cross section of a 10 nm gold nanoparticle in P3HT. 66

Figure 3.5 Equivalent nanocircuit for a metal nanoparticle surrounded by a lossy medium. The resistances in the circuit are associated with the material loss. If neither material is lossy then the resistances are 0. 67

Figure 3.6 Optical absorption results of a nanocircuit consisting of a 10 nm gold sphere inductor surrounded by a P3HT capacitor. (a) The power absorbed by each circuit element, normalized by the square of the incident field strength $|\mathbf{E}_0|^2$. (b) The ratio of the power absorbed in P3HT to the power absorbed in gold. . 67

(a) 67

(b) 67

Figure 3.7 Green function and permittivity data for P3HT and PMMA. (a) Green function spectrum S for a single 20 nm gold nanoparticle in P3HT and PMMA. Surrounding media are assumed to be infinite and homogeneous. (b) Real and imaginary parts of the permittivity of P3HT and PMMA. 72

(a) 72

(b) 72

Figure 3.8 Green function spectrum S for a 20 nm gold nanoparticle in various infinite and homogeneous embedding media. The permittivities of the embedding media are: $\epsilon_1 = \epsilon_{\mathrm{P3HT}}$, $\epsilon_2 = 5.2+\mathrm{Im}\{\epsilon_{\mathrm{P3HT}}\}i$, $\epsilon_3 = \mathrm{Re}\{\epsilon_{\mathrm{P3HT}}\}+1.5i$, $\epsilon_4 = 5.2+1.5i$, $\epsilon_5 = 5.2$ and $\epsilon_6 = \mathrm{Re}\{\epsilon_{\mathrm{P3HT}}\}$. The data is summarized in table 3.1 . . . 74

(a) 76

(b) 76

(c) 76

(d) 76

Figure 3.8 Effect of sharpness of semiconductor band edges on the linewidth of a plasmon peak. Band edges assumed to be linear for simplicity. All cross sections are calculated with Rayleigh scattering theory for a 10 nm gold nanoparticle. (a) Rayleigh scattering cross section of a 10 nm gold nanoparticle in a semiconductor with a broad band edge. The linewidth is 57 nm. (b) Real and imaginary parts of the permittivity of the broad band edge semiconductor. (c) Rayleigh scattering cross section of a 10 nm gold nanoparticle in a material with a sharp band edge. The linewidth is 32 nm. (d) Real and imaginary parts of the permittivity of the sharp band edge semiconductor.(e) Rayleigh scattering cross section of a 10 nm gold nanoparticle in a material with a very sharp band edge. The linewidth is 17 nm. (f) Real and imaginary parts of the permittivity of the very sharp band edge semiconductor. (g) Rayleigh scattering cross section of a 10 nm gold nanoparticle in a lossless dielectric. The linewidth is 32 nm. This is a broader linewidth than the very sharp band edge semiconductor. (h) Real and imaginary parts of the permittivity of the lossless dielectric. The real permittivity is 5 and the imaginary part is 0. 77

(e) 77

(f) 77

(g) 77

Figure 3.9 Permittivities of different perovskites. (a) Real permittivities. (b) Imaginary permittivities. 82

(a) 82

(b) 82

Figure 3.10 Green function spectrum S for a 20 nm gold nanoparticle in perovskites. The data is summarized in table 3.2. 83

Figure 3.11 The model used to solve the rate equation for the erbium atom. The W's represent spontaneous emission, the S's are either 1520, or 1210 nm stimulated emission and absorption, and the C's are co-operative upconversion terms. The red circles show which levels the co-operative upconversion process occurs. . . 91

Figure 3.12 A comparison between the experimental results from [1] and the rate equation model used here for 1520 nm excitation only, and simultaneous 1520 nm and 1210 nm excitation. (a) Rate equation results for 1520 nm excitation. (b) Experimental results for only 1520 nm excitation. (c) Rate equation results for 1520 and 1210 nm dual excitation. (d) Experimental results for 1520 and 1210 nm dual excitation. 93

Figure 3.13 Enhancement of emission of erbium atoms due to the presence of gold nanorods at the bright and dark modes. 94

Figure 4.1 2D representation of the layout of the FDTD simulations used for this work. 97

Figure 4.2 Cross Sections calculated from FDTD simulations. The black horizontal double arrow lines show the full width at half the maximum of each of the peaks. (a) The absorption cross sections of a single 10 nm gold sphere in P3HT and PMMA. (b) The scattering cross sections of a single 10 nm gold sphere in P3HT and PMMA. 98

(a) 98

(b) 98

Figure 4.3 FDTD numerical simulation data. (a) A schematic of the FDTD simulation. The blue box is a 120 nm thick layer of PMMA, with a 20 nm diameter gold nanoparticle in the center. The large orange box is the simulation region, the small pink box is the TFSF source and it is contained in the blue box and contains the gold nanoparticle. The yellow square is the field monitor where the scattered field was measured. (b) Scattering cross section calculated with FDTD from a 20 nm gold nanoparticle in a 120 nm thick PMMA layer and a 120 nm thick P3HT layer. 102

(a) 102

(b) 102

Figure 4.4 Schematic of the FDTD simulation. The orange box is the simulation boundaries, the yellow boxes are transmission monitors. There are two transmission boxes, one is small and surrounds only the dipole source, and the other is nearly as large as the simulation region, and surrounds both the dipole source and the gold nanorod. The dipole source was placed 10 nm from the tip of the gold nanorod and used an incident wavelength of 300-1500 nm. 105

Figure 4.5 Field profiles of the bright and dark modes of the gold nanorods used in experiments. (a) Bright mode at 980 nm. (b) Dark mode at 600 nm. 106

(a) 106

(b) 106

Figure 4.6 FDTD simulation results for the radiative and Purcell Enhancement factors of a dipole source nearby a gold nanorod. (a) Radiative enhancement factor. (b) Purcell Factor. 106

(a) 106

(b) 106

Figure 5.1 (a)-(d) Sample Preparation. (a) Spin coat bottom layer. (b) Drop coat gold nanoparticles. (c) Spin coat top layer. (d) Gold nanoparticles encased in thin layer of surrounding material. . . 109

Figure 5.2 20 nm spherical gold nanoparticles drop coated on a glass slide and imaged with a CytoViva dark field microscope. 110

Figure 5.3 10 nm gold in 100 nm thick PMMA. 111

Figure 5.4 TEM images of gold nanoparticles. (a) 20 nm gold nanoparticles. (b) 60 nm gold nanoparticles. (c) 100 nm gold nanoparticles. 111

(a) 111

(b) 111

(c) 111

Figure 5.5 20 nm gold nanoparticles. 112

Figure 5.6 60 nm gold nanoparticles. 113

Figure 5.7 100 nm gold nanoparticles. 113

Figure 5.8 Individual 20 nm gold nanoparticle spectrum. 113

Figure 5.9 Individual 60 nm gold nanoparticle spectrum. 114

Figure 5.10 Individual 100 nm gold nanoparticle spectrum. 114

Figure 5.11 20 nm gold nanoparticles in PMMA. 115

Figure 5.12 60 nm gold nanoparticles in PMMA. 115

Figure 5.13 Individual 20 nm gold in PMMA spectrum. 115

Figure 5.14 Individual 60 nm gold in PMMA spectrum. 116

Figure 5.15 20 nm gold nanoparticles in P3HT. 117

Figure 5.16 60 nm gold nanoparticles in P3HT. 117

Figure 5.17 A 20 nm layer of P3HT. The layer is no longer uniform. The optical properties are different from those of thicker layers because when the P3HT molecules are this spread, they cannot form a j-aggregate structure. 117

Figure 5.18 A 240 nm layer of P3HT. The fluorescence dominates the scattering signal and gold nanoparticles become difficult to see. . . 118

Figure 5.19 Individual 20 nm gold in P3HT spectrum. 118

Figure 5.20 Individual 60 nm gold in P3HT spectrum. 118

Figure 5.21 Change in spectra across a single isolated 60 nm nanoparticle. 119

Figure 5.22 Measured scattering spectrum at different points for the above individual 60 nm nanoparticle. 119

Figure 5.23 Schematic of the AOTF dark field microscope. 120

Figure 5.24 Scattering data collected from the AOTF dark field microscope. The circles on the plots correspond to measured scattering data and occur in 5 nm steps. The position of the plasmon peak and the FWHM are displayed on each plot. (a) Scattered power of 20 nm gold nanoparticles in PMMA. (b) Scattered power of 20 nm gold nanoparticles in P3HT. 123

(a) 123

(b) 123

Figure A.1 FDTD results for the power scattered from a 20 nm gold nanoparticle in films of finite thickness. (a) FDTD results for the power scattered from a 20 nm gold nanoparticle embedded in PMMA films. (b) FDTD results for the power scattered from a 20 nm gold nanoparticle embedded in P3HT films. 147

(a) 147

(b) 147

Figure A.2 Green function calculations for scattered power from a single gold nanoparticle in an infinite and homogeneous surrounding medium. In each plot, the numbers in the legend display the gold nanoparticle diameters. (a) Scattering spectrum for gold nanoparticles of varying diameter embedded in PMMA. (b) Scattering spectrum for gold nanoparticles of varying diameter embedded in P3HT. 149

(a) 149

(b) 149

Figure A.3 Green function spectrum S for various 20 nm metal nanoparticles embedded in infinite and homogeneous PMMA. (a) Scattering spectrum for metal nanoparticles in PMMA. (b) Scattering spectrum for metal nanoparticles in P3HT. Tables A.5 and A.6 show the metal nanoparticle permittivities and summarize the results shown in these figures. 150

(a) 150

(b) 150

Figure A.4 Scattered power spectrum from a 120 nm layer of P3HT. The red circles are experimental measurements taken in 5 nm increments. 154

Figure A.5 Green theory scattered power for PMMA and P3HT without normalization. 155

List of Abbreviations

acousto-optic tuneable filter	AOTF
atomic force microscope	AFM
bulk heterojunction	BHJ
discrete dipole approximation	DDA
electron energy loss spectroscopy	EELS
femtosecond	fs
finite-difference time-domain	FDTD
focused ion beam	FIB
figure of merit	FOM
full-width at half max	FWHM
highest occupied molecular orbital	HOMO
lowest unoccupied molecular orbital	LUMO
localized surface plasmon	LSP
localized surface plasmon resonance	LSPR
nanometer	nm
numerical aperture	NA
organic photovoltaics	OPV
perfectly matched layer	PML
simple harmonic oscillator	SHO
surface plasmon polariton	SPP
scanning tunneling microscope	STM
transverse electric	TE
transverse magnetic	TM
total-field scattered-field	TFSF

ACKNOWLEDGEMENTS

I would like to thank:

My supervisors, Alex Brolo and Reuven Gordon for their time, facilities and their wisdom and guidance. My colleagues and friends in the Brolo and Gordon labs. I've never had such good company for tennis, tea and drinks! Lastly, I would like to thank my family for their relentless support and the faith they had in me. We are the sum of those important people in our lives and I am so lucky to be surrounded by great people.

Chapter 1

Introduction

1.1 Introduction

1.1.1 History of Light and Nanotechnology

Nanotechnology is a relatively new field of research that involves the manipulation of matter on the nanoscale (1-100 nm). Norio Taniguchi coined the term "nanotechnology" in 1974 [8]. He defined nanotechnology as the process of separation, consolidation, and deformation of materials by one atom or one molecule. Nobel Prize laureate, Richard Feynman, was among the first scientists to consider the possibility of operational molecular scale machines, and is often attributed with being the father of nanotechnology. He gave a lecture in 1959 titled, "There's Plenty of Room at the Bottom", in which he described various nanoscale devices [9]. Feynman joked about how these tiny machines might not have any practical applications, and

spending any time thinking about them is only for entertaining our curiosity. Nanotechnology has come a long way since then, and is now a major field of scientific research with billions of dollars of funding available. Nanotechnology has a wide range of applications in physics [9, 10, 11, 12], materials science [13, 14, 15], engineering [16, 17, 18, 19], medicine [20, 21, 22, 23], chemistry [24, 25, 26, 27], and computer science [28, 29, 30, 31]. The United States and China boast the largest number of annual nanotechnology publications; in 2020, China published 40% of all nanotechnology related papers, while the United States published 12% [32]. Nanotechnology is still a rapidly growing field; nearly 9% of all scientific publications in 2020 pertained to nanotechnology [32]. In the United States, the National Nanotechnology Initiative (NNI), has raised 31 billion USD towards funding nanotechnology research since it was created in 2000 [33].

Figure 1.1: Lycurgus cup [2]. In the left image, the light source is on the same side as the camera, and green reflected light is seen. In the right image, the light source and camera are on opposite sides of the cup, and red transmitted light is seen. The difference in colour between the two images is due to the presence of metal nanoparticles in the cup.

People have been using nanotechnology for many centuries. The Lycurgus cup is

probably the most famous example of old age nanotechnology. This vibrant cup was made in the 4th century CE and is held in the British Museum today in London, England. The colour of the cup can appear to be red or green depending on if the light is being reflected or absorbed before it reaches the viewer's eyes. This interesting feature is a result of the composition of the cup. A special glass is used to make the cup, which contains silver and gold alloyed nanoparticles about 70 nm in size. These nanoparticles reflect and absorb green light, and so when shining a light source on the front of the cup, the cup appears green as the reflected light as seen. When lit from the back, the cup will appear red, as most of the green light is absorbed by the cup. The Lycurgus cup is not the only example of ancient nanotechnology. Starting from the 4th century CE, churches and cathedrals used stainless glass windows with gold and silver nanoparticles in the glass, which allowed for a wide range of colour. Glass-makers during this time knew that adding gold chloride or silver nitride to molten glass would result in a colour change to the glass, although they didn't know about the nanoscale science that was responsible for these colour changes.

Gerd Binnig and Heinrich Rohrer developed the scanning tunneling microscope (STM) in 1981 at IBM, for which they later shared the Nobel Prize in physics. This was a huge leap forward for nanotechnology because the STM allowed for imaging on the nanoscale, and the manipulation of individual atoms in a material. Before the development of electron microscopes such as the scanning electron microscope (SEM) and tunneling electron microscope (TEM), light microscopes were used for

imaging. Light microscopes were incredibly successful for viewing small objects only micrometers in size, like bacteria and human hairs, but could not resolve images in the nanoscale range. This is due to the diffraction limit, which gives an inherent limit to the resolution of the light microscope. The ubiquitous estimator for the resolution of a light microscope is one half wavelength of the light transmitting through the microscope. It is difficult to use higher frequency light for imaging for a number of reasons, and so most light microscopes use visible light and are restricted to resolutions of about half a micrometer. Thus, the electron microscopes could bypass the diffraction limit of light microscopes and image incredibly small objects that were never seen clearly before. In 1989, IBM used a scanning tunneling electron microscope (STM)

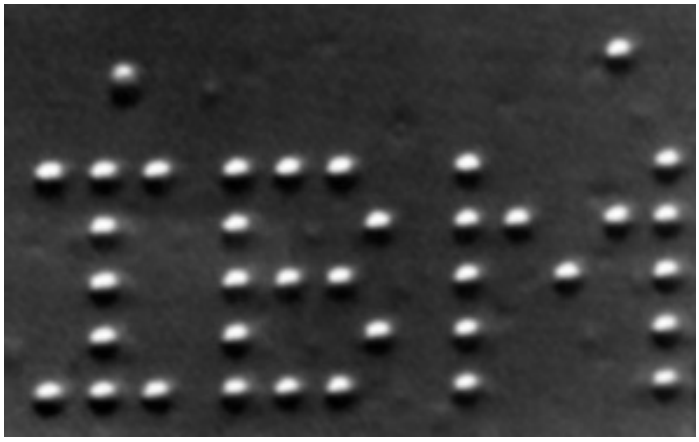

Figure 1.2: "IBM" spelled out with xenon atoms [3].

to position 35 individual xenon atoms to form their company logo. This was the first time ever that matter had been manipulated on such a small scale. Since the creation of the STM, other microscopes and machines have been developed, such as the atomic force microscope (AFM) and focused ion beam (FIB) that have been pivotal to pro-

gressing nanotechnology. With many tools available for imaging and manipulation on the nanoscale, the last few decades has seen a tremendous amount of achievements in nanotechnology. One of the most influential and ground-breaking achievements was the discovery of carbon nanotubes by Suumo Iijima in 1991 [34]. These nanotubes have large mechanical strength, and large electrical and thermal conductivities and are also commonly used as a drug delivery system. In 1997 the first nanotechnology focused company, Zyvex, was formed. The company still operates today and creates products, such as quantum computers, with atomic scale precision. In 2000 Carlo Montemagno made the first molecular motor [19]. The motor consisted of an ATP body with nickel propellers that could spin at about eight revolutions per second. In 2018, Lulu Qian created the smallest game of tic-tac-toe ever played by manipulating long strands of DNA molecules to form the x's and o's [35]. Computer chips are now made with transistors that are only 70 silicon atoms wide, and this was made possible with advancements in nanofabrication. With such a formidable list of achievements in its relatively short lifetime, it is exciting to think about what else the future of nanotechnology could bring.

Much of the magic of nanotechnology involves the interaction of nanostructures with light. A large portion of the progress in nanotechnology has come from the success of scientists to understand what light really is and how it interacts with nanoscale objects. Countless technologies such as solar cells, LEDs, fluorescence microscopy, light microscopes, x-ray imaging, radios, telescopes, GPS sensors, and

lasers, have all been made possible by developing our understanding of light.

People have been fascinated by light for many millennia and many great scientists have become immortalized from their efforts in understanding the properties of light. The first people in recorded history to attempt to understand light were the philosophers of ancient Greece in the 4th century BC. The Greeks were interested in sight, and the predominant theory for the next thousand years was based off of Plato's idea that eyes emit rays and when these rays make contact with an object, they would produce an image. Ptolemy studied the refraction of light travelling between two media and found that the angle of incidence and angle of refraction had a linear relationship, which is true for small angles of refraction. In the 980's, Ibn Sahl derived the law of refraction, which is also known as Snell's law, over 600 years before Willebrord Snellius re-derived it in 1621 [36]. Ibn Sahl also worked with curved mirrors and lenses and found how to shape them to focus light to a point. Alhazen rejected Ptolemy's idea that images are formed from rays emitted from the eyes, and stated that they are actually formed by rays emitted from the objects which then enter the eye. Al Buruni and Avicenna were the first to posit that light must have a finite speed, and even proposed ideas of how to measure it. Isaac Newton experimented with separating light into colours using prisms and showed that white light is constructed from coloured light and that each colour acted independently from each other, refracting through the prism at a different angle.

Newton believed that light was made of tiny corpuscles. He thought that matter

was made of larger corpuscles, and light and matter could freely change into each other. Christiaan Huygens disagreed with Newton's views on the nature of light, claiming light was a wave. The wave theory of light was able to account for the diffraction patterns noticed by Francesco Grimaldi, where Newtons' corpuscular theory failed. The wave theory of light was further enforced by Young's double slit experiment in 1802. Light was diffracted through a barrier with two slits and an interference pattern could clearly be seen by a screen behind the slits. The logical conclusion at the time was that the presence of the interference pattern would only be possible if light behaved like a wave and not a particle. Until the 19th century, electricity, magnetism, and optics were all regarded as separate fields of research. Michael Faraday and James Clerk Maxwell showed that these fields were intrinsically linked together by the concept of electromagnetic fields. In the early 20th century, it was well-known that the classical view of light as a wave failed to explain the radiation spectrum of a perfectly absorbing black body. Theory predicted unbounded electromagnetic radiation from a black body for high frequencies, however it was known at the time from experiments, that there was always a peak. This discrepancy between the classical theory of black-body radiation and the experimental results is known as the UV-catastrophe. Solving the UV-catastrophe was instrumental to the birth of quantum mechanics, and the progression of our understanding of light. Max Planck noticed that if the electromagnetic energy stored in the material of the cavity was discretized in units $E = nh\nu$ where n is an integer, h is now known as Planck's constant,

and ν is the frequency of the light, then he could recover the experimental results of black-body radiation spectrum [37]. Planck assumed that it was the oscillators which had the discrete energy. Einstein later adapted Planck's idea of discretizing energy in a system and applied that to the electromagnetic field directly. This was the birth of the photon and using this new concept Einstein explained the photoelectric effect, which classical electromagnetism could not explain [38]. The photoelectric effect was seen first in experiments and is the dependence of the number of electrons ejected from a metal on the frequency of incident light, and not the intensity of the incident light as classical electromagnetism expected. In 1921, Einstein was awarded the Nobel Prize in physics for explaining the photoelectric effect.

From the efforts of many great scientists, there is a great deal we understand about light today. Light is both a particle and a wave, moving at some large, finite speed, the speed of light, which is the fastest anything can move. It is electromagnetic radiation, a propagating time-dependent electric and magnetic field, which can even move through a vacuum without the need for a medium. Although light is massless, it still has momentum and kinetic energy, which is dependent on the frequency of these electromagnetic fluctuations. These different frequencies are the different colours of light, which Newton saw when he separated and recombined these colours from white light using his prism experiment.

The work in this thesis is based around the interactions of light with small nanoparticles. The light scattered from these nanoparticles can be measured and can have

peaks in the scattered spectra referred to as plasmon peaks. Light-matter interactions at the nanoscale are usually treated classically, using Maxwell's equations. In most cases, there are enough atoms making up nanostructures that their discrete interactions can be averaged, and the nanostructures can be treated as a single homogeneous structure. When nanostructures are reduced below about one hundred atoms, quantum effects are necessary to include. The classical limit of nanoparticles is surprisingly small; Scholl et al. have shown that quantum effects do not become significant for nanoparticles until they are 2 nm or smaller [39]. Taking into account the quantum nature of very small nanoparticles would result in a substantial blue shift and minor broadening of the plasmon peak [39]. The nanoparticles used in this thesis are 10 nm or larger and so the quantum effects can safely be ignored. In the classical approach, light is treated as a wave, and the discrete nature of light can be ignored.

Lasers are often used to measure or excite nanostructures. They usually have a Gaussian beam profile with a maximum intensity at the center of the beam. Lasers used in the lab typically have spot sizes around 10-100 μm and a nanoscale object will only take up a small area in the beam waist at the focus. This area is small enough that the Gaussian profile of the beam can be ignored and to a good approximation, the nanostructure experiences an incident plane wave. The assumption of an incident plane wave source is ubiquitous in nanophotonics, the field of optics concerned with light-matter interactions at that nanoscale, and it greatly simplifies the theory

involved with the response of a nanostructure.

1.1.2 Achievements of Nanotechnology

Our understanding of light combined with our ability to structure matter on the nanoscale has given rise to some interesting and promising areas of research. Much of these areas are based around a phenomenon known as plasmons. Plasmons are conduction electron oscillations in matter, which form a negatively charged electron gas. Nanoplasmonics studies the generation of plasmons by light in nanostructures, often made of gold or silver. Plasmons lead to large electric field enhancements and localization of larger incident fields to small regions near the plasmons. They are an essential element in the research and experiments pertaining to this thesis and are described in detail in Chapter 3.

Metamaterials

Metamaterials is a field of research studying materials that have physical properties not seen in nature. These metamaterials exist over a wide range of sizes and in particular, there are nanoscale optical metamaterials. In many cases these unique physical properties emerge by making use of subwavelength features; the scale of the details in the structure of the metamaterial is smaller than the incident wavelength of light that it is intended to respond to. In this sense, the fields of nanoplasmonics and metamaterials have some overlap, since in many cases plasmonic structures are

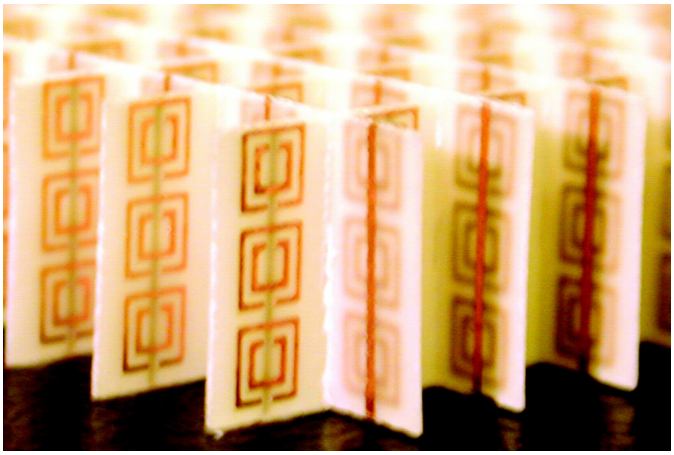

Figure 1.3: Microwave negative index metamaterial, made of split-ring resonators and silver wires [4].

much smaller than the incident light wavelength. Metamaterials often make use of a resonance dependent on the geometry and material properties used for the metamaterial and so there is a certain range of incident frequencies which the metamaterial operates successfully; off of the resonance the structure may behave like a normal material, but on the resonance it behaves like a metamaterial. Metamaterials are easily tuneable by changing properties such as particle/feature size, spacing, concentration, and shape. The first metamaterial operated in the microwave region of the electromagnetic spectrum. It was a negative index material made of a centimeter scaled lattice of unit cells consisting of gold split ring resonators and silver wires. In a negative index material, the path of the light wave and the energy carried by the light move in different directions. There is also research on cloaking devices which can make a small volume appear invisible, and superlenses which can theoretically focus light to a subwavelength spot.

Optical Sensors

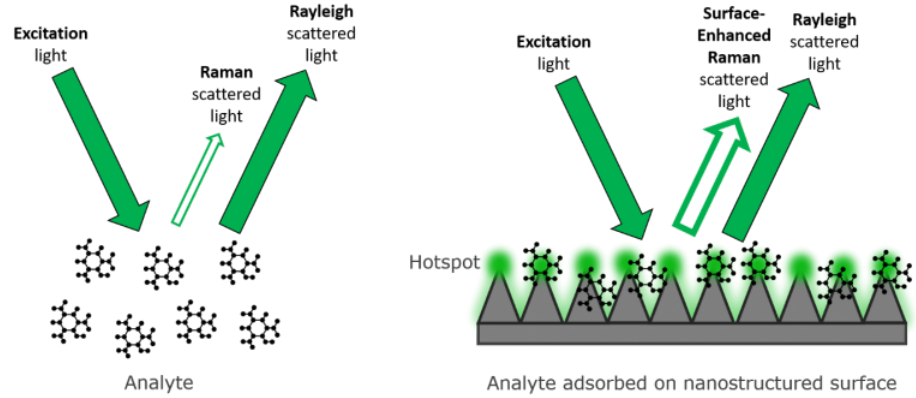

Figure 1.4: Schematic showing how SERS works [5].

Nanotechnology has been used to create highly sensitive optical sensors and spectrometers. Raman scattering is inelastic scattering of photons and electrons of target molecules. Every molecule has its own unique Raman spectrum, and so Raman can be used as a technique to identify material composition. However, the Raman process is very inefficient and occurs much less often than elastic Rayleigh scattering. Nanoplasmonic structures offer local field enhancements, which drastically increases the rate of Raman scattering. Typically a rough gold or silver surface or nanoparticle is added nearby the sample to be measured to increase the local field incident on the sample. This technique is known as surface enhanced Raman scattering (SERS). Raman enhancements of between 10^8 and 10^{10} are standard in SERS, allowing measurements of the Raman signal of single molecules! The enhancement is so large for the Raman process because it benefits from the local field enhancement two times. Both the rate of absorption of incident photons and the rate of emission of Raman scattered

photons are proportional to the intensity of the field at the absorption wavelength.

Optical Trapping

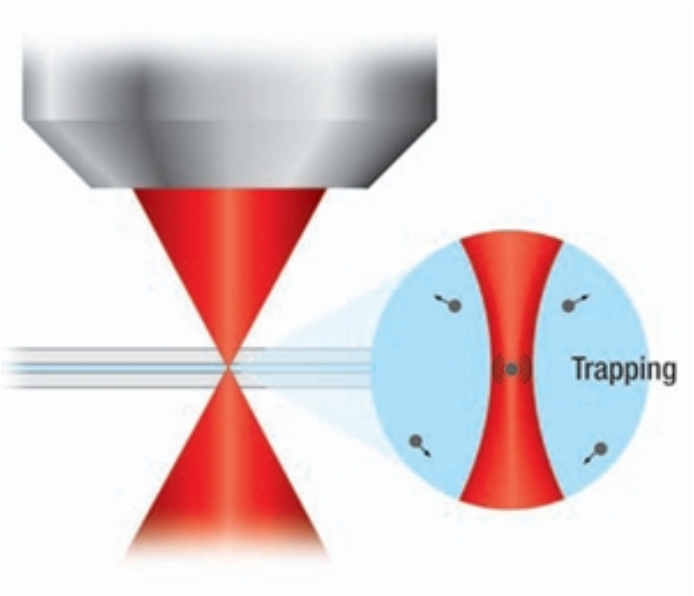

Figure 1.5: Molecules can be trapped by focusing a laser focused to a point, yielding a large intensity gradient [6].

Optical trapping is a relatively newly developed technique of trapping small particles with light. Optical trapping was first demonstrated by Arthur Ashkin in 1970 [40]. When illuminating small particles with a light beam it was found that they would move towards the center of the beam. This is due to an imbalance of radiation pressure experienced by the particle which is present when there is a significant gradient of the field over the volume of the particle. Naturally, a focused laser beam is a good illumination source for optical trapping due to the large field gradient it has. Plasmons exhibit strong fields in highly localized areas, and thus are effective in enhancing optical trapping. Double nanoholes have been used to trap single bovine

serum albumin proteins at the cusp, where the holes overlap and the field is strongly enhanced [23]. When a particle is trapped, some activity of the particle can be monitored by the change in the transmission signal over time. Optical trapping can then provide an in-depth view into the processes of individual proteins. For example, the unzipping of DNA has been measured by using optical trapping [41].

1.1.3 Plasmonic Solar Cells

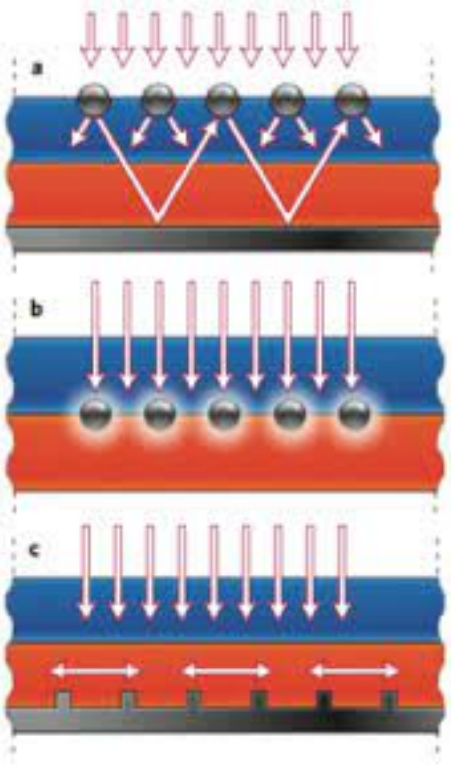

Figure 1.6: Particles or nanostructures can be added at any place in the cell, each increasing power conversion efficiency by a different method [7]. (a) Large particles at the top increase scattering in the cell. (b) Small particles inside the absorbing layer increase absorption. (c) nanostructuring of the bottom contact keeps light trapped in the absorbing layer.

Many studies have been focused on plasmonic enhancement of solar cells have been

performed by adding metal structures to the cells. Metal nanoparticles of various shapes and sizes have been added to the front, middle and rear of solar cells, to increase either scattered light into the cell, locally absorbed light, or the path length of light through the cell. Each of these methods add around a 1% power conversion efficiency to the cells. This may not seem like much, but over the lifetime of a standard silicon solar cell this would be a significant increase in the total energy absorbed by the cell. There is still plenty of research being done on the best size, shape and material to use, as well as the best place to put these particles in the cell, as these can change depending on the size, thickness and absorbing materials used to make the cell. Even with only a small increase in the efficiency, it may still be cost effective to add these nanoparticles to the cells.

Aside from inorganic solar cells, there are organic solar cells also known as organic photovoltaics (OPVs) which are made from organic semiconducting materials. These typically have much lower efficiency than inorganic cells, but are flexible and can be made simply and cheaply compared to inorganic cells. There has been extensive research on OPVs to make them more cost effective than silicon cells by increasing their durability, lifetime, and efficiency. P3HT (poly(3-hexylthiophene)) is a commonly used material in OPV research and has been studied for decades. P3HT is a conductive, highly absorbing polymer and has many interesting properties. P3HT is very strongly absorbing, degrades in oxygen atmosphere, and has a low charge carrier mobility, typical of most OPV materials. However, P3HT is also a conjugated

polymer and long chains of P3HT macromolecules can cause charge delocalization and greatly improved charge transport. It can form both a J-aggregate and an H-aggregate, depending on the conditions of its polymerization [42]. These aggregate structures have characteristically narrow linewidths, with the J-aggregate typically red-shifted in comparison to the H-aggregate peak. P3HT is used because it was one of the first successful OPVs and the scientific community has spent much time understanding and improving the efficiency of P3HT based OPVs. P3HT absorbs light so strongly that only a 100 nm layer thin cell is needed to absorb light efficiently as opposed to inorganic cells which can be hundreds of micrometers thick. Organic solar cells benefit even more from plasmonic enhancement than inorganic solar cells due to their stronger absorption.

1.2 Motivation

The initial goal of this work was to enhance the absorption in organic solar cells by adding gold nanoparticles. We were interested in how gold nanoparticles could increase absorption in P3HT. However, when we looked at the results, the absorption and scattering occurred over a surprisingly narrow region of the spectrum. This is not ideal for solar cells, as a large portion of the incident solar spectrum is then transmitted through the cell and not absorbed. However, the fact that the absorption and transmission were so narrow was strange and interesting. This is unexpected

because traditionally when there is a lot of "loss" (absorption) in a plasmonic system such as gold nanoparticles in P3HT, a broader optical interaction is expected. Upon further research it became apparent that there was no previous works done which showed a lossy medium yielding a narrow spectral response than a non-lossy medium. In the literature, the common theme was that more loss meant a broader response, but that is not what we saw in gold and P3HT. Upon this realization we developed theories, and performed simulations and experiments to determine why the spectral response was so narrow for gold in P3HT. Understanding how the linewidth narrows is important because we can use this information to make more effective plasmonic devices. Many plasmonic devices benefit from narrow linewidths and so loss is avoided in many systems, but if loss can provide even narrower linewidths than non-lossy materials, then there could be many materials that were initially ignored that could prove to be very effective in plasmonic devices. The material in this thesis is important in disproving the common assumption in the nanoplasmonics community that loss necessitates a broad linewidth.

1.3 Agenda

This thesis is broken down into an introduction and literature review, followed by a theory chapter, a chapter for simulations, a chapter for experimental results, and a conclusion chapter to summarize the major results and findings.

Chapter 1 Brief history of nanotechnology and light-matter interactions. Introduction of basic concepts pertaining to the work done in this thesis.

Chapter 2 In-depth review of nanoplasmonics with a focus on the history of linewidth reduction and Mie theory in lossy media.

Chapter 3 Detailed explanation of the theories which were used to find important and novel results for plasmonics in dispersive and lossy medium.

Chapter 4 The results of the simulations for each of the different projects are shown and reviewed.

Chapter 5 Experimental results are shown. This chapter contains descriptions of the experimental apparatus for each of the experiments performed, as well as an analysis of the results and comparison to those of theory and simulations.

Chapter 6 A summary of the results of the research and their implications for future work in the area of plasmonics in lossy and dispersive media.

Chapter 2

Literature Review

2.1 Nanoplasmonic linewidth

The basis of this thesis is understanding plasmonic resonances in lossy and dispersive media. The term lossy means that the medium absorbs light, while the term dispersive means there is a spectral dependence on the optical response of the medium (these features can be modelled mathematically by a permittivity ϵ with an imaginary component and allowing both the real and imaginary parts to be dependent on the frequency of incident light). There are very few works in the literature on this topic, despite it being the overlap of two large fields in the nanophotonics research community; plasmonics and Mie scattering theory. Mie scattering theory describes the more general case of how light is scattered from an arbitrarily sized particle from an incident light source. Even though it has been used for over a century, there are still new problems

to solve and advancements are consistently being made to the theory. Plasmonics is concerned with free electron waves generated by an incident light beam in conductors termed plasmons. These plasmons have characteristic plasmon resonance peaks which are quantitatively defined by their linewidths (full-width at half-max, FWHM) and the wavelength/frequency of the peak. There have been many advancements in understanding how plasmon peaks change for different metals and non-lossy media throughout the history of the literature. Plasmon resonances have been studied for over a century and have many applications including SERS (surface enhanced Raman scattering) [43, 24, 44, 45], optical tweezers [46, 47, 48], biosensing [49, 50, 51, 52, 53, 54, 55], subwavelength imaging [56, 57, 58], waveguiding and nanocircuits [59, 60, 61, 11, 62], enhancement of upconversion and downconversion [63, 64, 65, 66], harmonic generation [67, 68, 69, 70] and photovoltaics [71, 72, 73, 74]. A narrow linewidth is desirable for many of these applications [75, 76, 77]. In particular, the figure of merit (FOM) often used in optical sensing is:

$$\text{FOM} = \frac{S}{\text{FWHM}} \tag{2.1}$$

where $S = \frac{d\lambda_r}{dn}$ is the sensitivity of the sensor (how much the peak shifts due to a change in the local refractive index), and FWHM is the linewidth of the plasmonic sensor [78]. For optical sensors, a narrow linewidth results in a higher quality sensor. Of course, the figure of merit is only used to estimate the effectiveness of a device

and should not be taken too literally. These optical sensors detect a shift in the plasmon peak from a change in the index of refraction of the environment nearby the plasmon. Having a narrow peak ($FWHM$ is small) makes smaller shifts easier to detect. However, if the peak shift is very large (S is large) then it is less important to have a narrow peak. This idea is captured in the formula for the FOM.

The linewidth of the plasmon peak is assumed to be directly related to the total decay time from all of the various plasmon energy loss mechanisms [10]

$$\Gamma = \frac{2\hbar}{T_2}, \tag{2.2}$$

where Γ is the linewidth of the plasmon peak, and T_2 is the total decay time. Usually, the plasmon loss mechanisms are assumed to act independently from one another, and are simply added together.

$$\frac{\hbar}{T_2} = \gamma_1 + \gamma_2 + \gamma_3 + \ldots, \tag{2.3}$$

A variety of loss mechanisms can affect T_2 and Eq. (2.3) states that adding more loss mechanisms, or increasing the rate of existing ones, will decrease T_2 and thereby increase the linewidth. The effects of these loss mechanisms are encapsulated in the material permittivity function by adding additional terms to the bulk permittivity. The bulk permittivity inherently includes electron-electron, electron-phonon,

and electron-defect scattering terms, which are explained later in this chapter [79]. It is the permittivity that you would calculate from experimental measurements of the reflection and refraction of light by a large volume of the material (hence the terminology, "bulk"). The modified permittivity of both the metal and the surrounding medium is used in calculations of the linewidth. One of the first equations relating the plasmon linewidth to the permittivity functions was done for a small metal nanoparticle in a surrounding medium [80]:

$$\Gamma = \frac{2\epsilon_2}{\sqrt{(\frac{\partial\epsilon_1}{\partial\omega})^2 + (\frac{\partial\epsilon_2}{\partial\omega})^2}}, \tag{2.4}$$

where ϵ_1 and ϵ_2 are the real and imaginary parts of the metal permittivity. The derivation is shown in Appendix A.1. In this commonly used formula, the effect of the permittivity of the surrounding medium has been ignored. However, the medium permittivity can have a large impact on the plasmon peak, so this formula should be used with caution.

The plasmon decay time can be separated into an elastic and inelastic part [79, 10]

$$\frac{1}{T_2} = \frac{1}{2T_1} + \frac{1}{T_2^*}. \tag{2.5}$$

T_2^* is known as the pure dephasing time, and is the dephasing of the plasmon oscillations due to elastic self-interactions over time, ignoring all possible external interac-

tions. A plasmon consists of many electrons oscillating in phase, and these electrons can exchange energy with each other. These energy exchanges can then change the frequency of some of the electrons in the plasmon, and so results in a dephasing of the plasmon. This is an unavoidable dephasing time and is always present. Of course, the plasmon can exchange energy with its local environment a number of different ways, which will also cause dephasing, and this is accounted for by the population dephasing time, T_1. T_1 is due to inelastic scattering processes and is further separated into a radiative and non-radiative relaxation time $T_1 = T_r + T_{nr}$. The decay rates are usually given in units of meV, and are related to the relaxation times, in seconds, by $\gamma = \frac{\hbar}{T}$. The total dephasing time of a plasmon is very fast, typically on the order of a few femtoseconds (fs), and is difficult to measure precisely.

The non-radiative term T_{nr} contains the bulk damping term described above. To simplify the problem, it can often be assumed that the effect of electron-defect scattering is negligible. Then bulk damping is the plasmon decay only from electron-electron and electron-phonon scattering processes within the material. This is dependant on the material properties of the metal the plasmon is contained in. In many cases the medium embedding a metal nanoparticle is a dielectric, and the conducting electrons that make up the plasmon are constricted to moving back and forth within the metal. Then the electron-electron and electron-phonon interactions occur within the metal structure alone, not in the dielectric. With this assumption, the bulk damping decay

rate is

$$\gamma_b = \gamma_{e-e} + \gamma_{e-ph}, \tag{2.6}$$

where γ_{e-e} and γ_{e-ph} are the electron-electron and electron-phonon scattering rates within the metal.

Electron-electron damping is the damping from collisions of electrons in the plasma with other electrons. It is described by [81, 82]

$$\gamma_{e-e} = \frac{\pi^3 \Sigma \delta}{12 E_F}[(k_B T)^2 + (\frac{\hbar\omega}{2\pi})^2], \tag{2.7}$$

where E_F is the Fermi energy, Σ is the Fermi-surface average scattering probability, δ is fractional umklapp scattering, k_B is Boltzmann's constant, T is the temperature, and ω is the incident frequency. The electron-electron relaxation time ($\tau_{e-e} = \frac{\hbar}{\gamma_{e-e}}$) is very fast and has been measured for gold to be 19 fs at 850 nm [83].

Electron-phonon damping is the other portion of bulk damping, which arises from the energy exchange between electrons and the lattice of the metal containing the plasmon. It is described by [84, 85]

$$\gamma_{e-ph} = \gamma_0[\frac{2}{5} + 4(\frac{T}{\Theta})^5 \int_0^{\Theta/T} \frac{z^4}{e^z - 1} dz], \tag{2.8}$$

where γ_0 is a constant dependant on the metal, Θ is the Debye temperature. The derivation is shown in Appendix A.2. Equation (2.8) is derived under the assumptions

that the incident photon energy is much larger than the thermal energy, but much smaller than the Fermi energy, which is the case for gold and other noble metals in the optical spectrum.

Surface scattering is the collision of the electrons in the plasma with the surface of the nanoparticles and can damp the plasmon oscillations, reducing the linewidth. It is a non-radiative mechanism contributing to T_1. For smaller nanoparticles (below 20 nm) this becomes a significant form of linewidth reduction and dominates radiation damping [86]. The linewidths of smaller nanorods (8-14 nm diameter) and larger nanorods (30 nm rods) were measured in dark field scattering experiments. It was concluded that the smaller rods had broader linewidths from surface scattering while the larger rods had broader linewidths from radiation damping, and the narrowest linewidth was for 19 nm rods, where the surface scattering and radiation damping were more balanced [87]. The formula for the contribution of the surface scattering to the linewidth is:

$$\gamma_s = \frac{Av_f}{R}, \tag{2.9}$$

where v_f is the Fermi velocity of the electrons, R is the radius of the nanoparticle, and A is a phenomenological constant to fit to experimental data. The surface scattering term has an inverse relationship with the radius of the nanoparticle [88, 89]. In the literature, surface scattering values for A are inconsistent [39, 88, 90, 91]. There is also some uncertainty in the literature about the existence of surface scattering.

Single nanoparticle measurements have matched with theory without the need for a phenomenological surface scattering term [92]. More work is needed to understand this contribution to the linewidth.

As the electrons in a plasmon are oscillating, they are accelerating and so they are also spontaneously radiating. This mechanism is the radiative contribution, T_r to T_1. This effect is accounted for by the radiation damping term [93, 94]:

$$\gamma_r = 2\hbar\kappa V, \tag{2.10}$$

where κ is a phenomenological constant, and V is the volume of the nanoparticle. The radiation damping term scales with the volume of the nanoparticle and becomes the dominant source of linewidth broadening for larger particles. The radiative decay rate is related to the non-radiative decay rate by [95]:

$$\gamma_r = \frac{\sigma_{scat}}{\sigma_{abs}}\gamma_{nr}, \tag{2.11}$$

where σ_{scat} is the scattering cross section and σ_{abs} is the absorption cross section. Qualitatively, the scattering cross-section is related to the amount of light deflected by an object and absorption cross-section is related to the amount of light absorbed by an object. These concepts are explained in-depth in the next chapter.

Chemical interface damping is the transfer of energy through electron transfer

between the metal containing the plasmon and molecular adsorbates on the surface of the metal [91, 96, 97]. It is a non-radiative damping mechanism which contributes to T_1. This effect has been measured in experiments by adding adsorbates on the surface of metal nanoparticles and measuring the change in the linewidth [98, 97]. There is a linear dependence of the linewidth on the average distance of the electrons to the surface of the metal nanoparticle [97]. For very small particles, chemical interface damping can become the dominant plasmon damping mechanism.

Landau damping is a collisionless self-interaction of the electrons forming the plasmon and the field they produce [99]. It is a separate phenomena than electron-electron damping, which is the result of the effects of many individual collisions between two electrons [100, 101]. Assume there is some range of oscillation frequency with which we accept that free electrons oscillating at this frequency are part of the plasmon. Then the electrons in the plasmon will have a velocity distribution and if there are more electrons with a velocity below the phase velocity of the plasmon wave (the average electron velocity), energy from the plasmon field is taken to speed up these slow electrons, and the plasmon is damped. If the median electron velocity is above the plasmon phase velocity, then energy is taken from the fast electrons and stored in the plasmon field, causing anti-damping. Landau damping has been observed in experiments with effectively collisionless plasmas [102].

It is known that plasmon resonance linewidths are broadened by electromagnetic absorption in the metal containing the plasmons. Metals like gold and silver have

interband transitions which can be excited by the oscillating plasmon, resulting in an energy exchange between the plasmon and the metal and ultimately leading to damping. The increase in linewidth has been monitored over time upon exciting an interband transition in gold, showing that as the interband transition is excited, the linewidth broadened [103]. There are some advantages of loss in thermally driven applications like thermophoresis for information storage [104] and reducing spontaneous emission noise in amplifiers [105]. Overall, optical losses in metal are generally undesirable in plasmonic applications, even without considering linewidth broadening [106, 107, 108]. Large losses can result in inefficient devices, since a large portion of the incident optical energy is lost to absorption in the metal. Unfortunately, metals like gold and silver which are commonly used in plasmonic devices, have interband transitions in the ultraviolet and visible parts of the electromagnetic spectrum, and so are very lossy at these wavelengths. However, their optical properties make them well-suited for plasmon generation so most research in plasmonics is done with gold and silver nanoparticles.

All of the above damping mechanisms can be used to define the homogeneous linewidth, which is the linewidth expected for an individual metal nanoparticle. In experimental measurements, it is often the case that the signal from the plasmon resonance of many particles at once are collected in a single measurement. Since each nanoparticle is not exactly identical and experiences different environmental factors, each will have a slightly different linewidth. Then in these experiments, the

measured linewidth is broadened, and the measured linewidth is the inhomogeneous linewidth, not the homogeneous linewidth. Dark field measurements are capable of measuring single isolated nanoparticles, which makes them an excellent method for directly measuring the homogeneous linewidth [109, 92].

2.2 Reducing Linewidths

There are many different damping mechanisms, and most of these can be altered in some way, which means there are a large number of possible ways to reduce linewidths. As an example, even radiation damping can be reduced, despite it being an unavoidable form of damping (it will never be exactly zero). One way to reduce radiation damping is to use a smaller metal nanoparticle. The radiation damping term is dependent on the volume of the particle as can be seen from Eq. (2.10). Another way to reduce radiation damping is by exciting higher order multipolar modes. Usually plasmons are generated through exciting a dipolar mode in a metal nanoparticle, as these couple most easily to radiation, however, higher order modes can also sustain plasmons. Since these modes do not couple as easily to incident light as plasmons in the dipolar mode, the higher order multipolar modes are called dark modes. It was found for silver nanorods, the quadrupolar and octupolar modes have about half and one third the linewidth of the dipolar mode, respectively [110]. In nanoplasmonics, Fano resonances and multipolar modes are closely related. A Fano resonance is an

often narrow, asymmetric linewidth due to the interference of a discrete scattering process and a continuous background scattering process [111]. Fano resonances were first seen in the helium atom, where the excitation of the $2s2p$ discrete state and the ejection of a single electron into the continuum overlap in the energy spectrum and their interference produces a narrow asymmetric linewidth. Fano resonances can achieve high quality factor resonance peaks, but at the cost of signal transmission strength [112]. Fano resonances in asymmetric nanoplasmonic devices can be created by exciting dark plasmonic modes. Since these modes do not couple as well to radiation, the device overall will have much less transmission at the wavelength of the dark mode. On the other hand, the reduced coupling to radiation also lowers radiative loss as explained above, which is commonly the largest form of loss so the linewidth is expected to be reduced greatly. Fano resonances from a periodic lattice of nanostructures were found to cause narrow linewidths due to diffraction effects which partially mitigated the losses in metal nanoparticles [113].

Diffraction coupling of localized surface plasmon resonances into a periodic lattice of metal nanostructures can produce extremely narrow linewidths on the order of a few nanometers [114, 115, 116, 113]. Plasmons are very sensitive to their dielectric environment and both the peak position and linewidth can change by changing the dielectric constant of the local environment. Periodic metal structures have been shown to make sensors, highly sensitive to changes in the local refractive index, which is desirable for biosensing [117]. In a lattice of closely spaced nanoparticles the plas-

mons can transfer electromagnetic energy between nearby nanoparticles, rather than radiating the energy into the far-field, and so the radiation damping is greatly reduced. One possible drawback to this technique is that these diffraction arrays can take up large areas, and may require expensive nanofabrication methods and special equipment to produce.

Gold bypyramidal nanoparticles had their linewidths reduced by about 30% when cooled from room temperature to 77K [95]. This was due to a significant reduction in electron-phonon scattering process. However, they found cooling below 50K did not further reduce the linewidth; at this temperature the electron-phonon interaction had been effectively negated entirely. Then adjusting the temperature of a plasmonic device can reduce the linewidth depending on how large of a role the electron-phonon damping term plays in linewidth broadening. Considering only material dependant damping mechanisms (no geometry dependence like radiation and surface scattering), and setting electron-phonon scattering to its minimum theoretical value, a minimum possible linewidth of 43 meV for gold and 26 meV for silver were predicted [95]. These values for the minimal possible linewidth apply to any geometry of gold and silver devices, and are not restricted only to bypyramidal shapes. The reason silver is not used as much as gold in nanoplasmonics although it has a potential for a narrower linewidth and is cheaper is because silver oxidizes, and so is not stable like gold is. Once silver has an oxidized layer, its linewidth broadens becoming much larger than that of gold.

As mentioned above, plasmons are very sensitive to changes in the local environment. A halving of the plasmon linewidth has been observed for aluminum nanoparticles placed on aluminum films [118]. By adding a metal film under the nanoparticle, symmetry is broken and incident plane wave light can excite the quadrupolar (and higher order) mode of the nanoparticle. Both the quadrupole and dipole modes then can couple electromagnetic energy back to the film rather than radiating, and so the radiative decay rate is decreased by the presence of the metal film, thereby also reducing the linewidth. Aluminum experiences such a significant reduction in linewidth because it has a large radiative decay factor compared to gold and silver. This linewidth narrowing was also seen in gold dimers on a gold film, where the linewidth was narrowed from 209 nm on just a silica substrate to 45 nm [119] when a thin gold layer was added underneath the dimers. Gold films have also been used to further reduce the linewidth of narrow Fano resonances. A very narrow linewidth of 9 nm has been achieved for asymmetric gold disk-ring systems on a gold film [120].

2.3 Loss in Plasmonics

As losses in metal have been shown to broaden linewidths, there has been research on adding optical gain materials ($\mathrm{Im}(\epsilon_2) < 0$) nearby plasmons to offset the losses from absorption of energy by the metal. Adding materials with gain, such as organic dyes, around noble metal nanoparticles can result in narrower and larger plasmon

peaks [121, 122, 123]. With a large enough gain from the surrounding medium, a spaser can result (surface plasmon amplification by stimulated emission of radiation) [12, 124]. Spasers have extremely narrow linewidths on the order of 1 nm [125, 126].

When surrounding a metal nanoparticle with an absorbing material, the opposite of a gain material, one would expect that the linewidth should be broadened and the plasmon peak reduced. In the literature, it is common to see gold nanoparticles added to the active layer of a solar cell (the layer which absorbs the light) to broaden the absorption spectrum and increase the device efficiency [127, 128, 129]. While the general consensus is that all forms of loss increase the linewidth of plasmonic resonances, there has been no direct proof that embedding a nanoparticle in a lossy medium will broaden the linewidth.

2.4 Mie Theory in Lossy Media

Mie theory is the theory which describes the scattering and absorption of light by an object embedded in an infinite and homogeneous surrounding medium [130, 131]. Mundy et al. were the first to consider Mie scattering in a lossy medium [132]. They adapted the standard Mie formulas for the scattering and absorption cross sections for a lossy embedding medium considering only the far-field approximation. Bohren and Gilra later calculated the extinction cross section, rather than the absorption

and scattering cross sections of a nanoparticle in an absorbing medium [133]. For a non-lossy medium, the extinction cross section is simply the sum of the absorption and scattering cross sections, as the extinction is the result of only these two separate processes. However, they noted in a lossy medium, using the standard absorption and scattering cross sections is undesirable, as they are intrinsically tied together in a non-trivial way. The spectrum of the scattered light changes as it propagates through the lossy medium and is absorbed. The absorption of light by the lossy medium over the optical path to the particle changes the incident spectra which then changes the resulting scattering spectrum. The result is that the scattering and absorption cross sections both depend on the radius of the conceptual integrating sphere (the distance from the particle) and thus are not parameters at all, but are variables. Bohren and Gilra found that by looking at the extinction cross section, rather than the individual scattering and absorption cross sections, this problem could be avoided [133]. Using the far-field approximation, they derived an extinction cross section which depended only on the size and optical properties of the spherical nanoparticle and medium. They also expressed that there can be very large differences in the amount of extinction and the location of the extinction peak when not considering losses from the medium.

In scattering and extinction measurements, the surrounding medium is not infinite, as was the case for Bohren and Gilra's extinction cross section [133]. Lebedev et al. looked at finding the scattering and absorption cross sections by many

isolated nanoparticles in a thin film lossy medium [134]. The particles are assumed to be far enough away that any electromagnetic interactions between them can be ignored. Bohren and Gilra had defined the extinction cross section as the energy deficit of the incident plane wave at a detector far from the nanoparticle due to the presence of the particle [133]. Lebedev et al. had a two step process to finding the extinction of a nanoparticle in a thin lossy film [134]. First, they found the difference in local extinction by the presence of a single particle instead of a medium. This was done by integrating the Poynting vector over the surface of the particle and subtracting the extinction of just the medium in this same volume. This quantity gives the change in extinction from the existence of the particle, not the actual extinction of light, and it can be negative if the particle has less extinction than the medium in the same volume. Then they integrated over infinitesimal layers with an adjusted extinction coefficient dependent on their calculated extinction value for a single particle, the number of particles in the layer, the medium absorption coefficient, and the thickness of the full layer. This definition of extinction gets rid of the dependence of extinction on the total path length of the light in place of well-defined parameters such as the finite thickness of the layer, and so it is also a well-defined property of the nanoparticle and medium system in question. The theory matched well with the quasistatic model when used to predict the extinction of light from 2 nm iron nanospheres with a 5% concentration uniformly spread in a matrix of fullerite (C_{60}). However, there was a reasonably large difference between their calculations and the measured spec-

tra of iron clusters embedded in a fullerite matrix. There was a slight difference in the absorption coefficient of fullerite used between theory and experiment that can explain part of this difference. Lebedev et al. succeeded in finding a formula that works for describing the extinction of thin lossy films, with a reasonable agreement with experimental results [134]. With this method, the fields on the surface of the particle, and not far from the particle like Bohren and Gilra's method, are needed, so this way of calculating the extinction was called the near-field approach.

Sudiarta and Chylek showed that the extinction coefficient in the limit of a large spherical nanoparticle approached different values for non-absorbing and absorbing media [135]. They used a near-field approach similar to Lebedev et al.'s, where the calculation of the scattered and absorbed power is performed over the surface of the nanoparticle. One distinction between Sudiarta and Chylek's and Lebedev et al.'s results is that Sudiarta and Chylek accounted for the difference in intensity of incident light across a spherical nanoparticle by averaging the intensity over the circular cross-section of the nanoparticle. Thus, the reduced extinction coefficient for large spheres in an absorbing medium they attributed to the lack of extinction by diffraction from the sphere, as much of the incident light gets absorbed by the medium before it can be diffracted by the edge of the sphere for larger spheres. Another major difference is that Sudiarta and Chylek did not include the extinction by absorption in the surrounding medium in their work [135]. They only factored the medium extinction once it was incident on the particle, but the absorption of light approaching or leaving

the vicinity of the particle by the medium was ignored. In scattering measurements, this extinction is unavoidable and can be significant with very lossy materials or thick layers and so Sudiarta and Chylek's technique should not be used in these cases.

There were two different approaches developed for dealing with Mie theory in lossy media; the near-field approach and the far-field approach. The near-field approach cast away any dependence on the conceptual integration spheres, but made it more difficult to incorporate the extinction by the medium absorption. On the other hand, the far-field approach inherently incorporated the medium absorption, but made it difficult to avoid the dependence on the arbitrary radius of the conceptual sphere of integration. The far-field approach also assumed an isotropic and infinite medium, so was less useful for comparison to experimental results which involve finite thickness films. Fu and Sun used the near-field approach to calculate the absorption cross section using internal fields rather than external fields as Lebedev et al. did [136]. The benefit of this was to provide a formula for absorption within a particle without the need to define absorption as the difference between the extinction and scattering cross sections, and so the absorption of a particle in a lossy medium could be well-defined in this way. Fu and Sun also showed that for a large sphere in a lossy medium, the extinction cross section tends to 1, agreeing with Sudiarta and Chylek [136]. They concluded that the absorption of the medium has little effect on the overall absorption efficiency, though they only used relatively small values for the absorption of the medium. Also, these formulas they derived do not apply for strongly lossy

media because similarly to Sudiarta and Chylek, the extinction from absorption by the medium was ignored in Fu and Sun's work. Yang et al. were first to point out the discrepancy between extinction cross sections calculated using Lebedev et al.'s near-field approach and the actual extinction from the particle and medium system. They calculated the "inherent" and "apparent" optical properties of a sphere and shell nanoparticle in absorbing medium [137]. Inherent extinction is the extinction of a particle within the medium and in a medium with low loss is a close approximation to the apparent extinction. The apparent extinction included extinction of the inherent signal by the surrounding medium, and is what would be measured in an experiment. Yang et al. showed that the inherent and apparent extinction can give drastically different results when the medium has significant absorption.

Videen and Sun managed to use a far-field approach which avoided the issue of dependence on the radius of the conceptual sphere of integration [138]. They considered the case where there was no nanoparticle, and only absorption from the medium occurred. Then they considered the case where there was a nanoparticle, and found that this extinction had the same dependence on the path length through the absorbing medium as did the case without the nanoparticle. By subtracting these two cases, the extinction of the nanoparticle alone was obtained. Also, the incident intensity on the particle in the medium and the total extinction had the same exponential dependence on the distance travelled, and so the extinction cross section, which is the ratio of the two, was independent of this distance. The result

was a formula for the extinction cross section which did not depend on optical path length in a complicated way and agreed with the previously calculated extinction formula of Bohren and Gilra [133].

Yin and Pilon compared the near-field and far-field methods to find which was most suitable for the radiative transfer equations to find the apparent extinction for light passing through an absorbing medium with an ensemble of scattering particles. Mischencko solved the more general problem of a particle of arbitrary shape and orientation in a lossy medium using the far-field approach [139]. He concluded that the absorbing host affects the extinction by absorbing the incident and scattered light, as well as by changing the phase and scattering matrix elements. He stated that appreciable differences should be expected between extinction in lossy and non-lossy media.

2.5 Dispersion in Nanoplasmonics

Even with the luxury of having a variety of models to choose from to describe scattering of a particle in a lossy medium, it had not been shown that using a lossy medium necessitates a linewidth broadening. This is however, what would be expected, as it has been shown that adding losses to the metal broadens plasmon peaks [103, 106]. Metals have very large loss from interband transitions below the plasmon frequency, and metal nanoparticles are usually measured on glass or silica substrates in air, which

are non-lossy materials, so in most cases it is safe to ignore the loss in the surrounding medium. However, there are times where the absorption can be significant and can differ greatly from the scattering spectra of a non-lossy material [133, 135, 134], especially for strongly absorbing materials. For strongly absorbing materials, it is important to also consider the effects of dispersion. Absorption is the process of exchanging energy from an incident photon to excite the electron states of the absorbing matter. There are usually many discrete, separated energy levels to excite to so the absorption spectra will have many peaks and will be dispersive.

Resonances and damping effects are ubiquitous in physics. The Kramers-Krönig relations [140, 141] (see section A.8 for information on the Kramers-krönig relations) show that there will always be some damping in a physical system [142]. Plasmonic systems can be accurately represented by a familiar damped harmonic oscillator; the inductor-capacitor-resistor (LCR) electrical circuit [142]. It has been shown that plasmonic systems are nanoscale versions of these circuits [62]. It is understood that the linewidth of the resonance in an LCR circuit increases with the damping [142], and so the same behaviour is expected for plasmonic systems.

A deeper understanding of plasmonic systems, and damped harmonic oscillators in general, arises from analyzing the effects of dispersion on the plasmon peak due to a strongly absorbing and dispersive medium. Plasmon resonances are complex, and there are a variety of factors that can affect the peak shape, apart from material losses. Past works have studied the influence of nanoparticle geometry [87], back-

ground permittivity [143], and nanoparticle size [90] on the plasmon linewidth. For strongly absorbing media the Kramers-krönig relations necessitate dispersion. As real materials are dispersive and lossy it is important to understand how dispersive lossy materials play a role in changing the linewidth of plasmons in metal nanoparticles.

The effects of dispersion in the medium on the plasmonic response are not well-known. Most works in plasmonics ignore dispersion in the surrounding medium, or use non-dispersive media such as water air and glass. One work has recently engineered the dispersion of an optical system to increase its sensing capabilities (FOM) as a LSPR biosensor [144]. They found that by using higher concentrations of titanium in a titanium silver alloy, they could drastically reduce the dispersion of the nanoparticle, which would have two effects: the resonance peak broadened and the sensitivity to changes in the local refractive index greatly increased. For a good optical sensor, a high sensitivity and a narrow linewidth is desirable, so there will be some optimal dispersion to achieve the best FOM for sensing applications. The commonly referenced equation, Eq. (2.2) states that adding a loss mechanism (such as absorption in the surrounding medium) will necessarily reduce the plasmon decay time and broaden the linewidth. However, Eq. (2.2) is derived assuming there is no dispersion and may no longer hold when dispersive media are involved. The following chapters in this thesis go into more detail about the research and experiments performed with metal nanoparticles in dispersive lossy media.

Chapter 3

Theory

3.1 Drude-Lorentz Model

The Lorentz model attempts to explain how a material responds to an incident electromagnetic field. Once the response to the incident field is known, the total electromagnetic field in the presence of the material can be calculated. All materials are made of nuclei and electrons and the response of the material is the sum of the responses of these individual components. The Lorentz model is a classical model and treats the nuclei and electrons as points in space. The positively charged nuclei in the material are assumed to be stationary, while the less massive electrons are in motion near the nuclei. As is the case with many phenomena in physics, it is assumed that the equilibrium of the electron and the atom is stable, and so the electron will simply oscillate about the equilibrium position. This behaviour of bound electrons is

expressed by a spring force between the electrons and the nuclei of the material. The forces acting on an electron in the Lorentz model satisfy the following equation:

$$F = F_{\omega_0} + F_d + F_\omega. \tag{3.1}$$

F_{ω_0} is the spring force binding an atomic nucleus and an electron, F_d is the drag force from electron collisions, and F_ω is the driving force from an incident monochromatic (single-frequency) field. Rearranging these forces and removing the common harmonic time dependence of each force gives the amplitude of oscillations of the electrons:

$$x = \frac{q}{m}\frac{E_0}{\omega^2 - \omega_0^2 + i\gamma\omega}, \tag{3.2}$$

where q is the electron charge, m is the effective electron mass in the material, E_0 is the incident field amplitude, ω is the incident field frequency, ω_0 is the resonant frequency of the spring, and γ is the damping constant where $F_d = -m\gamma\dot{x}$. The above equation can be used to derive the relative permittivity,

$$\epsilon = 1 + \frac{\omega_p^2}{\omega_0^2 - \omega^2 - i\gamma\omega}, \tag{3.3}$$

where $\omega_p = \sqrt{\frac{Nq^2}{m\epsilon_0}}$ is the plasma frequency, N is the density of electrons, and ϵ_0 is the permittivity of free space. This is the central result of the Lorentz model, as the permittivity provides all the information about how electromagnetic fields interact

with the material.

When the electrons in a material are weakly bound, such as the free electrons in conductors, the spring force holding the electrons and nuclei together can be ignored. This leads to the Drude model [145], where the permittivity is described by Eq. (3.3) with $\omega_0 \to 0$:

$$\epsilon = 1 - \frac{\omega_p^2}{\omega^2 + i\gamma\omega}. \tag{3.4}$$

Typically, metals have a large density of free electrons, and so obtain a large plasma frequency ω_p. This gives them a characteristically large negative permittivity for longer wavelengths as can be seen by Eq. (3.4). It is common in both the Drude and Lorentz models to account for all other polarization effects apart from electron oscillations due to the incident electromagnetic field with a single phenomenological constant, ϵ_∞, such that at large frequencies, $\epsilon = \epsilon_\infty$. The adjusted permittivity for the Drude model is then

$$\epsilon = \epsilon_\infty - \frac{\omega_p^2}{\omega^2 + i\gamma\omega}, \tag{3.5}$$

and similarly the adjusted permittivity for the Lorentz model is

$$\epsilon = \epsilon_\infty + \frac{\omega_p^2}{\omega_0^2 - \omega^2 - i\gamma\omega}. \tag{3.6}$$

By measuring the reflected and transmitted light from thin metal films, Johnson and Christy were able to accurately determine the permittivities of gold and silver [146].

In gold, the Drude model matches the experimental data well for wavelengths above 500 nm, but below that there are some significant deviations. These deviations are caused by a failure of the Drude model to describe interband transitions. The Lorentz model can describe interband transitions by treating them as a spring force between an electron and an atom with resonance frequency ω_0 at the frequency of the transition, and so where interband transitions are present, the Lorentz model should be used. An interband transition will have a characteristic peak in the imaginary permittivity at the frequency corresponding to the energy of the transition, and so it is easy to see from the permittivity data which model to use to describe a material. The Drude and Lorentz models are often used in conjunction when describing more complicated materials such as semiconductors. For a semiconductor there are both conduction electrons, and bound electrons with interband transitions to consider. The Drude model describes the conduction electron portion of the material response, while the Lorentz model describes the material response for the bound electrons. Then a general material can be described by:

$$\epsilon = \epsilon_\infty - \frac{\omega_p^2}{\omega^2 + i\gamma\omega} + \Sigma_{k=1}^{N} \frac{f_k \omega_p^2}{\omega_0^2 - \omega_k^2 - i\gamma\omega}. \tag{3.7}$$

N gives the total number of interband transitions, and so for each interband transition, there is a separate Drude-Lorentz term with resonance at the interband frequency w_k with an oscillator strength f_k weighting the effect of the transition on the permittivity.

The Drude-Lorentz model is still used frequently and maintains good agreement with experimental measurements [147, 148, 149]. Many modern models are simply extensions of the Drude-Lorentz model [150, 151]. The Drude-Lorentz model is still used frequently instead of newer, more advanced models because it is simple to interpret and is accurate enough for most applications.

3.1.1 Plasmons

Plasmons form the basis of the processes and systems studied in this thesis, and so it is important to understand what a plasmon is. A plasmon is usually described in the literature as a collective electron oscillation at the interface formed between a dielectric and a metal. While this definition is true, it leaves out an important detail about plasmons; the oscillating charges are part of a longitudinal wave. A more precise definition for a plasmon is: a longitudinal charge density oscillation coupled to electromagnetic radiation. With this definition it is clear why not all electron oscillations can be considered plasmons and why a metal-dielectric interface is needed to form a plasmon. To demonstrate this point, imagine a TEM (transverse electric and magnetic) field propagating through a homogeneous material. Within the planes of constant phase, the electrons of the material will move transverse to the propagation direction due to the transverse electric field component, and the distance between the electrons remains constant. Therefore there is no longitudinal charge density wave formed although charge is oscillating, and so there is no plasmon.

Plasmons can be generated with light at the interface between a dielectric and a metal, which is why the first definition of a plasmon is so common in the literature. This is done by shining TM (transverse magnetic) light at an angle so that there is a longitudinal component to the electric field with respect to the metal-dielectric interface. The importance of the metal-dielectric interface is that there is a bound surface charge present which will form a plasmon along the interface due to the longitudinal electric field. These plasmons, known as surface plasmon polaritons (SPPs) can propagate relatively large distances of hundreds to thousands of micrometers from where they were initially excited [10].

There are three categories of plasmons: bulk plasmons, surface plasmon polaritons (SPP) and localized surface plasmons (LSP). Plasmons are a classical phenomenon that are derived directly from Maxwell's equations [10]. Bulk plasmons result from longitudinal electron oscillations within the volume of a material. These are described by the Drude-Lorentz model, where the plasma frequency, ω_p, is the natural frequency of the electrons in the material. The plasmon resonance frequency of these bulk plasmons is $\omega_p/\sqrt{(3)}$. Within the bulk, there is no interface where charge is bound, since the material is assumed to be homogeneous, and a TEM wave propagating through a bulk material will always have a transverse response. Therefore, TEM light cannot excite bulk plasmons. However, bulk plasmons can be excited using other techniques. As an example, an electron beam shot through a material will excite plasmons. The collisions between the electrons in the beam and the material

causes longitudinal motion of electrons in the material, and the energy lost by the electrons in the beam can be used to find the plasmon resonance. This technique is known as electron energy loss spectroscopy (EELS).

As described earlier, SPPs occur at a planar interface between a metal and a dielectric. These electromagnetic waves can propagate along the interface, but are bound at the surface, and thus evanescent in both the metal and dielectric layers in the direction normal to the interface. SPPs can only be excited by incident TM light. The resonance frequency for an SPP occurs when:

$$\epsilon_1 = -\epsilon_2. \tag{3.8}$$

This condition is typically met at some point in the electromagnetic spectrum for any general metal and dielectric pair as metals exhibit a wide range of values ϵ_1.

Finally, there are LSPs, which do not propagate and are evanescent in all directions. These come about from small subwavelength features in nanostructures. For instance, a metal nanosphere in an embedding medium generates a LSP on the surface of the metal. A double nanohole generates a LSP, with the strongest electromagnetic response at the cusp of the nanohole. For a metal sphere surrounded by a dielectric, the LSP resonance (LSPR) occurs when

$$\mathrm{Re}\{\epsilon_1\} = -2\mathrm{Re}\{\epsilon_2\}. \tag{3.9}$$

The nanocircuit model, developed in 2005, offers a more intuitive way to understand surface plasmons. The nanocircuit model applies the lumped element method of evaluating electrical circuits to optical devices at the nanoscale [62]. In this model, a dielectric with a positive permittivity acts as a capacitor, while a negative permittivity material, such as a metal, acts as an inductor. The imaginary parts of the permittivities represent absorption of light by the materials, and act as resistors in the circuit, where power in the electromagnetic field is dissipated. The accuracy of the nanocircuit model was verified in experiments where the transmission of a periodic layer of Si_3N_4 and air gaps was determined by a nanocapitor-nanoinductor circuit model [152].

The categorization of nanoparticles into nanocapacitors and nanoinductors in response to an external field can be understood by considering the similarities between the current and voltage across capacitors and inductors in AC circuits. In a LC circuit, the current through a capacitor leads the voltage (the current is 90 degrees ahead in phase) across the capacitor, while across the inductor, the voltage leads the current. Then the voltages across the capacitor and the voltage across the inductor are out of phase. When a monochromatic electromagnetic wave interacts with a material with positive permittivity, the positive nuclei and negative electrons in the material separate in a way that reduces the internal field. The charge distribution and the field oscillate with the same frequency, and at any point in time the charges are always distributed so that the field they generate opposes the incident field within

the material. For a negative permittivity the charges arrange themselves opposite to a positive permittivity material, the internal field is enhanced, and the charge oscillations of a negative permittivity material is out of phase with those of a positive permittivity material.

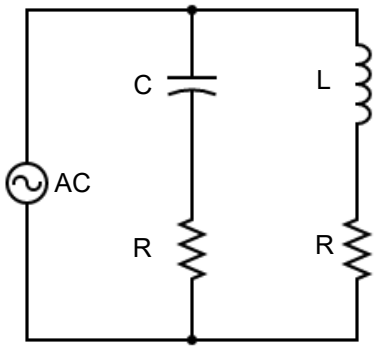

Figure 3.1: Equivalent circuit for a metal nanosphere in an infinite homogeneous medium. The role of the AC current source is adopted by the displacement current resulting from the oscillating incident light.

For a small metal sphere surrounded by a dielectric, the equivalent circuit is an inductor and capacitor in parallel, each with a series resistance as is shown in Fig. 3.1. This gives rise to an LC resonance, which is the plasma resonance. Thus the circuit model can be used to calculated the plasmon resonance frequency

$$\frac{1}{LC} = \omega_0^2 \tag{3.10}$$

where L, the inductance, and C, the capacitance, can be derived from Maxwell's

equations and appropriate boundary conditions for the dielectric displacement D [62]:

$$L = [-\omega^2 \pi a \mathrm{Re}\{\epsilon_1\}]^{-1}, \tag{3.11}$$

$$C = [2\pi\omega a \mathrm{Re}\{\epsilon_2\}] \tag{3.12}$$

where a is the radius of the sphere, ϵ_1 is the permittivity of the sphere, and ϵ_2 is the permittivity of the surrounding medium. The condition for LC resonance is satisfied when

$$\mathrm{Re}\{\epsilon_1\} = -2\mathrm{Re}\{\epsilon_2\}, \tag{3.13}$$

which matches the LSP resonance condition from the conventional definition of an LSP (3.9).

Plasmons have a wide range of practical applications. They can be used in Raman spectroscopy to greatly increase the magnitude of the Raman signal [153]. Raman scattering benefits from a fourth power scaling with the local electric field amplitude [154]. The Raman process is very infrequent, but using the local field enhancement from a metal nanostructure, the Raman signal from single molecules have been observed [24]. Plasmons are used in biosensors to measure reaction rates. Plasmonic sensors are incredibly sensitive to changes in the permittivity of the local environment, and when a binding reaction occurs, for example, between an antibody and an antigen, the change in the permittivity produces a measurable change in the plas-

mon resonance [49, 155, 54]. One advantage to using plasmons as biosensors is that they are "label free", meaning that there is no need to include fluorescent molecules to monitor the reaction rate, which can sometimes significantly alter the reaction rate. Both LSPs and SPPs are used in solar cells by addition of metal nanoparticles, nanostructures, or metal films which enhance the fields, or the path length of light within the solar cell, and thus the absorption and efficiency of the cell [156]. The Gaussian field of a laser tends to localize small particles to the center of the beam, which is known as optical trapping [157]. Including nanostructures can enhance the trapping ability of a laser. The field enhancement from plasmons in the cusp of double nanoholes allows for a strong local field and efficient optical trapping of individual proteins. The trapped transmission signal can show discrete steps which give valuable information about protein folding processes, such as the zipping and unzipping of DNA by P53 [41].

3.1.2 Dispersion and Loss

Dispersion is the dependence of an object on the wavelength of light that is incident on the system. Dispersion is a common phenomenon seen in every-day life. The refraction of light in water droplets, or by a prism to produce the colours of the rainbow are examples of dispersion. The cause of dispersion is explained at the atomic scale. Light is absorbed by an atom in a material, then an electron becomes excited and re-emits the absorbed energy in the form of a photon. The energy of

the emitted photon is related to the available electron states of the atom. Since different colours of light have different energies, then the light-matter interaction between the different colours occur at different rates. With higher collision rates, the light is slowed more due to being stored as absorbed potential energy in an atomic electron transition before being re-emitted. Also, when there are more collisions, there is more scattering of photons between atoms in the material, increasing the path length of light and further decreasing the effective speed of light. So light at different frequencies experience different collision rates with the atoms of a material which adjusts the speed of light in that materials and so each frequency of light travels at a different speed.

Dispersion is a general wave phenomenon exhibited by any physical system described by the wave equation

$$\nabla^2 f - 1/v(\omega)^2 \frac{\partial^2}{\partial t^2} f = 0, \tag{3.14}$$

with v being the velocity of the wave in the medium, which depends on the frequency of the wave. The general solution to this equation is $f = Ae^{i(\mathbf{k}\cdot\mathbf{r}-\omega t)} + Be^{i(\mathbf{k}\cdot\mathbf{r}+\omega t)}$, where k is the wavevector and r is the position vector. With the form of the solution known, the operators in the wave equation can be applied to the general solution and

this gives the dispersion relation:

$$k^2 = \omega^2/v(\omega)^2. \tag{3.15}$$

The dispersion relation must always hold true for electromagnetic waves travelling through any medium. In many media, the velocity of the waves do not have a significant dependence on ω, such as in glass or air, and so there is a simple linear dependence between the wavevector and the frequency. Materials with this behaviour are deemed "non-dispersive". The velocity of an electromagnetic wave in a medium with index of refraction n is given by

$$v^2 = c^2/n^2 \tag{3.16}$$

where c is the speed of light in vacuum. In general, the index of refraction of a medium is

$$n = \sqrt{\epsilon\mu}. \tag{3.17}$$

Most materials are non-magnetic and so $\mu \approx 1$, then the index of refraction simplifies to

$$n = \sqrt{\epsilon}, \tag{3.18}$$

and any interesting dispersion information of the dispersion relation is now stored in ϵ

$$c^2k^2 = \epsilon(\omega)\omega^2. \tag{3.19}$$

There are two types of dispersion, which stem from the Drude-Lorentz model; these are normal and anomalous dispersion. In most materials, the permittivity will gradually increase with the frequency and this is known as normal dispersion. Anomalous dispersion can occur near an interband transition, where the permittivity can rapidly decrease with increasing frequency. Thus anomalous dispersion is usually only present in small spectral regions which overlap the Lorentzian absorption peaks in the imaginary part of the permittivity.

Loss is the absorption of electromagnetic radiation by a material. Strongly absorbing materials are deemed lossy. There are many mechanisms which cause loss in a material, relating to all the different processes by which radiation can be absorbed. The effect of loss is an exponential decrease in the intensity of an incident light wave as it passes through the lossy material (attenuation). This can be modelled by an imaginary component to the permittivity. Materials that are described by the Drude model have absorption peaks, and so the lossy component of the permittivity is dispersive.

Accounting for a lossy surrounding medium complicates the analysis of electromagnetic fields. For the case of a nanoparticle in a surrounding lossy medium, the simple cross section formulas of both Rayleigh theory (3.22)- (3.23) and Mie theory (3.27)- (3.28) have to be adapted to describe the scattered and absorbed light. The values of these quantities become dependent on the distance from the nanoparticle in a lossy medium. When dealing with lossy materials, it is better to use the

extinction cross section, rather than the separate absorption and scattering cross sections because the extinction cross section remains independent of the distance from the scattering center [133, 138].

3.1.3 Linewidth

The linewidth of a plasmon is given by the full-width at half max (FWHM) of the scattering cross section. Near to the resonance, the scattering cross section takes on a Lorentzian form:

$$\sigma_{scat} \approx \frac{\Gamma/2}{(\omega - \omega_0^2) + \Gamma^2/2}, \tag{3.20}$$

where Γ is the linewidth of the peak, and w_0 is the spectral location of the maximum. Using materials described by the Drude-Lorentz model, Γ is exactly equal to the collision frequency γ. For quantum mechanical systems, Γ is estimated by the decay rate of the excited state, which can be derived from the energy-time uncertainty principle: $\Delta E \Delta t \geq \hbar$. In general, the linewidth can be calculated using:

$$\Gamma = \frac{2\hbar}{T_2}, \tag{3.21}$$

where T_2 is the total plasmon decay time [10]. As the decay time is reduced by the addition of losses then the linewidth increases. Thus, material losses by electromagnetic absorption, which is just one form of additional losses, are widely believed to broaden plasmon resonances [158, 159, 160, 10, 107, 106, 117].

Plasmonic materials make desirable optical sensors which detect the presence of a small concentration of a particular molecule by measuring a shift in the resonance peak due to the accompanied change in the refractive index of the surrounding medium. A narrow linewidth plasmon is believed to make a better sensor as the figure of merit (FOM) is given by [78]: FOM $= \frac{\text{Sensitivity}}{\text{FWHM}}$. The quality factor is another measure of resonant systems in general and is given by $Q = \frac{\omega_{\text{res}}}{\text{FWHM}}$ with ω_{res} being the resonant frequency. A high Q is often desirable in resonant systems and this is usually the case in nanoplasmonics.

Radiation damping [93], surface scattering [87], and bulk damping broaden the plasmon linewidth, reducing the FOM and quality factor. Radiation damping, in which the plasmon oscillations lose energy by radiating light, is proportional to the volume of the nanoparticle and so becomes a significant factor to the loss for larger nanoparticles. Surface scattering, the scattering of the plasmons by the surface of the metal nanoparticle, is inversely proportional to the radius of the nanoparticle and is important to consider for small nanoparticles for which radiation damping is small. Lastly, bulk damping due to collisions of the oscillating free electrons in the metal nanoparticle also reduces the plasmon linewidth.

3.1.4 Extinction

Given a material permittivity, how can the total electromagnetic field be calculated? This question was first answered by Lord Rayleigh in 1871 [161], and is a difficult

question to answer, with analytical solutions existing only for the simplest scenarios. To arrive at a description of the interaction between light and matter, Rayleigh analyzed particles much smaller than the wavelength of incident light. For small particles, the phase of the field over the particle can be assumed to be constant (quasi-static approximation), so at each instant in time, the particle experiences the same field everywhere within its volume. Using this assumption, Rayleigh calculated the scattering and absorption cross sections of a small spherical particle in an infinite and homogeneous surrounding medium:

$$C_{\text{scat}} = \frac{1}{6\pi}\left(\frac{2\pi}{\lambda}\right)^4 \left|\frac{\alpha}{\epsilon_0}\right|^2, \tag{3.22}$$

$$C_{\text{abs}} = \frac{2\pi}{\lambda}\text{Im}\left(\frac{\alpha}{\epsilon_0}\right). \tag{3.23}$$

Here, λ is the incident wavelength, α the dipole polarizability and $\epsilon_0 = 8.85 \times 10^{-12}$ is the permittivity of free space. The scattering cross section, C_{scat}, is a measure of how much electromagnetic energy propagates in a different direction from the initial incident field direction, while the absorption cross section, C_{abs}, is a measure of how much light remains within the volume of the particle; how much light is absorbed. The extinction cross section $C_{ext} = C_{scat} + C_{abs}$ is a measure of the combination of the absorption and scattering processes, and quantifies the total loss of forward scattered light due to the particle and medium. These cross sections have units of

area and give an effective size of the particle, separate from its physical size. A larger cross section indicates a stronger light-matter interaction with the particle. Often, the scattering and absorption cross sections are normalized to the target area (the physical cross-sectional area of the particle). The scattering process (ignoring absorption) is elastic so that the incident photon and scattered photon have the same energy. This is the difference between Rayleigh and Raman scattering, in which the scattered photon will gain (anti-Stokes) or lose (Stokes) an amount of energy depending on the molecular/atomic transitions that are excited in the scattering body.

Rayleigh scattering theory explained some atmospheric phenomena such as the colour of rainbows and why the sky was blue. Scattered light has a strong inverse dependence on the wavelength of light, $C_{\text{scat}} \propto 1/\lambda^4$, so smaller wavelength light is scattered much more than longer wavelength light. Then at any position in the sky, there is more blue light reaching your eye than any other colour due to the larger scattering of high frequency light. The interesting frequency dependence from Eqs. (3.22) and (3.23) is hidden within the formula for the dipole polarizability of a sphere

$$\alpha = 4\pi a^3 \epsilon_{\text{CM}} \epsilon_0. \tag{3.24}$$

where a is the radius of the particle and ϵ_{CM} is the Clausius-Mossotti factor:

$$\epsilon_{\text{CM}} = \frac{\epsilon_1 - \epsilon_2}{\epsilon_1 + 2\epsilon_2} \tag{3.25}$$

where ϵ_1 is the permittivity of the sphere and ϵ_2 is the permittivity of the surrounding medium. Notice that this equation has a pole in the complex plane when $\epsilon_1 = -2\epsilon_2$, and the dipole polarizability and scattering and absorption cross sections become infinite. This is known as plasmonic resonance. In most cases, this condition cannot be met exactly because both the particle and surrounding medium have positive imaginary permittivities. In this case, there is still a resonance peak in the scattering and absorption cross sections when the Fröhlich condition is met:

$$\mathrm{Re}\{\epsilon_1\} = -2\mathrm{Re}\{\epsilon_2\}. \tag{3.26}$$

Rayleigh scattering theory could very accurately describe the interaction of small ($ka \ll 1$) particles with light, but a new theory was needed to describe the light-matter interaction of larger particles. In 1907, Gustav Mie generalized Rayleigh's scattering and absorption cross sections for any sized spherical particle [130, 131]. By allowing the field to vary over the volume of the particle, the charge distribution within the particle could now have components of quadrupole, octopole and all higher order charge distributions. Each of the different charge distributions get excited in different amounts by an incident field and each have a different effect on the scattering and absorption of light, unlike for Rayleigh theory, where a material may only have a dipolar charge distribution (due to the constant field in the material). Another important difference between Rayleigh and Mie theory is that light is predominately

scattered in the forward direction, and this forward scattering is increased with the size of the particle. The equations for the normalized cross sections are a little cluttered, but for completeness they are included here (assuming non-magnetic materials, $\mu \approx 1$):

$$Q_{scat} = \frac{2}{k^2 a^2} \Sigma_{n=1}^{\infty} (2n+1)(|a_n|^2 + |b_n|^2), \tag{3.27}$$

$$Q_{abs} = Q_{ext} - Q_{scat}, \tag{3.28}$$

$$Q_{ext} = \frac{2}{k^2 a^2} \Sigma_{n=1}^{\infty} (2n+1)(\mathrm{Re}\{a_n + b_n\}), \tag{3.29}$$

$$a_n = \frac{\epsilon_1 [\rho_2 j_n(\rho_2)]' j_n(\rho_1) - \epsilon_2 [\rho_1 j_n(\rho_1)]' j_n(\rho_2)}{\epsilon_1 [\rho_2 h_n(\rho_2)]' j_n(\rho_1) - \epsilon_2 [\rho_1 j_n(\rho_1)]' h_n(\rho_2)}, \tag{3.30}$$

$$b_n = \frac{[\rho_2 j_n(\rho_2)]' j_n(\rho_1) - [\rho_1 j_n(\rho_1)]' j_n(\rho_2)}{[\rho_2 h_n(\rho_2)]' j_n(\rho_1) - [\rho_1 j_n(\rho_1)]' h_n(\rho_2)}, \tag{3.31}$$

where $\rho_i = k_i a$, with $i = 1$ representing the sphere and $i = 2$ representing the surrounding medium, a is the radius of the sphere, j_n is the spherical Bessel function of the first kind, h_n is the spherical Hankel function of the first kind, and $'$ represents a derivative with respect to ρ.

Mie theory was first developed to understand the vibrant colours of colloidal gold nanoparticles. It is commonly used in nanoplasmonics when working with larger nanoparticles, or high frequency light, where Rayleigh theory becomes inaccurate. Mie theory allows for a calculation of the scattering and extinction cross sections over the entire electromagnetic spectrum, as well as the reflection absorption and transmission coefficients. Over the last century it has been developed significantly

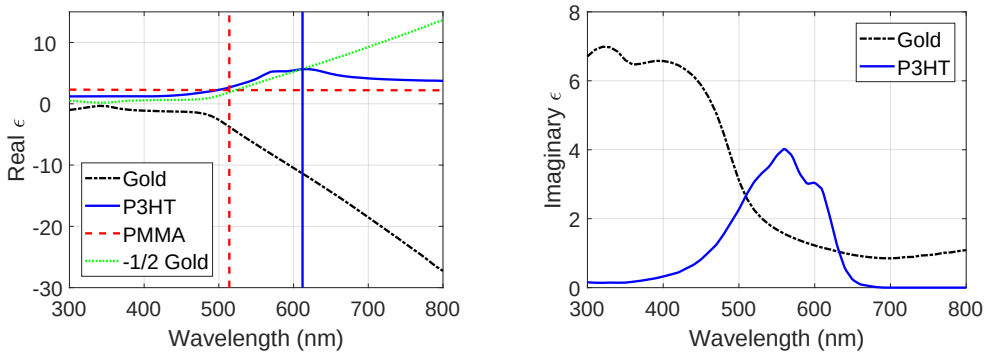

(a) (b)

Figure 3.2: Relative permittivities of gold, P3HT, and PMMA. (a) The real permittivities. The vertical solid blue line corresponds to the plasmon resonance of gold and P3HT at 612 nm determined from the Clausius-Mossotti factor described below. The vertical dashed red line corresponds to the plasmon resonance of gold and PMMA at 514 nm determined from the Clausius-Mossotti factor. (b) The imaginary permittivities. The imaginary part of the permittivity of PMMA is nearly zero.

and applies to a broad range of scattering problems. In 1912, Richard Gans extended Mie theory to apply to spheroidal nanoparticles [162]. Mundy, analyzed scattering and absorption of nanoparticles in absorbing media [132] and in a later work by Bohren and Gilra, it was concluded that light scattering could be greatly affected by a strongly absorbing medium [133]. Aden calculated the electromagnetic response of nanoparticles with an external coated layer (nanoshell) [163]. These are just a few of the extensions to Mie theory over the years. With all of these developments, Mie theory remains a powerful tool for characterizing the electromagnetic response of nanoparticles.

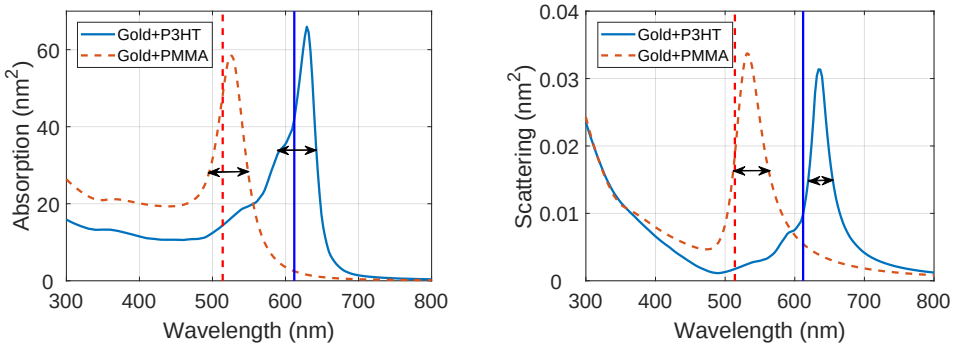

(a) (b)

Figure 3.3: Cross Sections from Rayleigh scattering formulas, Eqs. (3.32)-(3.35). (a) The absorption cross section of a 10 nm gold sphere embedded in P3HT and 10 nm gold in PMMA. (b) The scattering cross section of a 10 nm gold sphere embedded in P3HT and 10 nm gold in PMMA. For both (a) and (b) the vertical solid blue line represents the gold and P3HT plasmon resonance and the vertical dashed red line shows the gold and PMMA plasmon resonance. The black horizontal double arrow lines show the full width at half the maximum of each of the peaks. The gold nanoparticle has a geometric cross section of 7.85×10^{-17} m^2 (πa^2 for a 10 nm diameter gold nanoparticle).

3.2 Scattering in Lossy Dispersive Media

Figure 3.2 shows the permittivities of the materials analyzed in this work. P3HT and gold are both lossy dispersive materials, while PMMA is a non-lossy, non-dispersive material. Figure 3.3 shows the cross sections of a 10 nm diameter gold nanoparticle embedded in PMMA and 10 nm gold in P3HT predicted by Rayleigh scattering theory [161].

For particles much smaller than the wavelength of incident light, the quasi-static approximation holds (vanishing time derivatives in Maxwell's equations) and the physics of light scattering can be accurately described with the Rayleigh scattering

formulas (in SI units)

$$C_{\text{scat}} = \frac{1}{6\pi}\left(\frac{2\pi}{\lambda}\right)^4 \left|\frac{\alpha}{\epsilon_0}\right|^2. \tag{3.32}$$

The scattering cross section, C_{scat}, shows how much of the incident light is scattered from the nanoparticle. There is a strong dependence on the wavelength of incident light, λ, as well as the dipole polarizability of the particle, α

$$C_{\text{abs}} = \frac{2\pi}{\lambda}\text{Im}\left(\frac{\alpha}{\epsilon_0}\right). \tag{3.33}$$

The absorption cross section, C_{abs}, shows how much of the incident light is absorbed from the nanoparticle. In the above equation, Im is the imaginary part of what follows in the brackets. $\epsilon_0 = 8.85 \times 10^{-12}$ is the permittivity of free space

$$\alpha = 4\pi a^3 \epsilon_{\text{CM}} \epsilon_0. \tag{3.34}$$

where a is the radius of the nanoparticle. The quasi-static approximation assumes the incident field is constant over the entire nanoparticle at any given time, and so it breaks down for large particle sizes comparable to the wavelength of incident light, where the fields vary significantly over the volume of the nanoparticle. Within the dipole polarizability is the Clausius-Mossotti factor, ϵ_{CM}, which gives the polarizabil-

ity a dependence on the wavelength of incident light [164],

$$\epsilon_{\mathrm{CM}} = \frac{\epsilon_1 - \epsilon_2}{\epsilon_1 + 2\epsilon_2}. \tag{3.35}$$

When a metal and a dielectric material are used, a plasmon resonance occurs for the wavelength where ϵ_1 (relative permittivity of the metal nanosphere) and ϵ_2 (relative permittivity of the surrounding dielectric medium) maximize ϵ_{CM}. Thus, a plasmon resonance results when the following relation is approximately held:

$$\epsilon_1 = -2\epsilon_2. \tag{3.36}$$

Rayleigh scattering theory was used to find the absorption and scattering cross sections of 10 nm diameter spherical gold nanoparticles embedded in PMMA and P3HT. The vertical lines in Figure 3.2 (a) show the cases where $\mathrm{Re}(\epsilon_1 + 2\epsilon_2) = 0$, which is the real part satisfying Eq. (3.36). Figure 3.2 (b) shows the imaginary part of the permittivity corresponding to losses for P3HT and gold. PMMA is lossless and is therefore not shown.

From Fig. 3.3 it is seen that the resonances are shifted, as expected from the clausius-Mossotti relation. The resonances are not exactly at the position of the vertical line in Figure 3.2 (a) due to the large dispersion in the permittivity. Rayleigh scattering theory predicts plasmon peaks of nearly equal magnitude and a linewidth of

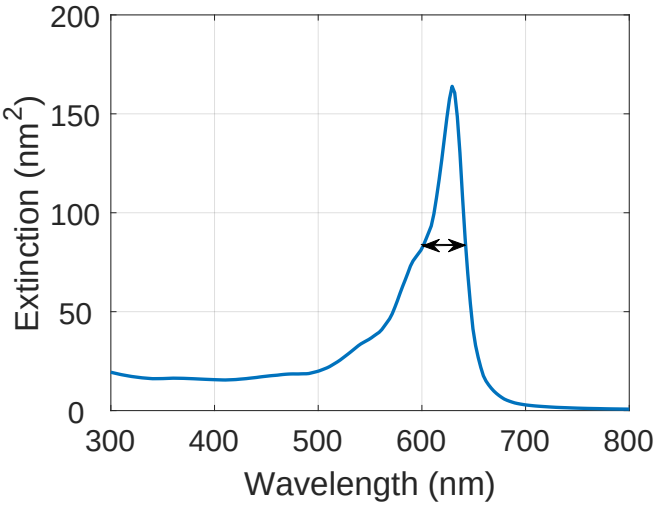

Figure 3.4: Extinction cross section of a 10 nm gold nanoparticle in P3HT.

50 nm for the scattering cross section of gold in PMMA and 35 nm for the scattering cross section of gold in P3HT (the full width at half maximum was used as a measure for the narrowness of the peaks). Care should be taken in analyzing the results of Rayleigh theory when strongly absorbing media are involved because the scattering and absorption become dependent on the distance from the scatterer as losses from the absorbing medium are accumulated. In the case of lossy media, using the full extinction cross section (absorption and scattering) allows for a quantification that is independent of the distance from the scatterer [133, 138, 139, 165]. Figure 3.4 shows the extinction cross section of a 10 nm gold sphere surrounded by P3HT defined previously [133] using

$$C_{\text{ext}} = \frac{6\pi}{\lambda}\text{Im}\left(n_2\frac{m^2-1}{m^2+2}\right), \tag{3.37}$$

where $n_2 = \sqrt{\epsilon_2}$, and $m^2 = \epsilon_1/\epsilon_2$. The extinction cross section does not depend on

the distance from the nanoparticle, as can be seen from Eq. (3.37). The extinction cross section of 10 nm gold in P3HT has a linewidth of 43 nm, while the absorption cross section calculated with Rayleigh theory has a broader linewidth of 53 nm.

3.3 Circuit Model for Lossy Dispersive Media

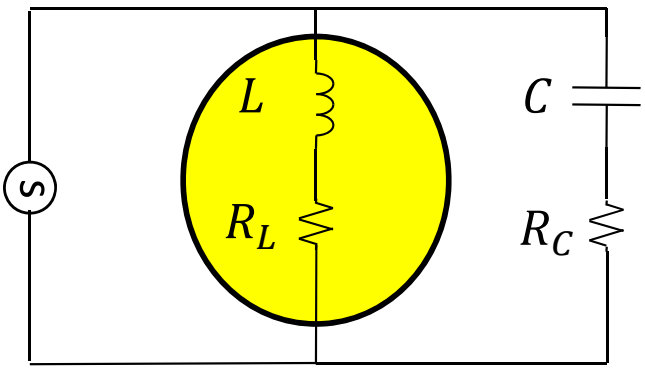

Figure 3.5: Equivalent nanocircuit for a metal nanoparticle surrounded by a lossy medium. The resistances in the circuit are associated with the material loss. If neither material is lossy then the resistances are 0.

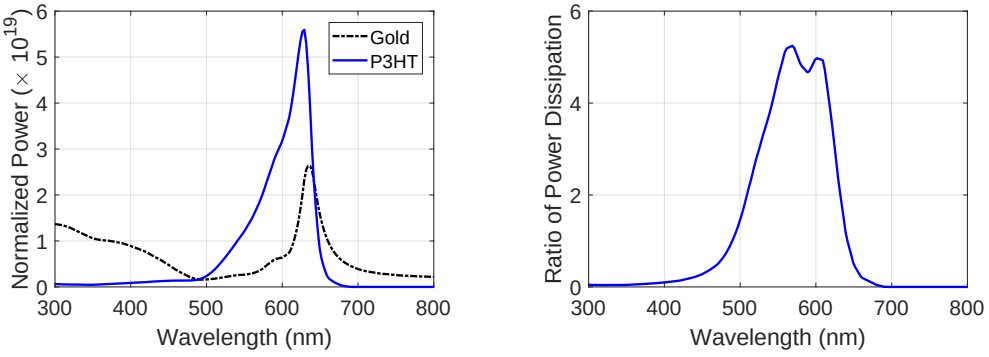

(a) (b)

Figure 3.6: Optical absorption results of a nanocircuit consisting of a 10 nm gold sphere inductor surrounded by a P3HT capacitor. (a) The power absorbed by each circuit element, normalized by the square of the incident field strength $|\mathbf{E}_0|^2$. (b) The ratio of the power absorbed in P3HT to the power absorbed in gold.

Figure 3.5 shows the equivalent nanocircuit for a nanoparticle surrounded by an absorbing material [62]. Both the inductor and capacitor have a resistance associated with them, and power will be dissipated in each of these circuit elements over time. The resistors are placed in series to ensure that each branch represents a different physical material; that is, to avoid shunting. The metal plays the role of an inductor (negative capacitor), while the surrounding medium acts as a capacitor in parallel with the inductor. This nanocircuit describes a gold nanosphere surrounded by P3HT.

Figure 3.6 shows how the power dissipation is partitioned between the gold and the P3HT nanocircuit. The circuit model predicts a sharp peak in absorbed power for the gold and P3HT system. Between 550 and 600 nm, P3HT absorbs five times more power than gold. This shows the effectiveness of adding gold nanoparticles to P3HT for photovoltaic applications, where it is desirable for the surrounding medium to absorb most of the incident light.

The current, impedance, and potential difference in the circuit are given by [62]:

$$I_L = -j\pi a^2 \omega \epsilon_0 \epsilon_1 \epsilon_{\mathrm{CM}} |\mathbf{E}_0| \tag{3.38}$$

$$I_C = -j2\pi a^2 \omega \epsilon_0 \epsilon_2 \epsilon_{\mathrm{CM}} |\mathbf{E}_0| \tag{3.39}$$

$$V = a\epsilon_{\mathrm{CM}} |\mathbf{E}_0|, \tag{3.40}$$

where I_L is the current through the inductor, I_C is the current through the capacitor, V is the potential difference across the circuit, j is the imaginary unit, ω is the incident field frequency, a is the radius of the gold nanoparticle, $|\mathbf{E}_0|$ is the magnitude of the incident electric field and ϵ_1 and ϵ_2 are the relative permittivities of the inductor and capacitor materials. Linear polarization is assumed.

The power absorbed in each element is given by:

$$P_L = I_L^* V = j\pi a^3 \omega \epsilon_0 \epsilon_1 |\epsilon_{\mathrm{CM}}|^2 |\mathbf{E}_0|^2 \tag{3.41}$$

$$P_C = I_C^* V = j2\pi a^3 \omega \epsilon_0 \epsilon_2 |\epsilon_{\mathrm{CM}}|^2 |\mathbf{E}_0|^2. \tag{3.42}$$

When both of the materials are non-absorbing, there is only reactive power (power transferred back and forth between the inductor and capacitor) in the circuit and no power is dissipated, as is expected in an LC circuit without any resistance. For materials with loss there is power dissipation in each of the circuit elements. The circuit model is useful in determining the absorption of light in both the metal and the surrounding medium. The equations used here have been adapted from [62], where the surrounding medium was lossless and therefore, they serve only to roughly estimate the absorption for the case of lossy surrounding media.

3.4 Green Function Theory

Green function calculations were used to find the linewidth of gold nanoparticles in P3HT and PMMA. The theory and code used for these calculations was developed by Professor Stephen Hughes and Dr. Juanjuan Ren [166]. This section explains the details of these Green function calculations. A Green function is the function which gives the Dirac delta function as a solution when substituted into an inhomogeneous differential equation. Once the Green function is known, any general and possibly more complicated inhomogeneous differential equation can be solved by using the Green function. The Green function for Maxwell's equations satisfies

$$\nabla \times \nabla \times \mathbf{G}(\mathbf{r}, \mathbf{r}_0, \omega) - \frac{\omega^2}{c^2}\epsilon(\mathbf{r}, \omega)\mathbf{G}(\mathbf{r}, \mathbf{r}_0, \omega) = \frac{\omega^2}{c^2}\mathbf{1}\delta(\mathbf{r} - \mathbf{r}_0), \tag{3.43}$$

where $\mathbf{G}$ is the dyadic Green function, ω is the angular frequency, $\mathbf{r}$ is the location of the field point of interest, $\mathbf{r}_0$ is the location of the source, c is the speed of light, $\epsilon(\mathbf{r}, \omega)$ is the permittivity, $\mathbf{1}$ is the unit tensor, and δ is the Dirac delta function. The Green function is then separated into scattering and homogeneous medium contributions

$$\mathbf{G} = \mathbf{G}^s + \mathbf{G}^{\text{hom}}. \tag{3.44}$$

The formula for the scattering contribution of the Green function, $\mathbf{G}^s$ used in this thesis can be found in a past work [167]. The Green function spectrum is defined as

$$S_0(\omega) = \left| \frac{1}{\epsilon_0} \mathbf{G}^s(\mathbf{r}, \mathbf{r}_0, \omega) \cdot \mathbf{d} \right|^2, \tag{3.45}$$

where $\mathbf{G}^s$ is the scattering part of the Green function at position $\mathbf{r}$ from the center of the nanoparticle. The source is a dipole polarized in the z direction located at $\mathbf{r}_0$ with dipole moment $\mathbf{d}$ (the z-axis is along the direction from the center of the nanoparticle to the dipole position $\mathbf{r}_0$, and the point $\mathbf{r}$ is past the dipole along the z-axis). The resulting scattered component of the Green function spectrum, $\mathbf{G}^s$, defined here quantifies the power scattered by the nanoparticle.

The calculations were performed with the distance between the field point and the dipole $|\mathbf{r} - \mathbf{r}_0|$ set to 50 nm. The dipole source was placed 4 nm away from the nanoparticle. In experiments, illuminating a nanoparticle with a light source placed far away (which is usually the case, with one exception being near-field optical experiments) is effectively using a plane wave source, not a dipole source, so the Green-function method used here can only approximate what would be expected in experiments. Since the Green function calculations were meant to be compared to experiments, there was an extra renormalization to the calculated scattered power that needed to be done. In experiments, the incident light would pass from air to the surrounding medium, while in calculations the light from the dipole source was generated within the surrounding medium. To account for this, the scattered power

was renormalized

$$S = S_0 \left| \sqrt{\epsilon_{\text{med}}} \right|, \tag{3.46}$$

where ϵ_{med} was the medium permittivity.

3.5 Green Function Analysis

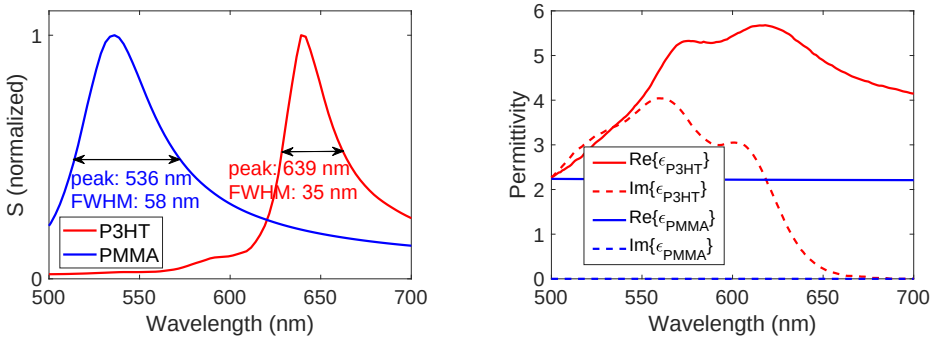

(a) (b)

Figure 3.7: Green function and permittivity data for P3HT and PMMA. (a) Green function spectrum S for a single 20 nm gold nanoparticle in P3HT and PMMA. Surrounding media are assumed to be infinite and homogeneous. (b) Real and imaginary parts of the permittivity of P3HT and PMMA.

To understand the unusually narrow linewidth seen for gold in P3HT, Green function analysis was employed. Figure 3.7 (a) shows the calculated Green function spectrum S, for a single 20 nm gold nanoparticle in both P3HT and PMMA assuming the surrounding medium was infinite and homogeneous. The un-normalized scattering spectrum, found in Appendix A.7, shows that gold in PMMA exhibits more scattering than gold in P3HT. The Green function spectrum for an individual spherical

nanoparticle in a infinite, homogeneous surrounding medium was given by

$$S(\omega) = \left| \frac{1}{\epsilon_0} \mathbf{G}^s(\mathbf{r}, \mathbf{r}_0, \omega) \cdot \mathbf{d} \right|^2 |\sqrt{\epsilon_{\text{med}}}|, \tag{3.47}$$

where ω is the angular frequency of the source, ϵ_0 is the permittivity of free space, ϵ_{med} is the relative permittivity of the surrounding medium, $\mathbf{G}^s$ is the scattered Green function, $\mathbf{r}$ is the location of the field point of interest, $\mathbf{r}_0$ is the location of the point dipole source, and $\mathbf{d}$ is the dipole moment, polarized along the z direction (parallel with the direction defined by the vector connecting the dipole and the center of the nanoparticle). The Green function method goes beyond the common dipole approximation [167] and includes more terms in the multipole expansion. The full infinite series is exact within the context of Maxwell's equations, although in practice only a finite number of terms can be used and there is always some small deviation from the exact solution. The Green function calculations for the linewidths of gold in PMMA and P3HT agree qualitatively with the experimental dark field data shown in Chapter 5; the plasmon linewidth of gold in P3HT is half the linewidth of gold in PMMA.

Figure 3.7 (b) shows the real and imaginary parts of the permittivity of P3HT and PMMA. The permittivity of PMMA is nearly constant from 500 to 700 nm and is effectively non-dispersive. Also, the imaginary part of PMMA is almost zero over this wavelength range and so PMMA is considered lossless. Both the real and imaginary

components of the permittivity of P3HT have a large magnitude and dispersion near the plasmon peak for gold in P3HT (around 640 nm).

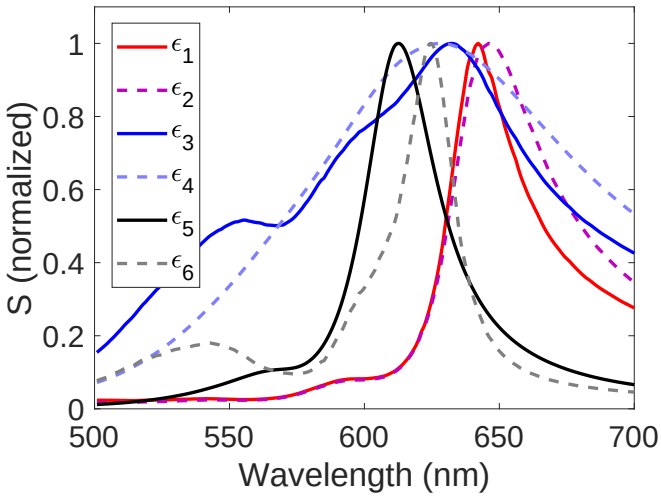

Figure 3.8: Green function spectrum S for a 20 nm gold nanoparticle in various infinite and homogeneous embedding media. The permittivities of the embedding media are: $\epsilon_1 = \epsilon_{\text{P3HT}}$, $\epsilon_2 = 5.2 + \text{Im}\{\epsilon_{\text{P3HT}}\}i$, $\epsilon_3 = \text{Re}\{\epsilon_{\text{P3HT}}\} + 1.5i$, $\epsilon_4 = 5.2 + 1.5i$, $\epsilon_5 = 5.2$ and $\epsilon_6 = \text{Re}\{\epsilon_{\text{P3HT}}\}$. The data is summarized in table 3.1

To investigate how the embedding medium impacts the plasmon linewidth, Green function calculations were performed for gold nanoparticles surrounded by various media. The effects of dispersion on the linewidth are not well documented in the literature and most works assume there is no dispersion in the surrounding medium. Although this is usually a good approximation for commonly used embedding materials, for materials with large dispersion such as P3HT, the assumption is no longer valid. Thus the permittivities with wavelength dependence are considered in order to find the effects of the dispersion on the plasmon peak. Figure 3.8 shows the Green function spectra for a single 20 nm gold nanoparticle in various homogeneous infinite

Permittivity	Description	Peak	Linewidth
$\epsilon_1 = \epsilon_{\mathrm{P3HT}}$	actual material	642 nm	35 nm
$\epsilon_2 = 5.2 + \mathrm{Im}\{\epsilon_{\mathrm{P3HT}}\}i$	dispersive imaginary component	646 nm	47 nm
$\epsilon_3 = \mathrm{Re}\{\epsilon_{\mathrm{P3HT}}\} + 1.5i$	dispersion, constant loss	632 nm	110 nm
$\epsilon_4 = 5.2 + 1.5i$	no dispersion, constant loss	628 nm	127 nm
$\epsilon_5 = 5.2$	no dispersion, lossless	613 nm	33 nm
$\epsilon_6 = \mathrm{Re}\{\epsilon_{\mathrm{P3HT}}\}$	dispersion, lossless	624 nm	22 nm

Table 3.1: Summary of plasmon peaks calculated from Green function spectra for 20 nm gold in various infinite and homogeneous embedding media. The scattering spectra for the permittivities listed in this table were calculated using Mie series expansions. When only five terms were used in the series expansions, the resulting linewidths were accurate to three decimal digits. The displayed linewidths were calculated using 23 terms and there is negligible numerical error in these values.

embedding media. Although some of the dielectric functions used are unphysical and do not obey the sum rules [168] and the Kramers-krönig relations [140, 141], they are nevertheless utilized to conveniently isolate the linewidth response for a specific change in permittivity (for example, taking the physical material permittivity and then removing loss). Table 3.1 shows the peak wavelengths and linewidths for each of the plasmon peaks in Fig. 3.8. In the following analysis, the different contributions of an infinite and homogeneous embedding medium permittivity to the linewidth, including dispersive effects in the real and imaginary parts of the medium permittivity are explained. The case of finite surrounding medium layers was analyzed with FDTD simulations and show there is only a small dependence of the plasmon peak on the layer thickness (for more details, see Appendix A.3). Also, a Green theory analysis was used to find how the size and permittivity of the metal nanoparticle affect the linewidth (Appendix A.4 and A.5). The Green theory analysis of the embedding medium permittivity indicated that four factors were important to the linewidths

of the plasmons. These factors are: the magnitude of both the real and imaginary parts of the permittivity, and the dispersion of the real and imaginary parts of the permittivity near the plasmon peak.

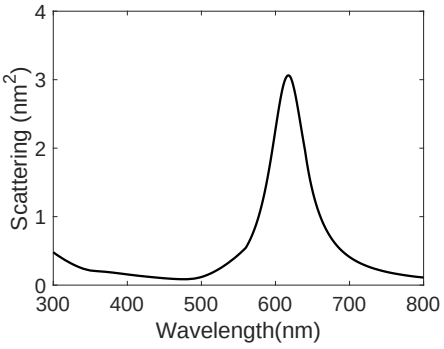

(a)

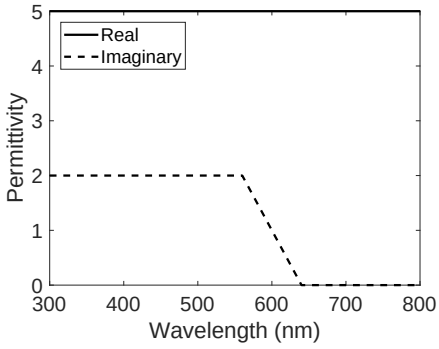

(b)

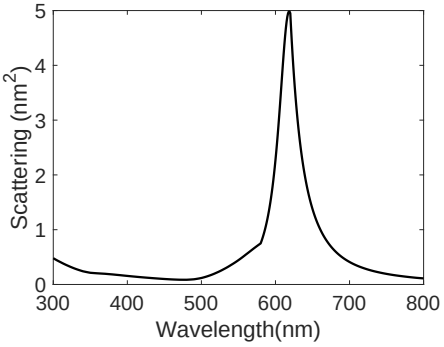

(c)

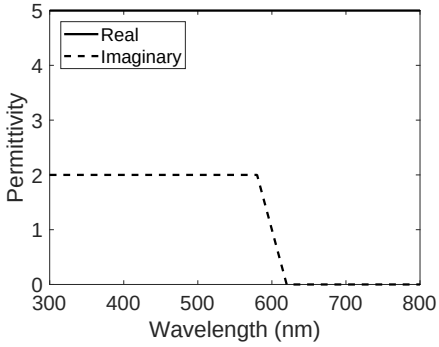

(d)

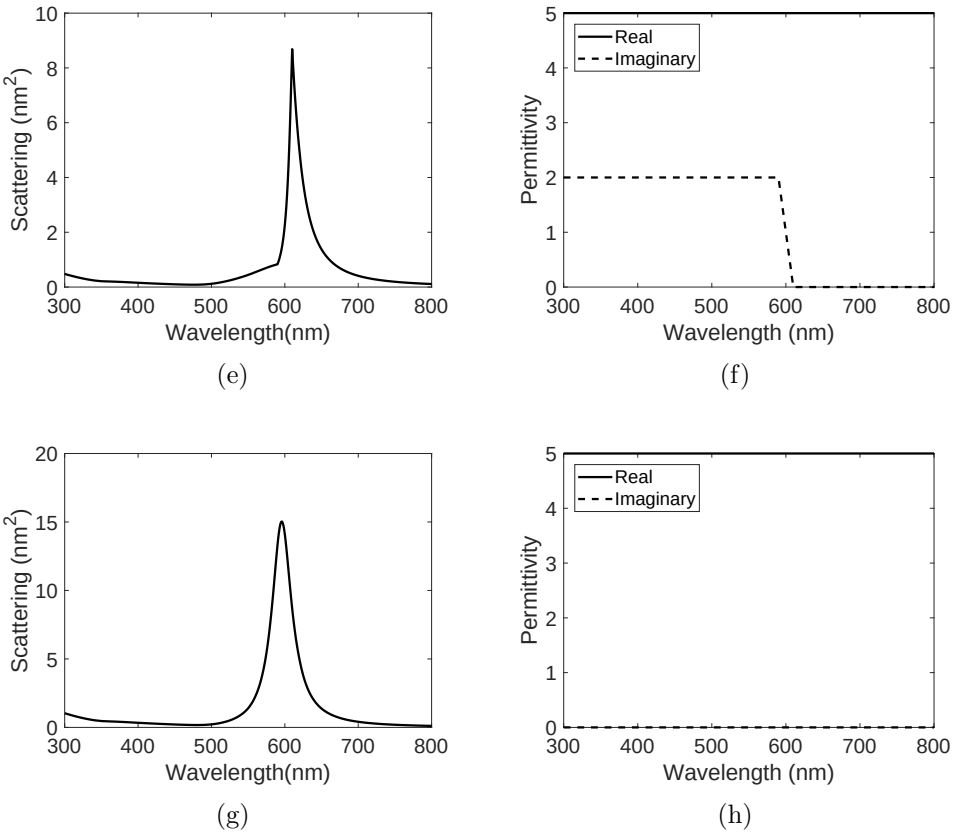

Figure 3.8: Effect of sharpness of semiconductor band edges on the linewidth of a plasmon peak. Band edges assumed to be linear for simplicity. All cross sections are calculated with Rayleigh scattering theory for a 10 nm gold nanoparticle. (a) Rayleigh scattering cross section of a 10 nm gold nanoparticle in a semiconductor with a broad band edge. The linewidth is 57 nm. (b) Real and imaginary parts of the permittivity of the broad band edge semiconductor. (c) Rayleigh scattering cross section of a 10 nm gold nanoparticle in a material with a sharp band edge. The linewidth is 32 nm. (d) Real and imaginary parts of the permittivity of the sharp band edge semiconductor.(e) Rayleigh scattering cross section of a 10 nm gold nanoparticle in a material with a very sharp band edge. The linewidth is 17 nm. (f) Real and imaginary parts of the permittivity of the very sharp band edge semiconductor. (g) Rayleigh scattering cross section of a 10 nm gold nanoparticle in a lossless dielectric. The linewidth is 32 nm. This is a broader linewidth than the very sharp band edge semiconductor. (h) Real and imaginary parts of the permittivity of the lossless dielectric. The real permittivity is 5 and the imaginary part is 0.

Dispersion in the imaginary part of the permittivity near the plasmon peak resulted in linewidth narrowing. Fig. 3.8 shows that the left edges of the plasmon peaks

for both $\epsilon_1 = \epsilon_{\mathrm{P3HT}}$ and $\epsilon_2 = 5.2 + \mathrm{Im}(\epsilon_{\mathrm{P3HT}})i$ are the steepest. Near the plasmon peak, where the Fröhlich condition,

$$\mathrm{Re}(\epsilon_1) = -2\mathrm{Re}(\epsilon_2) \tag{3.48}$$

for gold (ϵ_1 in the above formula) in P3HT (ϵ_2 in the above formula) is satisfied (611 nm), the absorption of P3HT rapidly decreases which is accounted for in the permittivity by a dispersive imaginary part. Table 3.1 shows that the lossless materials in general had narrower linewidths than the lossy materials. However, the presence of a dispersive loss component near the plasmon peak noticeably narrowed the linewidth. P3HT has loss at the plasmon peak, and so it has a broader peak than the lossless materials. Although there is little absorption in P3HT at the plasmon peak, nearby the peak there is significant loss and dispersion. The presence of the large dispersion of the loss near the peak is a contributing factor to the narrow linewidth for gold in P3HT. The right edges of the plasmon peaks for $\epsilon_1 = \epsilon_{\mathrm{P3HT}}$ and $\epsilon_2 = 5.2 + \mathrm{Im}(\epsilon_{\mathrm{P3HT}})i$ are not as steep due to the lack of a dispersive imaginary permittivity here. Then an ideal medium for narrowing plasmon linewidths would have very dispersive loss that rapidly goes to zero at the plasmon peak, and this should result in an even narrower peak than a lossless medium with the same real permittivity. This trivial addition of dispersion and loss to an existing material, however, is unphysical; changes in the real and imaginary parts of the permittivity are linked

through the Kramers-krönig relations [140, 141]. With physical materials in mind, there are other semiconductors apart from P3HT, that exhibit sharp band edges resulting in dispersive loss. For example, GaAs, InAs and Ge all are quite lossy and dispersive semiconductors. Then, with the addition of an ideal metal nanoparticle, the plasmon peak would occur near this band edge, and a significant narrowing of the plasmon peak would be expected. Figures 3.8 (a) - (h) show the effects that a sharp semiconductor band edge can have on the plasmon peak. The permittivities used in the scattering calculations are not realistic, they were chosen to clarify the effect dispersion of the imaginary permittivity on the plasmon peak. It is clear that dispersion in the imaginary part of the permittivity of the surrounding medium can narrow linewidths.

Although dispersive loss can narrow linewidths, non-dispersive loss leads to broader plasmon linewidths. To separate the effects of dispersive and non-dispersive loss on the linewidth, the Green function spectra for lossy background materials with and without dispersive loss were calculated. As seen in Fig. 3.8, the materials with constant loss ($\epsilon_3 = \mathrm{Re}(\epsilon_{\mathrm{P3HT}}) + 1.5i$, $\epsilon_4 = 5.2 + 1.5i$) have much broader linewidths than the materials with dispersive loss ($\epsilon_1 = \epsilon_{\mathrm{P3HT}}$, $\epsilon_2 = 5.2 + \mathrm{Im}(\epsilon_{\mathrm{P3HT}})i$) and with no loss. From this evidence, it is concluded that non-dispersive loss broadens linewidths.

Dispersion in the real part of the medium permittivity, which arises near a lossy resonance, can also contribute to narrowing the plasmon peak. Comparing the plasmon peaks for $\epsilon_1 = \epsilon_{\mathrm{P3HT}}$ and $\epsilon_2 = 5.2 + \mathrm{Im}(\epsilon_{\mathrm{P3HT}})i$ in Fig. 3.8, the right edge of the

peak for $\epsilon_1 = \epsilon_{\mathrm{P3HT}}$ is steeper than the right edge of the peak for $\epsilon_2 = 5.2 + \mathrm{Im}(\epsilon_{\mathrm{P3HT}})i$. Figure 3.7 (b) shows that the real part of $\epsilon_1 = \epsilon_{\mathrm{P3HT}}$ decreases near the plasmon peak. The permittivity of gold becomes more negative for wavelengths larger than 600 nm. The Fröhlich condition (Eq. (3.48)) shows that at the resonance peak, decreasing ϵ_1 and ϵ_2 will result in a more rapid movement away from the resonance as the wavelength changes resulting in a smaller linewidth. This is what is causing the steep right edge for the $\epsilon_1 = \epsilon_{\mathrm{P3HT}}$ plasmon peak. Therefore, a dispersive real permittivity can narrow plasmon peaks.

The magnitude of the real part of the permittivity can also narrow plasmon linewidths. In Fig. 3.8, the $\epsilon_5 = 5.2$ peak yields a relatively narrow linewidth. The real permittivity of gold becomes more negative and dispersive for longer wavelengths. For larger ϵ_2 the Fröhlich condition (Eq. (3.48)) is satisfied at longer wavelengths. Redshifting a plasmon peak can reduce the losses from interband transitions in gold [87]. Then by redshifting the plasmon peak into the large dispersion and low loss regime of gold, not only is loss from gold reduced, which narrows the peak, but also the Fröhlich condition is swept through faster, further reducing the linewidth. Therefore, a large real permittivity can significantly narrow plasmon linewidths. The narrowest peak was obtained for $\epsilon_6 = \mathrm{Re}(\epsilon_{\mathrm{P3HT}})$, which has both a large permittivity and large dispersion. Importantly, the addition of the large dispersion to the permittivity causes a narrower peak than the $\epsilon_5 = 5.2$ peak, supporting the claim that a dispersive real permittivity can narrow plasmon peaks.

As a response to these findings, Mishchenko and Dlugach theoretically investigated the far-field scattering spectra of metal nanoparticles in a lossy medium [160]. They looked at 10 nm spherical nanoparticles of gold, silver, aluminum and sodium and used a medium permittivity similar to water, but with a lossy component. The absorption of the lossy medium was adjusted gradually by changing the imaginary component of the permittivity of the medium, and it was found that more absorption lead to broader resonance and reduced resonance peaks for all of the nanoparticles. The authors noted this was in contrast to the results of my work, which showed a narrowing of the resonance peak for gold nanoparticles in a lossy medium. However, the missing ingredient, which these authors also acknowledged, is that the surrounding medium in their work is non-dispersive. The results shown in this chapter agree with theirs in the case dispersion is ignored; there is a large broadening of the linewidth when the medium is lossy and non-dispersive. However, it has also been shown here that when dispersion is included, the plasmon peak can be narrowed even when the medium is lossy.

Very recently, Khlebtsov has analyzed plasmonic nanoparticles in lossy media [169]. He showed that there are inaccuracies and inconsistencies in previous attempts of understanding scattering within lossy media. He derived equations for both the near-field and far-field scattering cross sections in a lossy medium. He also analyzed gold nanoparticles in P3HT and PMMA, and compared his results to our previous work [166]. His findings agree quantitatively with ours, showing that the lossy P3HT

has a narrower linewidth than PMMA. He found a linewidth of 33.6 nm for 10 nm gold in P3HT and 53.8 nm for 10 nm gold in PMMA. His work furthers our understanding of plasmonics in lossy media and confirms the results and conclusions presented in this thesis.

3.5.1 Perovskite Green Function Analysis

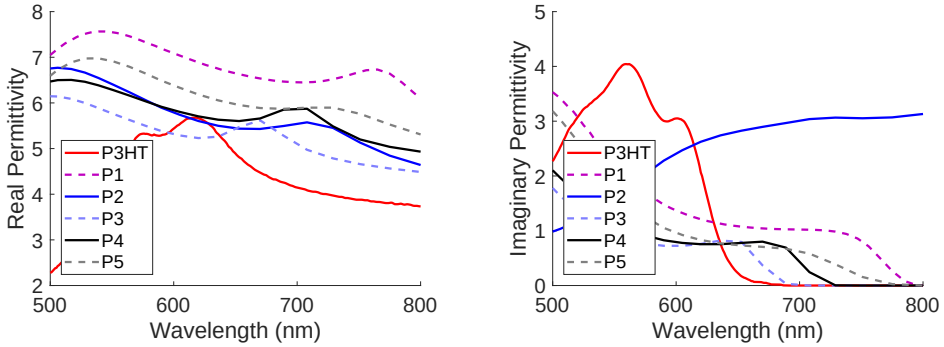

(a) (b)

Figure 3.9: Permittivities of different perovskites. (a) Real permittivities. (b) Imaginary permittivities.

Material	Peak	Linewidth
P3HT	642 nm	35 nm
P1 = $CH_3NH_3PbI_3$	661 nm	80 nm
P2 = $CsBr10\%1:2$	627 nm	184 nm
P3 = $CsCl17\%0:1$	618 nm	97 nm
P4 = $CsI15\%0:1$	632 nm	74 nm
P5 = $CsI15\%1:2$	643 nm	65 nm

Table 3.2: Summary of plasmon peaks calculated from Green function spectra for 20 nm gold in different perovskites. The scattering spectra for the permittivities listed in this table were calculated using Mie series expansions.

Figure 3.10 shows the Green function analysis for perovskites, which are a high efficiency alternative to silicon solar cells. The perovskite permittivies shown in Fig. 3.9

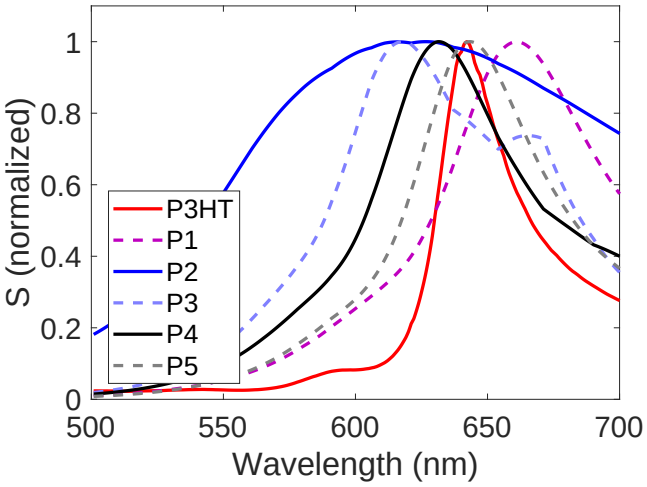

Figure 3.10: Green function spectrum S for a 20 nm gold nanoparticle in perovskites. The data is summarized in table 3.2.

were found from experiments [170, 171]. These perovskites are known to be very dispersive, so there was hope that they might yield narrower cross sections than gold nanoparticles in P3HT. However, as seen in table 3.2, the linewidths are much larger for the perovskites, even though they are lossy and dispersive like P3HT. These theoretical results show the importance of the location of the dispersion in narrowing the linewidth; a lossy and highly dispersive material is not enough to guarantee a narrow linewidth. The reason P3HT has such a narrow linewidth is because the permittivity, both real and imaginary components, change rapidly over the spectral region of the plasmon peak. This does not happen for the perovskites that were analyzed here and so the result is a broader linewidth. So it may prove difficult to find other materials which display such a narrow linewidth as P3HT, since many conditions need to be met. Namely, the material needs to be lossy, and have dispersive imaginary and real

components, and both of these must result in a rapidly changing permittivity near the spectral region of the plasmon peak.

3.5.2 Organic Photovoltaics

Organic photovoltaics (OPV) is a field of research that studies photovoltaic devices made with organic materials. An OPV cell functions similarly to an inorganic cell with only a few distinguishing differences. Rather than p-type and n-type doping of silicon which generates different electron and hole concentrations, OPVs make use of donor and acceptor materials. The donor has both a larger highest occupied molecular orbital energy level (HOMO) and lowest unoccupied molecular orbital energy level (LUMO) than the acceptor. When light is absorbed in the donor material, it generates an exciton (an electrostatically bound electron-hole pair). Due to the difference in HOMO and LUMO levels in the donor and acceptor, it is energetically favourable for the holes to remain in the donor, while the electrons move into the acceptor. This results in a flow of electrons from donor to acceptor. By adding conductive contacts at each end of the device and connecting them with a wire, a current can be maintained through the circuit. Organic materials are often much better at absorbing light than inorganic materials, and thinner layers can be used to absorb the same amount of light. However, the charges generated are not as mobile in organic materials, and so often there is a significant loss in efficiency due to the charges not being collected by the conductive contacts.

Organic photovoltaics is a relatively new field of research; the first OPV device was created in 1979 by Tang [172, 173], and it converted incident light into electrical power at an efficiency of 1%. The first donor-acceptor heterojunction cell was developed in 1993 [174] and had less than 1% efficiency. Although the efficiency of the device was low, the concept of using a donor polymer and acceptor polymer was promising for making higher efficiency cells. In 1995, PCBM ([6,6]-phenyl-C61-butyric acid methyl ester) was used as a donor in an OPV cell and it was found to enhance charge separation, charge transport and exciton dissociation, resulting in an efficiency of 2.9% [175]. Since 2018, the world record OPV cell is 17.4% efficient, but had an area less than 1cm^2 [176]. For larger area OPV cells, which are commercially viable, the largest measured efficiency is 12.6% for a 26 cm^2 cell [177].

The Shockley-Quessier limit is the maximum theoretical efficiency of an ideal, single-junction solar cell assuming only radiative losses [178]. The Shockley-Quessier limit is reached for a material with a band gap of 1.4 eV with a maximum efficiency of 33%. This is close to the 1.1 eV band gap of silicon and is partially why silicon makes a good solar cell, which has a Shockley-Quessier limit of 29%. The most efficient silicon cell has a remarkable 26.7% efficiency, and is very close to theoretical limit [179]. However, there is a large difference between the reported efficiencies of cells created in the lab and the usual 15-20% efficiency of cells that are commercially available [180]. The highest efficiency cells in the lab are usually very small (less than 1 cm^2), and don't suffer extra series resistance and cell interconnection losses.

Also, more expensive material deposition techniques like spin coating and FIB milling (focused ion beam) are not used in the manufacturing process for commercial cells, and instead less precise methods such as roll to roll printing must be used. There are methods to increase solar cell efficiencies beyond the Shockley-Quessier limit, such as singlet fission, where multiple excitons are generated from a single photon [181]. Efficiencies greater than 33% are routinely reported by using multi-junction cells with multiple layers, each layer tailored to absorb a separate portion of the solar spectrum [182]. However, multi-junction cells also have theoretical limits due to radiative losses, albeit much larger than single-junction cells. For a 2 and 3 layer cell, the maximum theoretical efficiencies are 42% and 49% respectively [183]. The main problem with using multi-junction cells is that the device becomes more timely and costly to make.

OPVs have have short lifetimes, typically ranging from a couple months up to about 2 years, even when encapsulated [184]. Silicon cells are much more durable and usually last 25 years. Degradation mechanisms of OPV cells are still being studied, but it is known that many organic polymers can lose their ability to absorb light if exposed to air or water [185]. Why use OPVs at all if they cannot reach the efficiencies of silicon cells and have shorter lifetimes? OPVs have several advantages over silicon cells, and can exist in niche markets, such as flexible cells, and painted cells. They also have the potential to be much cheaper to produce. Although the raw material cost for P3HT versus silicon is much larger, the production of silicon

cells is timely and expensive. It is thought that once OPVs can reach 10% efficiency and last 10 years, then roll-to-roll printing of OPVs will become competitive with silicon [186, 187].

The first major improvement to the efficiency of OPVs came from the development of bulk heterojunction (BHJ) cells, in 1992 [188]. BHJ cells utilize a single layer where both the donor and acceptor materials are mixed together. Before BHJs were used, the donors and acceptors were stacked together with a single planar interface separating the donor layer and the acceptor layer. BHJs drastically increased the surface area in which the donor and acceptor are in contact and also reduced the distance the charges travel from the donor to the acceptor. The use of BHJs provided a way to compensate for the short diffusion lengths observed in organic materials (P3HT has a diffusion length of only 5 nm). This short diffusion length is due to the typically small permittivities of organic materials, which cause a large binding energy of the generated excitons (0.3-1 eV) [189]. This means increasing layer thickness is not a valid pathway to increase efficiency; it doesn't matter how many excitons are generated in the cell if none can dissociate into an electron and hole and be collected by the metal contacts on either end of the cell. Ultrathin layers ($\approx$10 nm) were used, so that most of the charges generated are collected. But the trade off for better charge transport is less absorption. With the addition of BHJs thicker layers could be used due to the enhancement of the charge transport properties, and so this would further increase cell efficiency. One major drawback to BHJs is that although the charges can

efficiently be moved from the donor to the acceptor, due to the randomly generated structure of the BHJ layer, the charges do not always have a clear path from the acceptor to the back contact, where they must go to be collected and provide power to an external circuit. This problem can be avoided with nanofabrication techniques, however this also raises the cost and time of producing the cells.

Due to the low carrier mobility, the active layer of OPVs are typically only 100 nm or less. This means that even with their strong light absorption, much of the light is not absorbed and is transmitted through the cell. Thus OPV can benefit greatly from plasmonic enhancement. Plasmonic enhancement uses metal nanostructures or films, which make use of the plasmon resonance to increase the PCE of the OPV. There are many ways which plasmonic enhancement of the cell can occur. By incorporating metal nanoparticles into the active layer of the cell, the field is enhanced in the absorbing material surrounding the metal nanoparticles. This field enhancement results in a large increase in absorption at and nearby the plasmon resonance. Larger metal nanoparticles can also be included near the front and rear contacts to increase light scattering into the active layer. This also increases the path length of light in the active layer which increases absorption. The increase in path length comes from the increase in high angle light due to scattering in the presence of the metal nanoparticles. Without the nanoparticles, the light path would not bend and would take a short path through the active layer through the back contact. Lastly, erbium upconversion is another popular method of increasing the efficiency of solar cells. About half of

the sunlight reaching a solar cell is below the band gap of silicon. OPVs typically have even higher energy band gaps than silicon, so this is even more of a problem for them. By adding erbium nanoparticles to a solar cell, much of this low energy light can be converted into useful higher energy light which can be absorbed by the solar cell. This process happens a number of ways, but the simplest is by absorption of two 1520 nm photons in an erbium atom, which results in the 980 nm emission which is then below the bandgap of silicon. Erbium upconversion is a promising method of increasing the efficiency of the cell by making use of incident light that would be otherwise just pass through the solar cell. Furthermore, this can be combined with plasmonic enhancement of the cell by addition of gold nanoparticles.

3.5.3 Erbium Upconversion Enhancement

A recent work has shown the enhancement of erbium emission when placed in close proximity to gold nanorods [1]. There was a significant bright mode enhancement, and somewhat surprisingly, a dark mode enhancement of the emission was also noted. This is surprising because the dark mode does not typically couple to radiation and although there is an expected near-field enhancement, the far-field emission is not expected to be enhanced. One way to explain this enhancement was that there were multiple erbium emitters nearby to each gold nanorod, and that the emitters were emitting at different times. Having multiple emitters nearby, but emitting at different times could mean that the dark mode would be excited and the emitters would not

destructively interfere with each other, so that there would be an overall enhancement of the far-field signal at the dark mode. However, simulations were performed with FDTD in which the time between emission for two dipoles at opposite ends, 10 nm from the tip of a gold nanorod, was gradually changed, and there was no observed change in the emission at the dark mode. It was noted that the Purcell factor for a single dipole excited at the bright mode was about 1000 while the dark mode is about 200. This was interesting because in the experimental data, the bright mode and dark mode emission enhancements are similar. In the simulations, the erbium atoms were simply treated as dipole sources. However, erbium is much more complicated with a variety of atomic levels that can absorb and emit. We then thought to explain this enhancement of the dark mode radiation by solving the rate equations for an erbium atom. It was possible that by enhancing the bright mode emission of erbium, this could in turn also enhance the dark mode emission. Below is the model of the erbium atom used, as well as the rate equations which were solved in steady state.

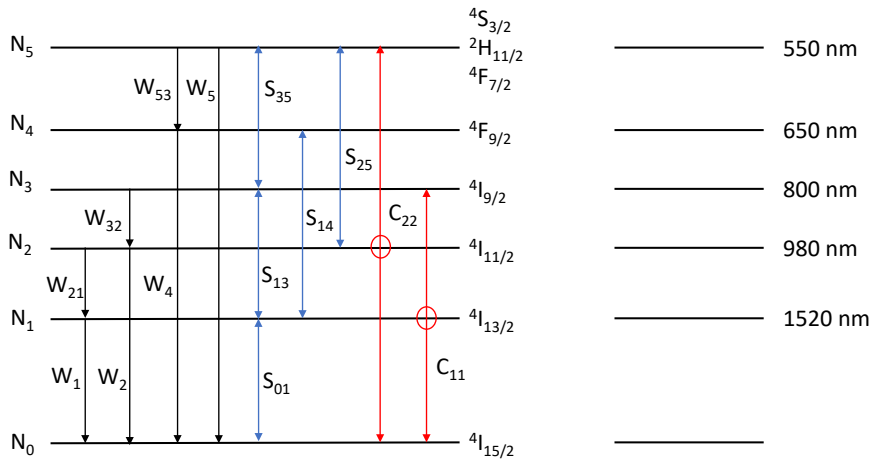

Figure 3.11: The model used to solve the rate equation for the erbium atom. The W's represent spontaneous emission, the S's are either 1520, or 1210 nm stimulated emission and absorption, and the C's are co-operative upconversion terms. The red circles show which levels the co-operative upconversion process occurs.

$$\frac{dN_0}{dt} = W_1N_1 + W_2N_2 + W_4N_4 + W_5N_5 + S_{10}N_1 + C_{11}N_1^2 + C_{22}N_2^2 \tag{3.49}$$

$$\frac{dN_1}{dt} = -W_1N_1 + W_{21}N_2 + S_{01}N_0 - S_{10}N_1 + S_{31}N_3 - S13N_1 + S_{41}N_4 - S_{14}N_1 - 2C_{11}N_1^2 \tag{3.50}$$

$$\frac{dN_2}{dt} = -W_2N_2 - W_{21}N_2 + W_{32}N_3 + S_{52}N_5 - S_{25}N_2 - 2C_{22}N_2^2 \tag{3.51}$$

$$\frac{dN_3}{dt} = -W_{32}N_3 + S_{13}N_1 - S_{31}N_3 + S_{53}N_5 - S_{35}N_3 + C_{11}N_1^2 \tag{3.52}$$

$$\frac{dN_4}{dt} = -W_4N_4 + S_{14}N_1 - S_{41}N_4 \tag{3.53}$$

$$\frac{dN_5}{dt} = -W_5N_5 + S_{25}N_2 - S_{52}N_5 + S_{35}N_3 - S_{53}N_5 + C_{22}N_2^2 \tag{3.54}$$

$$N = N_0 + N_1 + N_2 + N_3 + N_4 + N_5 \tag{3.55}$$

Where W_{ij} is the spontaneous decay rate from level i to level j, γ_{br},γ_{dr}, γ_{bt} and γ_{dt}

are the radiative bright mode enhancement, radiative dark mode enhancement, bright mode Purcell factor, and dark mode Purcell factors respectively. The factors γ_{br},γ_{dr}, γ_{bt} and γ_{dt} were found in FDTD simulations, and simulate the modification of the atomic processes by the field enhancement from the presence of gold nanorods. The bright mode occurs at 980 nm and the dark mode occurs at 650 nm, so any processes occurring at these wavelengths were modified by the corresponding enhancement factor. Explicitly, W_{2r} was modified by a factor of γ_{br}, W_{4r} was modified by a factor of γ_{dr}, W_2 and C_{22} were modified by a factor of γ_{bt} and W_4 was modified by a factor of γ_{dt}. N_i is the number of electrons in level i, N is the concentration of erbium atoms being pumped, and S_{ij} is the rate of photons involved in the stimulated emission or absorption processes. S_{01}, S_{13} and S_{35} are excited with 1520 nm illumination and S_{14} and S_{25} are excited with 1210 nm illumination.

Table 3.3 shows the values of all of the coefficients needed to calculate the plasmon enhancement factor from gold nanorods. The W_r terms are the purely radiative spontaneous decay rates. $W_{r1}N_1$ gives the number of 1520 nm photons emitted, $W_{r3}N_3$ gives the number of 980 nm photons emitted, and $W_{r4}N_4$ gives the number of 650 nm photons emitted.

As seen in Fig. 3.12 agree qualitatively in the behaviour of the levels between theory and experiment for 1520 nm pumping. In particular, both the 650 nm and 980 nm emissions are linear in the case of only 1520 nm excitation. When there is dual excitation, there is a second order dependence for 980 nm emission and a third order

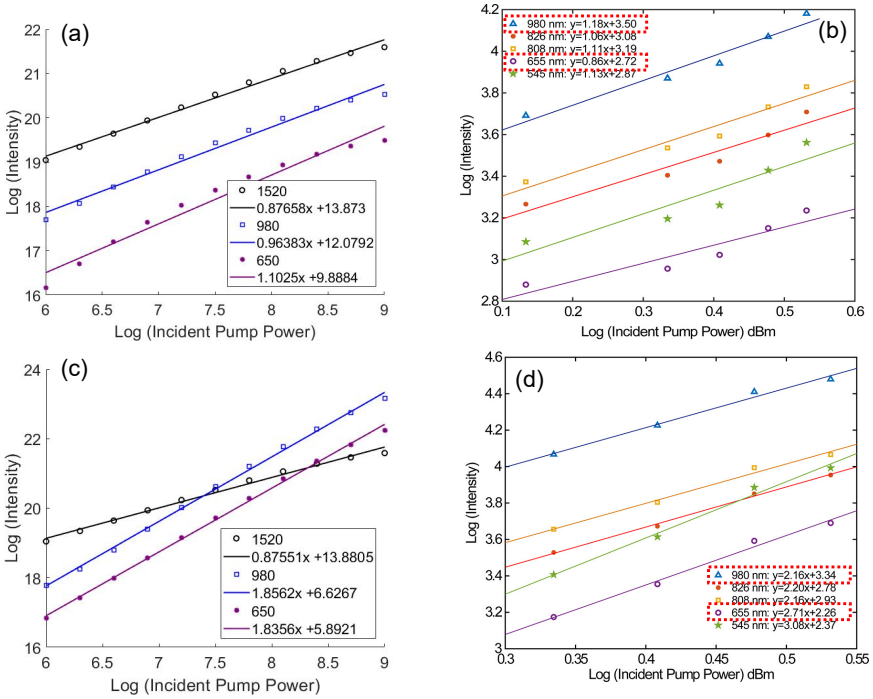

Figure 3.12: A comparison between the experimental results from [1] and the rate equation model used here for 1520 nm excitation only, and simultaneous 1520 nm and 1210 nm excitation. (a) Rate equation results for 1520 nm excitation. (b) Experimental results for only 1520 nm excitation. (c) Rate equation results for 1520 and 1210 nm dual excitation. (d) Experimental results for 1520 and 1210 nm dual excitation.

dependence for 650 nm emission, on the incident power in experiments. The rate equations only predict a second order dependence on both the 980 nm and 650 nm emission.

From Fig. 3.13 it is seen that the bright mode is expected to be enhanced by a large factor of around 30, while the dark mode is actually reduced. This differs significantly from the experimental results, where a 30 % enhancement at the dark mode and only a 55 % enhancement at the bright mode is seen. With such a large discrepancy it would be easy to conclude that the atomic model fails to explain the

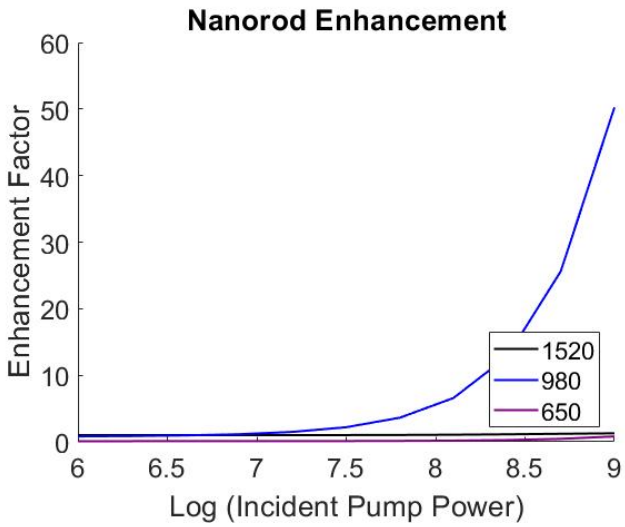

Figure 3.13: Enhancement of emission of erbium atoms due to the presence of gold nanorods at the bright and dark modes.

dark field phenomenon, however this is not necessarily true. There are many values in Table 3.3 and it is possible some of these differed in the experiments compared to the values shown in the table. With enough adjustment of the coefficients it is possible the same bright field and dark field emission enhancement is seen in theory and experiment. Then if this is achieved, the next step would be to explain why the coefficients differ in the experiments. More work needs to be done with the atomic model theory for erbium to before it should be ruled out.

3.6 Conclusion

The basic theories pertaining to this thesis were covered in-depth in this chapter. Rayleigh theory was used to calculate the absorption and scattering cross sections for 10 nm gold nanoparticles in P3HT and PMMA and it was found that P3HT had about

half the linewidth as PMMA. Green theory was used to further investigate the reason for this surprisingly narrow linewidth in a lossy medium. It was found that dispersion in both the real and imaginary parts of the permittivity of the surrounding medium plays a vital role in narrowing the linewidth. Lastly, in another research project, the unexpected enhancement of far field radiation at the dark mode from erbium emitters nearby gold nanorods was investigated. The theory hypothesizes that this dark mode far field enhancement comes from an enhanced near field due to the gold nanorod and enhancement of atomic transition rates in erbium that emit at the dark mode. Though the calculations did not match well with experimental data, more work needs before this theory should be rejected. There is a large parameter space that needs to be explored before it can be said that the theory fails to explain experiment.

Coefficient	Value
W_1	$1e8$
W_2	40000
W_4	500000
W_5	100000
W_{21}	5000
W_{32}	10000
W_{54}	10000
W_{1r}	121
W_{2r}	116
W_{4r}	1028
γ_{br}	340
γ_{dr}	11
γ_{dt}	940
γ_{bt}	236
S_{01}	$6e-21$
S_{10}	$6e-21$
S_{13}	$6e-21$
S_{31}	$6e-21$
S_{35}	$6e-21$
S_{53}	$6e-21$
S_{14}	$1e-21$
S_{12}	$1e-21$
S_{25}	$1e-21$
S_{52}	$1e-21$
C_{11}	$4e-22$
C_{22}	$2e-20$

Table 3.3: These were the values of the coefficients in the rate equation used to calculate the plasmonic enhancement factor at the bright and dark modes. The values shown here are the coefficient values before modification from field enhancement of the bright and dark modes.

Chapter 4

Simulations

4.1 Gold Nanoparticle Scattering in P3HT

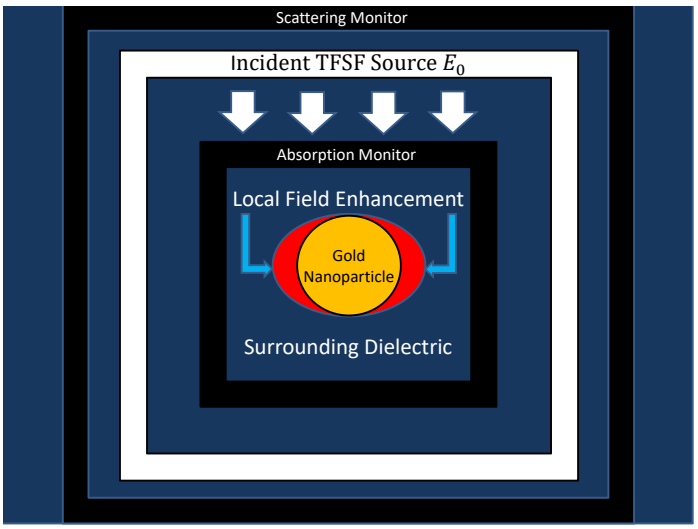

Figure 4.1: 2D representation of the layout of the FDTD simulations used for this work.

Figure 4.1 shows a schematic representation of a finite-difference time-domain (FDTD) simulation for calculating the absorption and losses associated with a gold

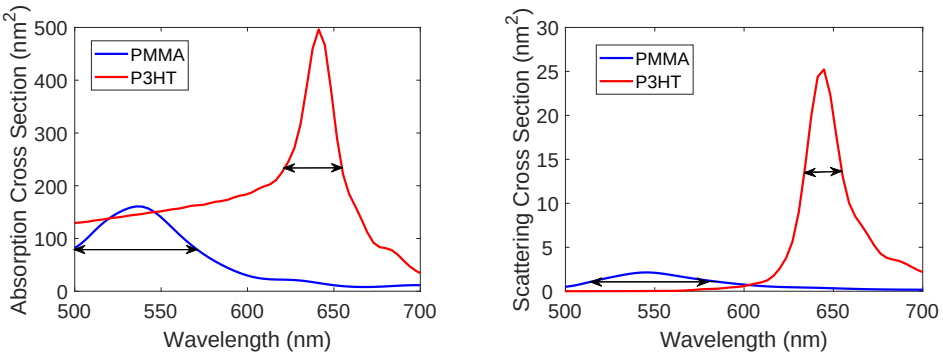

Figure 4.2: Cross Sections calculated from FDTD simulations. The black horizontal double arrow lines show the full width at half the maximum of each of the peaks. (a) The absorption cross sections of a single 10 nm gold sphere in P3HT and PMMA. (b) The scattering cross sections of a single 10 nm gold sphere in P3HT and PMMA.

nanoparticle in a (lossy) dielectric medium. A commercial package, Lumerical FDTD version 8.21.1854, was used for these simulations. The simulation region consists of a 10 nm diameter gold nanoparticle surrounded by a dielectric material. There is a box of 2D power monitors of side length 17.5 nm to measure absorbed power, a total-field scattered-field source (TFSF) with side length 25 nm and another box of 2D power monitors to measure the scattering with a 250 nm side length. The TFSF source emits light in the range of 300 to 1000 nm. The TFSF source was injected in the y-axis and polarized in the z-direction. The simulation used a time step of 0.002 fs and a 0.5 nm mesh was used within the TFSF region. The mesh refinement type used was conformal variant 1 for faster convergence on the boundary of the gold nanoparticle. Symmetric boundary conditions were used to significantly reduce simulation time. The default 8 layer PML (perfectly matched layer) boundary was used for the FDTD simulation boundaries.

Figure 4.2 shows the cross section data for each of the FDTD simulations. Rayleigh scattering theory and FDTD simulations yield similar cross sections for PMMA; however, for the lossy P3HT, they are different. The absorption cross section peak of gold in PMMA and of gold in P3HT are comparable in magnitude when using Rayleigh scattering theory, but in the FDTD simulations P3HT has an absorption cross section peak that is three times larger than PMMA. The reason for this discrepancy is that Rayleigh scattering theory and the simulations calculate the cross sections at different positions relative to the nanoparticle, and these cross sections change for lossy media. Rayleigh theory operates in the far-field regime while the simulations had monitors relatively close to the nanoparticles and within what would be considered the near-field regime. For a lossy medium, if the far-field has a comparable absorption cross section to a non-lossy medium, then in the near-field region the electromagnetic field must be larger in the lossy medium. This is because the fields are being reduced in magnitude by absorption in the medium as they propagate, so if they end at similar magnitudes, they must have started off larger in the lossy medium, and so there is more absorption in the near-field compared to the far-field for lossy media. It was recently found by Khlebtsov that the magnitude of the electric field of gold nanoparticles in P3HT is much larger than for PMMA nearby the gold nanoparticles [169]. Rayleigh scattering theory also predicts scattering cross section peaks for gold in PMMA and gold in P3HT that are similar in magnitude. In the FDTD simulations, the P3HT scattering cross section peak is an order of magnitude larger than

the PMMA scattering cross section peak. The large shoulder from 500 to 600 nm in the absorption cross section is accounted for by the absorption of P3HT surrounding the gold, as this region of the spectrum is where P3HT is strongly absorbing. This was verified with a simulation where the absorption monitor and TFSF source had their dimensions reduced, resulting in a reduction in the shoulder.

An interesting result from the FDTD simulations is the large scattering peak of gold and P3HT. In general, it is expected that absorption dominates the scattering process for small particles. This is considered in photovoltaics where larger nanoparticles are used to scatter light to increase the optical path length within the device, whereas smaller nanoparticles directly enhance absorption of light in the device [156]. Eqs. (3.32)- (3.34) quantify this phenomenon;

$$C_{\text{abs}} \propto a^3 \tag{4.1}$$

$$C_{\text{scat}} \propto a^6. \tag{4.2}$$

For 10 nm gold in P3HT, the scattering cross section is still an order of magnitude lower than the absorption cross section. It seems possible that for a metal-dielectric composite with a large enough scattering peak, there may not be an absorption dominant regime for wavelengths near the plasmon peak. Having small particles which both absorb and scatter effectively could be useful in solar cell applications, where the particles would increase the optical path and light absorption simultaneously.

Apart from the large magnitude of scattering, there was also a significant narrowing of the linewidth for gold in P3HT. This linewidth narrowing was unexpected as lossy materials typically broaden plasmon linewidths. Some sense can be made by considering how material dispersion can affect the plasmon peak. Figure 3.2 shows that gold is very dispersive for wavelengths larger than 500 nm, P3HT is dispersive from 300 to 650 nm and PMMA is effectively non-dispersive. The large dispersion in both P3HT and gold leads to rapid variations in the Clausius-Mossotti factor and thereby result in narrower plasmon peaks. The numerator of Eq. (3.35) is often ignored, but for small resonance linewidths this term can become significant. For the ideal narrow cross section, the dispersion of the nanoparticle and surrounding medium would be such that moving off resonance would result in changing the Clausius-Mossotti from the maximum directly to a minimum. Minima in both scattering and absorption cross sections exist when the Clausius-Mossotti factor is 0. So, if for some combination of nanoparticle and surrounding medium $\epsilon_1(\lambda_1) \approx \epsilon_2(\lambda_1)$ then the permitivitties move towards $\epsilon_1(\lambda_2) \approx -2\epsilon_2(\lambda_2)$ and then again the permitivitties move back to $\epsilon_1(\lambda_3) \approx \epsilon_2(\lambda_3)$ in a short wavelength span $\Delta\lambda = \lambda_3 - \lambda_1$, then the dispersion of each of the materials is serving to narrow the plasmon linewidth. In general, larger material dispersion means the Clausius-Mossotti maximum is swept through in a reduced wavelength range and the result is a narrower plasmon resonance.

These FDTD simulations show that a lossy medium surrounding a metal nanoparticle can narrow the plasmon resonance as well as increase the magnitude of the peak.

The observed peak narrowing agreed with calculations using Rayleigh scattering theory; however, the latter is not suitable for obtaining accurate results when considering lossy media, and underestimates the peak narrowing and magnitude enhancement. The extinction cross section is more suitable to compare, and using the extinction cross section as seen in the theory chapter, Eq. (3.37),there is good agreement between the theory and the simulations still. The simulations agree well with the quasistatic response, as shown in Fig. (3.3) when there is no loss in the surrounding material, but the results differ for the lossy P3HT.

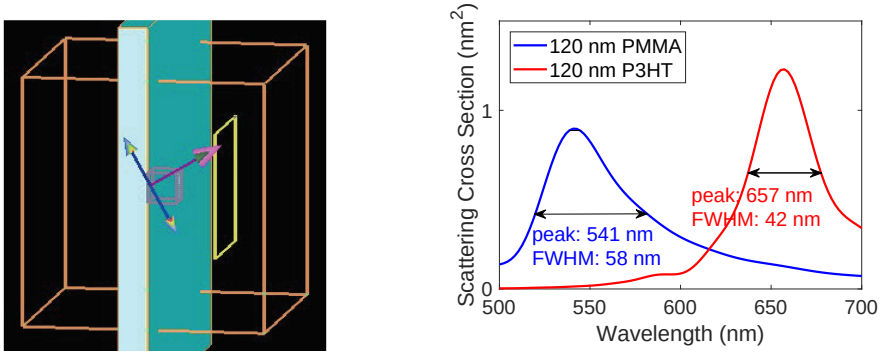

(a) (b)

Figure 4.3: FDTD numerical simulation data. (a) A schematic of the FDTD simulation. The blue box is a 120 nm thick layer of PMMA, with a 20 nm diameter gold nanoparticle in the center. The large orange box is the simulation region, the small pink box is the TFSF source and it is contained in the blue box and contains the gold nanoparticle. The yellow square is the field monitor where the scattered field was measured. (b) Scattering cross section calculated with FDTD from a 20 nm gold nanoparticle in a 120 nm thick PMMA layer and a 120 nm thick P3HT layer.

Lumerical version (8.20.1731) was used to perform further FDTD calculations. The goal of these calculations was to simulate a scattering signal that would be compared to actual dark field scattering measurements. Figure 4.3 (a) shows a schematic

of the simulations. A total-field scattered-field (TFSF) source was used with a 50 nm side length which illuminated the sample at an angle of 30°. The angle was important because most dark field microscopes have an angled source so that the transmitted light is not collected, and only scattered light is measured/imaged. The wavelength range of the source was 400-800 nm. The sample was modeled by a 20 nm gold nanoparticle at the center of a 120 nm thick rectangle of P3HT or PMMA, which extended through the simulation boundaries. PMLs boundaries were used and were 16 layers thick to more effectively absorb high angle scattered light. The simulation region was a 1000 nm cube. A single power monitor was placed outside the sample and the TFSF region to measure the scattered power. The gold permittivity used in the simulations was fitted to Johnson and Christy data [146], the P3HT permittivity was fitted to experimental data collected from the McGehee Stanford research group [190], and the PMMA permittivity was 2.25. Convergence of all simulations was checked by gradually decreasing the mesh size. The simulations for the data shown in Fig. 4.3 (b) used a 1 nm mesh in the gold nanoparticle region and a 3 nm mesh in the surrounding medium.

Figure 4.3 (b) shows the results of the FDTD simulations for the scattering cross section of 20 nm gold nanoparticles encased in a 120 nm layer of PMMA and P3HT. Comparing Fig. 4.2 (b) for 10 nm particles and Fig. 4.3 (b) for 20 nm showed that the 20 nm particles simulations resulted in broader linewidths for both PMMA and P3HT layers. Both simulations agreed that the linewidth of gold nanoparticles in P3HT is

half of those in PMMA. There were a few differences in how the simulations were performed which affect the measured linewidth and the size of the particle was only one of these factors. How the size of a nanoparticle changes the plasmon resonance is well known already from Mie theory, and so there was no need to investigate this with the simulations. In the simulations done for the 20 nm particle, most of the transmitted light did not go through the scattering monitor, similarly to how a dark field microscope measures only the scattered light. This is why the magnitude of the scattering signal is much smaller for the 20 nm simulation compared to the 10 nm simulation (Fig. 4.2). In the 10 nm simulation, a box of transmission monitors captures all of the scattered and transmitted light, whereas only a single monitor captures some of the forward scattered light for the 20 nm simulations. This is comparable to how a collective objective would gather a large amount of the forward scattered light to be detected with a camera or spectrometer in a dark field microscope. Simulations were done with different film thicknesses to show that the thickness of the film did not change the plasmon peak appreciably (see Appendix A.3).

4.2 Nanorod Emission Enhancement

Figure 4.4 shows the schematic of the FDTD simulations performed to find the emission enhancement an erbium nanoparticle would experience near a gold nanorod. A simple staircase mesh was used with a mesh size of 1 nm. A Dipole source was used

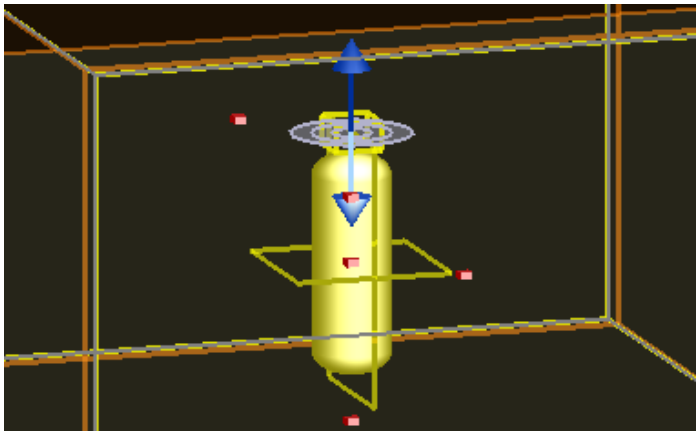

Figure 4.4: Schematic of the FDTD simulation. The orange box is the simulation boundaries, the yellow boxes are transmission monitors. There are two transmission boxes, one is small and surrounds only the dipole source, and the other is nearly as large as the simulation region, and surrounds both the dipole source and the gold nanorod. The dipole source was placed 10 nm from the tip of the gold nanorod and used an incident wavelength of 300-1500 nm.

to model the erbium emitter, which was placed 10 nm from tip of a gold nanorod and emitted from 300-1500 nm. The gold nanorods in the simulations used the same dimensions as the BBI solutions nanorods which were used in experimental measurements [1]. The nanorods were 119 nm long and 25 nm in diameter. The gold permittivity used for the nanorod was taken from Palik. FDTD boundaries were PML and symmetric boundary conditions were used on the x and y boundaries to drastically reduce simulation time. A field monitor was used to measure the field inside and nearby to the gold nanorod, while a 15 nm box of transmission monitors centered around the dipole measured the Purcell enhancement, and a 240 nm box of transmission monitors surrounding both the nanorod and the dipole source measured the radiative emission.

Figures 4.5 (a) and (b) show the bright and dark modes of the gold nanorods. The

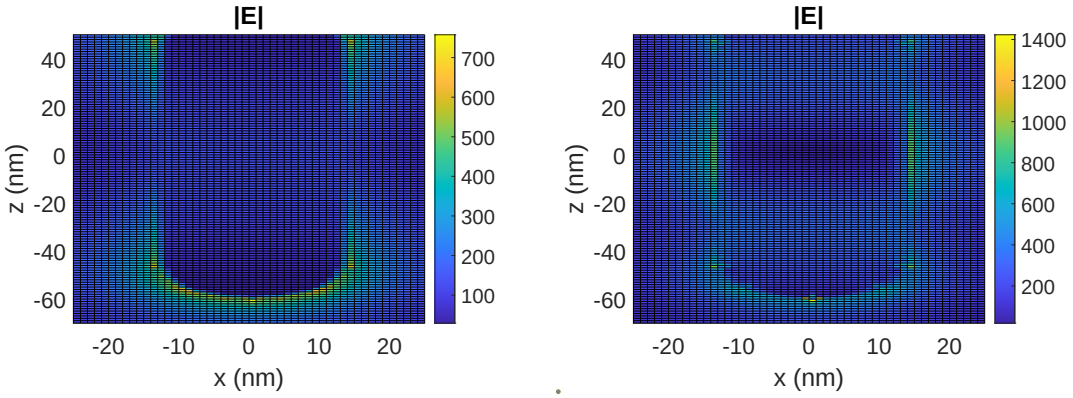

(a) (b)

Figure 4.5: Field profiles of the bright and dark modes of the gold nanorods used in experiments. (a) Bright mode at 980 nm. (b) Dark mode at 600 nm.

dimensions of the gold nanorods were set from the gold nanorods used in experiments, which had a bright mode at 980 nm. The field profile clearly shows the excitation of the bright mode of the gold nanorod at 980 nm. The dark mode at 600 nm is also excited by the dipole source.

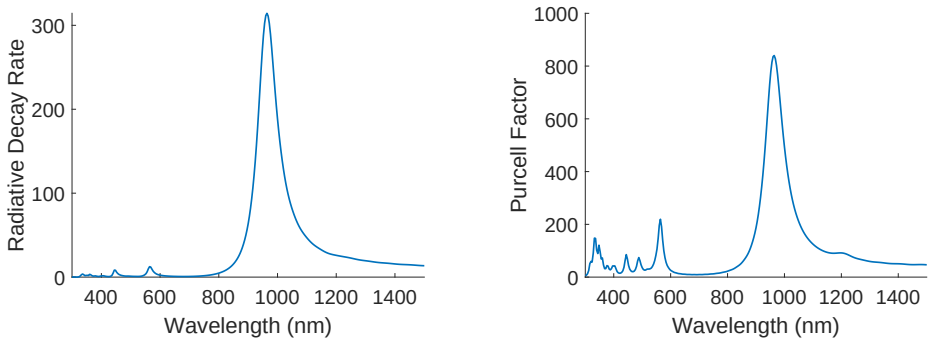

(a) (b)

Figure 4.6: FDTD simulation results for the radiative and Purcell Enhancement factors of a dipole source nearby a gold nanorod. (a) Radiative enhancement factor. (b) Purcell Factor.

Figures 4.6 (a) and (b) show the radiative and Purcell enhancement factors. The radiative enhancement factor was found by measuring the scattered power with a

box of transmission monitors surrounding the nanorod and dipole source. Similarly, the Purcell factor was found by measuring the transmission through a small box of transmission monitors enclosing only the dipole source. Both of these were normalized by the incident power the dipole source would radiate, without the gold nanorod present, to find the enhancement factors. As expected with a dark mode, the radiative enhancement factor is small because dark modes do not easily couple to radiation. The radiative enhancement factor is 11 for the dark mode compared to 300 for the bright mode. The Purcell factor for the dark mode is 225 and the Bright mode is 900. These values were used in the theoretical calculations for the rate equations for the erbium atom.

4.3 Conclusion

Two sets of simulations using Lumerical FDTD were performed with one set more focused on matching Rayleigh theory calculations and the other tailored towards experiments that will be covered in the next chapter. All of the simulations show a significantly narrower peak for gold in P3HT than for gold in PMMA matching with the predictions of Rayleigh theory. Simulations in Lumerical FDTD were also performed for the erbium dark mode enhancement project and both the Purcell and radiative enhancement factors were calculated. These values were used in the theory to calculate the dark mode emission enhancement factor.

Chapter 5

Experiments

5.1 Sample Preparation

Experiments were designed with the hopes of measuring some interesting properties of the scattering cross section for gold nanoparticles in a lossy dispersive medium. The samples consisted of gold nanoparticles encased in a thin layer of either P3HT or PMMA. P3HT was used as the lossy dispersive material, as an unusually narrow linewidth and large magnitude plasmon peak were predicted [191]. The non-lossy, non-dispersive PMMA was used as a control. The scattering cross section of each sample would be measured with a dark field microscope.

Figure 5.1 (a)-(d) shows how the samples were made. First a bottom layer of material (either P3HT or PMMA) was spin coated onto a clean glass slide, then gold nanoparticles were drop coated with a micropipette on top of the bottom layer.

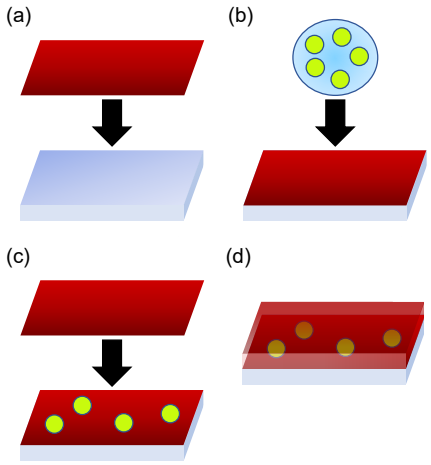

Figure 5.1: (a)-(d) Sample Preparation. (a) Spin coat bottom layer. (b) Drop coat gold nanoparticles. (c) Spin coat top layer. (d) Gold nanoparticles encased in thin layer of surrounding material.

Clean glass slides were prepared by sonication in an ethanol bath for 10 minutes, then sonication in an acetone bath for 10 minutes. The 50μL drops were heated on a hot plate for 10 minutes until the drops evaporated, leaving a small area of gold nanoparticles on the surface of the sample. Finally, the top layer of material was spin coated on the sample. The result was nanoparticles encased within a thin layer of the spin coated material. The PMMA solution used was 4% PMMA in anisole. The P3HT used in this experiment was 90% regioregular P3HT from Rieke metals (4002-EE).

A 12 mg/mL P3HT:toluene solution was mixed together in a nitrogen atmosphere glovebox to prevent the degradation of the P3HT, and was spin-coated at 3500 RPM, with 10 s acceleration and deceleration time, and 20 s spin time to form a 120 nm thick layer [192]. P3HT forms a mixture in toluene and to dissolve it, solutions

were placed on a hot plate at 75°C for two hours and stirred with a stir bar until they became a bright orange color. The dissolved solutions were then filtered with a 0.2 μm filter to remove any P3HT macromolecules and impurities. The resulting solution was spin coated immediately upon removal from the hot plate to prevent the P3HT from polymerizing in the toluene. If allowed to polymerize, the solution changed from orange to dark purple and was much more viscous, altering the spin coating properties.

P3HT can form both J-aggregate and H-aggregate structures [42, 193, 194], which have characteristically narrow scattering peaks. The spin coated layers consisting of P3HT in the samples were neither J- nor H-aggregates as these narrow peaks were not observed in samples of P3HT alone (see Appendix A.6).

5.2 Measurements

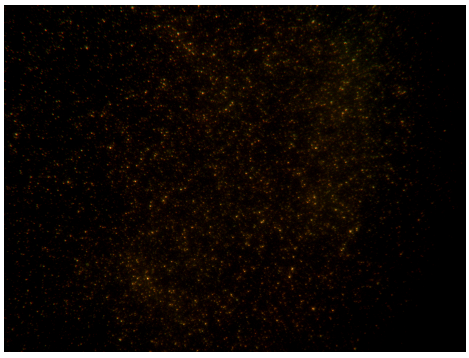

Figure 5.2: 20 nm spherical gold nanoparticles drop coated on a glass slide and imaged with a CytoViva dark field microscope.

Figure 5.2 shows a typical dark field microscope image of 20 nm gold nanoparticles

drop coated onto a clean glass slide. The commercially available CytoViva dark field microscope was used to measure the scattering cross section of gold nanoparticles. This microscope has a 1 nm spectral resolution and was used to measure the scattering spectra of gold nanoparticles in the spectral range of 400-1000 nm. This microscope can be used to see gold nanoparticles as small as 10 nm in diameter. The samples measured were gold nanoparticles on a clean glass slide with either no coating, or coated in PMMA or P3HT.

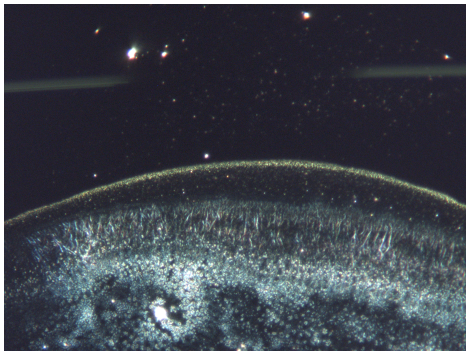

Figure 5.3: 10 nm gold in 100 nm thick PMMA.

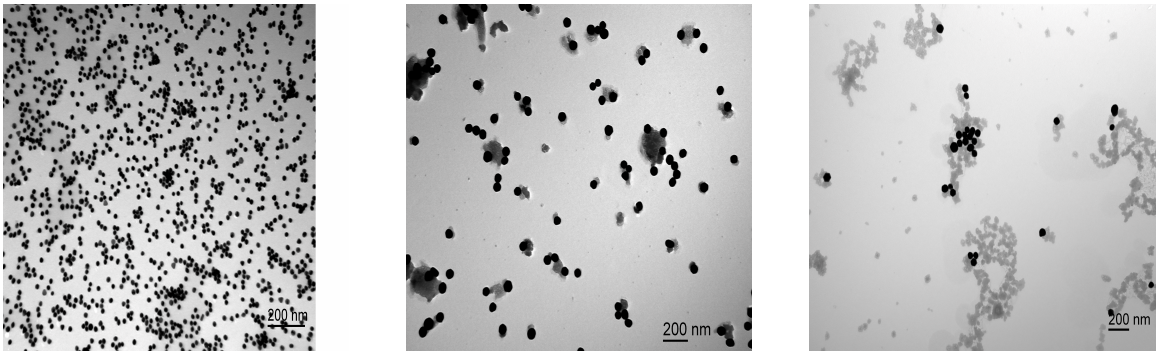

(a) (b) (c)

Figure 5.4: TEM images of gold nanoparticles. (a) 20 nm gold nanoparticles. (b) 60 nm gold nanoparticles. (c) 100 nm gold nanoparticles.

Figure 5.3 shows the CytoViva dark field image of 10 nm gold nanoparticles in

PMMA. There is a ring of gold, condensed together due to the coffee ring effect [195]. Beneath the ring of gold is salt, used in the gold nanoparticle solution to prevent agglomeration. At first, 10 nm gold nanoparticles were used, since the initial calculations and simulations were for 10 nm gold nanoparticles. However, individual 10 nm particles were harder to see in the microscope than larger nanoparticles. Also, the scattering cross section scales with the volume of the particle squared, so the exposure time was much longer for individual 10 nm particles, and measurements would take a long time. Figures 5.4 (a) - (c) show TEM images of the nanoparticles used in this experiment. 20 nm and 60 nm nanoparticles from BBI solutions and 100 nm gold nanoparticles from Cytodiagnostics, all capped with citrate and dispersed in water, were used in the dark field scattering measurements.

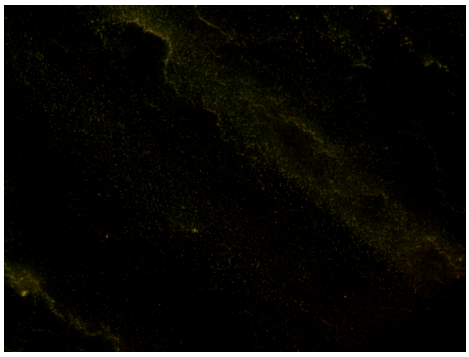

Figure 5.5: 20 nm gold nanoparticles.

Figures 5.5 - 5.7 show the dark field images of different sizes of gold nanoparticles on glass. There was a significant amount of phosphate-buffered saline (PBS) salt in the Cytodiagnostics 100 nm nanoparticle solutions, and so the 100 nm particles were not used in experiments with PMMA and P3HT. Although salt was present in the 20

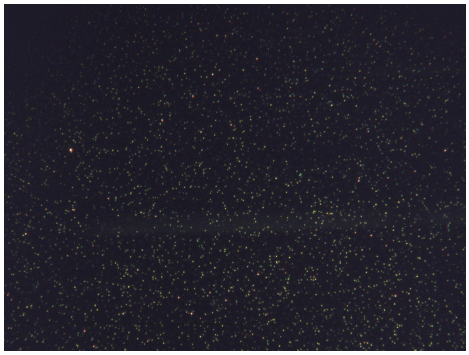

Figure 5.6: 60 nm gold nanoparticles.

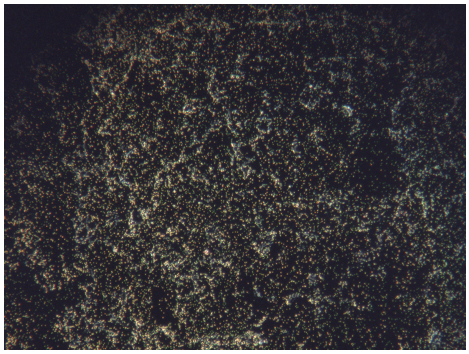

Figure 5.7: 100 nm gold nanoparticles.

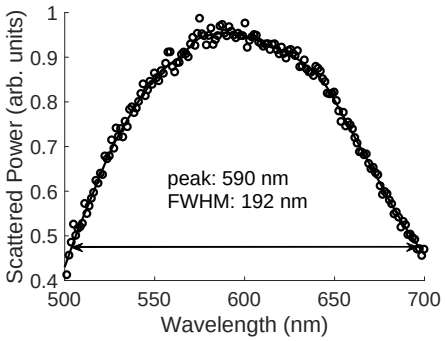

Figure 5.8: Individual 20 nm gold nanoparticle spectrum.

and 60 nm solutions as well, there was not as much, and so there were always at least a few areas on the sample where there individual gold nanoparticles could be measured accurately. Figures 5.8-5.10 show the dark field scattering spectrum of individual 20, 60 and 100 nm gold nanoparticles. For all CytoViva dark field measurements,

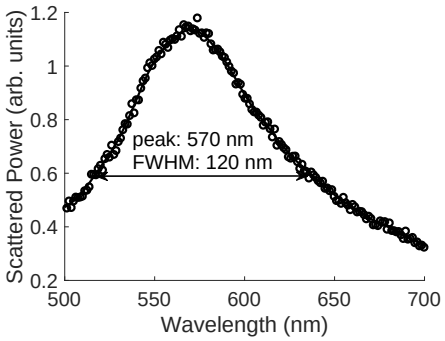

Figure 5.9: Individual 60 nm gold nanoparticle spectrum.

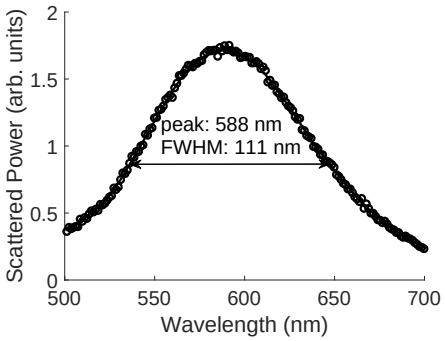

Figure 5.10: Individual 100 nm gold nanoparticle spectrum.

the spectra of a single isolated nanoparticle was measured and normalized to the incident white light source. The linewidth of the 20 nm particles was unusually broad. There are two factors that could explain this broadening. First, there is surface scattering, which becomes a significant linewidth broadening mechanism for small particles. Secondly, the scattered light signal was weak for 20 nm particles, and so did not separate well from the noise. This also made measuring the location of the peak less accurate, which explains why the peak for 20 nm particles are more red-shifted than for larger particles. The 60 nm and 100 nm particles show more expected behaviour, with comparable linewidths and a red-shift in the peak for the

larger particles.

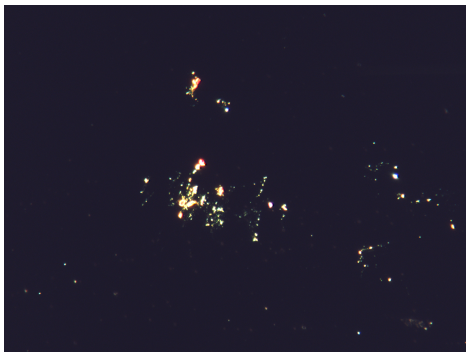

Figure 5.11: 20 nm gold nanoparticles in PMMA.

Figure 5.12: 60 nm gold nanoparticles in PMMA.

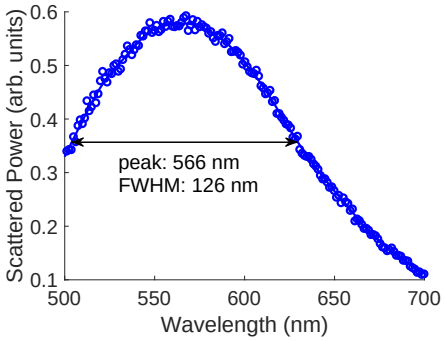

Figure 5.13: Individual 20 nm gold in PMMA spectrum.

Figures 5.11 and 5.12 show the dark field images of 20 and 60 nm gold nanoparticles in a 100 nm thick layer of PMMA. The thickness of PMMA does not affect the

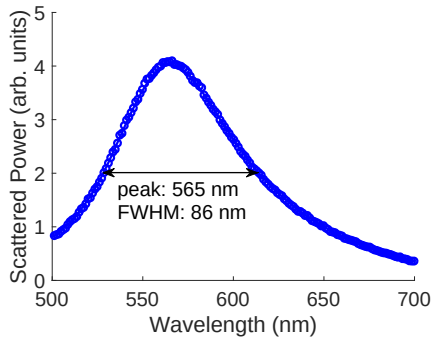

Figure 5.14: Individual 60 nm gold in PMMA spectrum.

scattering spectrum of individual nanoparticles as PMMA is not lossy. There is no attenuation of the scattered light signal as it propagates from the nanoparticles to the camera. Figures 5.13 and 5.14 show the spectrum of the scattered light for isolated 20 and 60 nm nanoparticles in 100 nm thick PMMA. Again, the 20 nm particles show a large broadening of the peak for the same reasons as stated for the case without the PMMA layer. By comparing the data from 20 and 60 nm particles with and without PMMA, the inclusion of PMMA narrows linewidths. This is because increasing the index of refraction of the surrounding environment narrows linewidths for noble metal nanoparticles [87]. A small red-shift was expected by adding PMMA, but this was not observed in experiments.

Figures 5.15 and 5.16 show the dark field images of 20 and 60 nm gold nanoparticles in a 120 nm thick layer of P3HT. The thickness of P3HT did change the scattering spectrum of individual nanoparticles. 120 nm was found to be a good thickness for accurate dark field measurements. When layers were much thinner than this, there were large regions of the sample where the P3HT was sparse and was not a smooth,

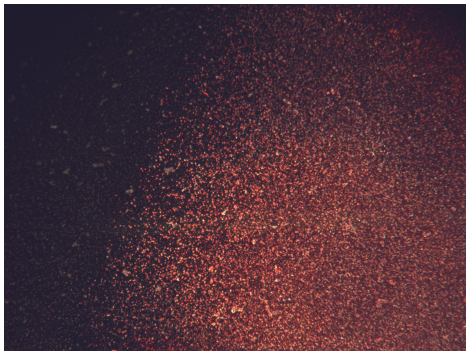

Figure 5.15: 20 nm gold nanoparticles in P3HT.

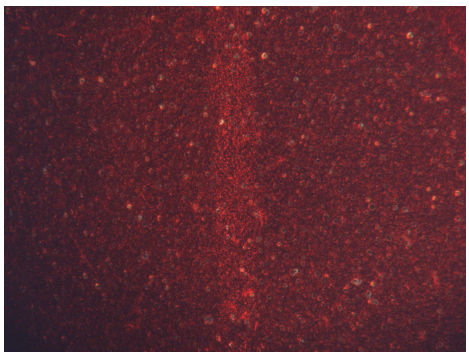

Figure 5.16: 60 nm gold nanoparticles in P3HT.

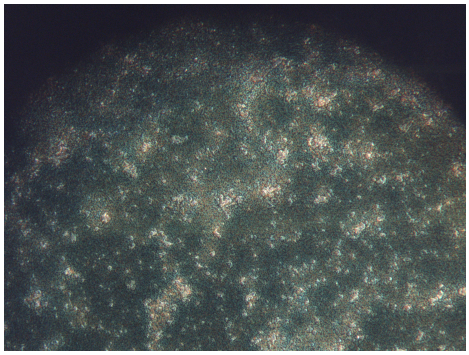

Figure 5.17: A 20 nm layer of P3HT. The layer is no longer uniform. The optical properties are different from those of thicker layers because when the P3HT molecules are this spread, they cannot form a j-aggregate structure.

uniform layer, as seen in Fig. 5.17. If the P3HT layer was much thicker than this, there would be a dominant red fluorescent signal from the P3HT layer which would make it hard to see and measure individual gold nanoparticles, as seen in Fig. 5.18.

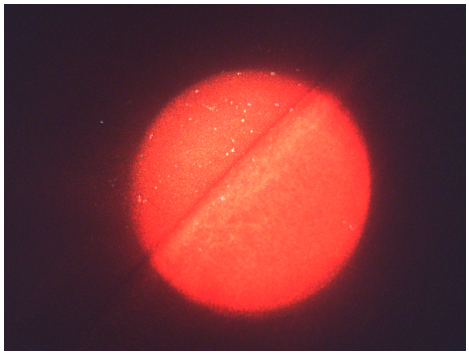

Figure 5.18: A 240 nm layer of P3HT. The fluorescence dominates the scattering signal and gold nanoparticles become difficult to see.

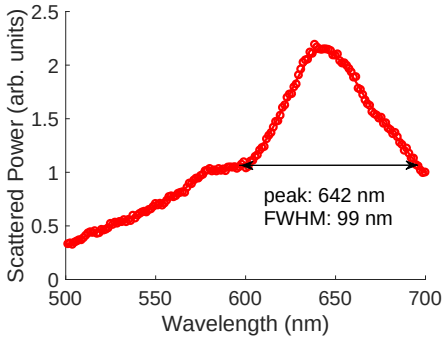

Figure 5.19: Individual 20 nm gold in P3HT spectrum.

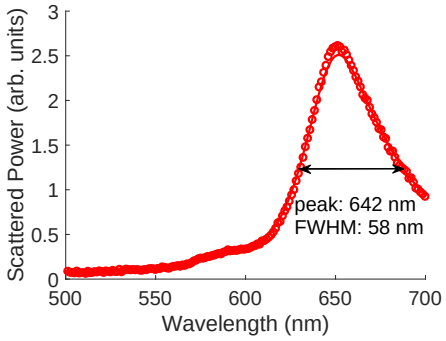

Figure 5.20: Individual 60 nm gold in P3HT spectrum.

Figures 5.19 and 5.20 show the spectra of the scattered light for isolated 20 and 60 nm nanoparticles in 120 nm P3HT. The P3HT significantly red-shifts the peak to around 640 nm, agreeing with the theoretical predictions. Once again, the 20 nm particles

have a wider linewidth. There is a very narrow 58 nm linewidth seen for the 60 nm gold particles in P3HT.

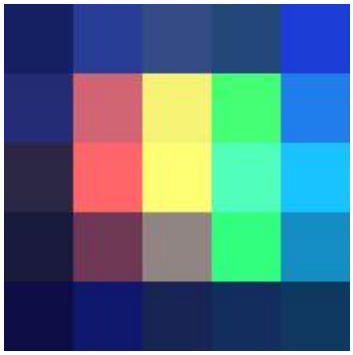

Figure 5.21: Change in spectra across a single isolated 60 nm nanoparticle.

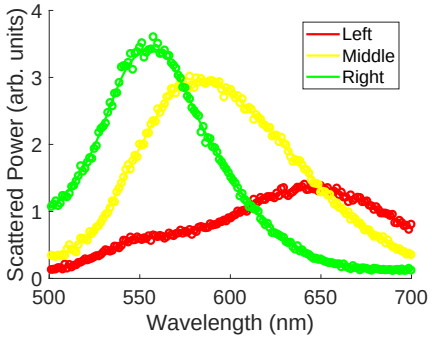

Figure 5.22: Measured scattering spectrum at different points for the above individual 60 nm nanoparticle.

The CytoViva dark field microscope had an issue with measuring spectra, which lead to an artificial broadening of linewidths. Figures 5.21and 5.22 show this problem. For a single nanoparticle, the spectrum measured at each point near the nanoparticle is expected to change in magnitude, but the shape and linewidth should be very similar. However, this was not seen in the CytoViva dark field measurements. CytoViva was contacted about this issue and they mentioned this problem was rare and they had seen this before, but it was not known what caused this problem or how to fix the

issue. Thus, the conclusions drawn from the scattering data should be taken qualitatively rather than quantitatively. However, analyzing the data for 60 nm particles shows that P3HT has a linewidth of 58 nm and PMMA has a linewidth of 86 nm and so P3HT has a linewidth close to two thirds that of PMMA. The theories and simulations predicted that the linewidth for P3HT should be closer to half that for PMMA. The theories and simulations do not take into account the fluorescence of P3HT which absorbs at 550 nm and emits near the plasmon peak around 650 nm and would cause significant linewidth broadening, and this could explain the difference between the CytoViva measurements and the theories and simulations. What can be concluded from the data is that both 20 nm and 60 nm gold nanoparticles in P3HT have a narrower linewidth than in PMMA, agreeing qualitatively with theory.

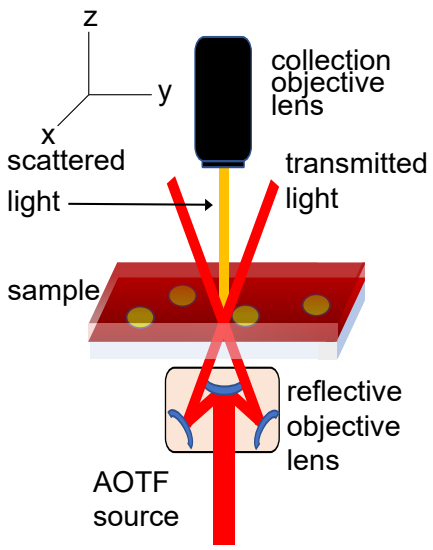

Figure 5.23: Schematic of the AOTF dark field microscope.

Due to the inability of the commercial dark field microscope to accurately measure

linewidth, a separate dark field microscope was constructed. The schematic of the microscope is seen in Fig. 5.23. A supercontinuum laser (Fianium Supercontinuum SC450) emitted a broad range of wavelengths from 350 to 850 nm, while an acousto-optic tuneable filter (Fianium AOTF-DUAL) blocked most of the incident light and acted as a tuneable narrowband filter. The result was a narrow 2-4 nm bandwidth laser beam at any desired wavelength within the range of 450 to 750 nm. The output power would vary greatly from 450-500 nm and 700-750 nm, so the wavelength range of measurements was shortened so that the power did not need to be adjusted between measurements. A sweep of the incident wavelength from 500 to 700 nm was performed in 5 nm intervals to measure the scattering cross section for each sample.

The AOTF dark field setup used a reflective objective lens (Thorlabs LMM-40x-P01, 40× magnification, 0.5 numerical aperture) which emitted light in a cone with an apex angle of 60° to illuminate the sample. The advantage of this lens is there is no dispersion and so no chromatic aberration, as the lens is reflective rather than refractive. This allows for the full range of light from 500-700 nm to follow the same optical path through the lens for better focusing. The scattered light was gathered by a collection objective lens with 7× magnification and 0.2 numerical aperture (NA). The low NA did not transmit the high angle incident light from the source, and only the scattered light from 0° to 12° was transmitted. A Thorlabs Quantalux sCMOS (scientific complementary metal–oxide–semiconductor) camera was used to detect this scattered light. As all light reaching the detector was scattered light, the scattered

power was calculated by integrating the counts over every pixel of the detector for each individual incident wavelength used.

The same samples used for the CytoViva measurements were used in the constructed AOTF dark field microscope. Only 20 nm particles were used because the CytoViva showed that measuring 10 nm particles proved to be difficult due to their low scattering signal. Although 60 nm have a narrower linewidth, a lot of the theory was based around small 10 nm particles. 20 nm particles were used, under the assumption they would produce similar results to 10 nm particles while being easier to measure. The gold nanoparticles had a 600 nm average inter-particle distance upon drop coating onto a glass slide and they were randomly distributed on the surface, except near the edge of the drop, where they would be highly concentrated due to the coffee ring effect [195]. By moving the beam near and away from the edge of the drop, there will be more or less scattering, depending on how many gold particles are in focus. Unlike the CytoViva microscope, the AOTF dark field microscope measured the scattering of many gold nanoparticles in the illuminated area on the sample. This made comparison of the magnitude of the plasmon peaks between different samples, and even different areas of the same sample difficult. The AOTF dark field measurements were performed to find the position of the plasmon peak and the linewidth of the plasmon peak for different samples.

Figure 5.24 (a) shows the scattered power of 20 nm gold nanoparticles in PMMA and Fig. 5.24 (b) shows the scattered power of 20 nm gold nanoparticles in P3HT

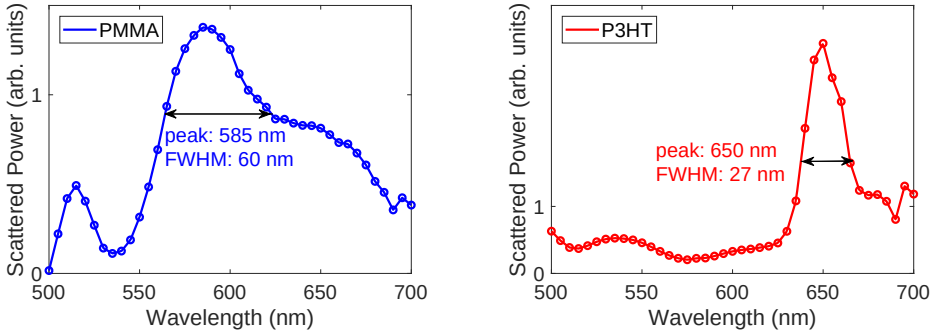

(a) (b)

Figure 5.24: Scattering data collected from the AOTF dark field microscope. The circles on the plots correspond to measured scattering data and occur in 5 nm steps. The position of the plasmon peak and the FWHM are displayed on each plot. (a) Scattered power of 20 nm gold nanoparticles in PMMA. (b) Scattered power of 20 nm gold nanoparticles in P3HT.

obtained with the AOTF dark field microscope. The effect of fluorescence of P3HT was greatly reduced in the AOTF setup by looking at areas with a higher concentration of gold nanoparticles, which would increase the ratio of plasmon peak signal to background fluorescence. Additionally, with the narrow 2-4 nm bandwidth of the source, there was much less excitation of fluorescence, compared to the 400-1000 nm incident white light of the CytoViva. The absorption peak occurs for P3HT around 550 nm so it is likely that the small peak seen in Fig. 5.24 (b) at 550 nm is from the increased fluorescence signal from this absorption peak. A narrow 27 nm (80 meV) plasmon linewidth was measured in dark field scattering experiments using 20 nm gold nanoparticles in lossy and dispersive P3HT. This linewidth was less than half the measured linewidth of 60 nm (220 meV) for gold nanoparticles in non-lossy, non-dispersive PMMA. This agrees qualitatively with the theoretical predictions. The

experimental linewidth was surprisingly narrower than both the FDTD simulations and the Green theory. In the Green theory, the source used to excite the gold nanoparticle was a dipole and not a plane wave. A nearby dipole might couple to the dipole mode of the gold nanoparticle more than an incident plane wave. The dipolar mode is the broadest mode, and so this difference in the coupling of modes between the dipole and plane wave sources could explain why the Green theory results have a broader linewidth than experiments. As for the simulations, one possible explanation for this difference in linewidths is the difference in the area over which the scattered light was measured. In simulations, the monitor used to measure the scattered power collected the light over a large solid angle. In the experiments, the collective objective is relatively far from the source and had a small aperture resulting in scattered light collected over a smaller solid angle. It is typical for scattering spectrum to vary with the scattering angle and so collecting over a larger area would expectedly result in a broadened spectrum. Thus, the dark field scattering experimental results verify the narrow linewidth theorized previously [191]. In contrast to past works claiming that losses must be reduced in plasmonic systems when small linewidths are desired [10, 158, 159, 107, 106, 160], by embedding gold nanoparticles in the lossy and dispersive P3HT, the linewidth was surprisingly reduced. With the theory verified by the experiment, it is concluded that the narrow plasmon peak exhibited by gold nanoparticles in P3HT is attributed to the large dispersion in both the real and imaginary parts of the permittivity for P3HT as well as the large magnitude of the

real part and relatively low loss at the plasmon peak.

5.3 Conclusion

Dark field experiments using both a CytoViva commercial dark field microscope setup and a constructed AOTF tuneable laser dark field setup were conducted to measure the scattering signal of 20 nm gold nanoparticles in PMMA and P3HT. Much broader linewidths were measured in the CytoViva microscope due to an unresolved technical issue, however it was found that in general the linewidths measured for P3HT samples was narrower than those for PMMA samples. Also, fluorescence played a significant role in broadening linewidths for P3HT samples in this setup. The AOTF setup minimized fluorescence by exciting with a narrowband source and a remarkably narrow 27 nm linewidth was measured for gold in P3HT samples. Again, this was much narrower than the 60 nm linewidth measured for gold in PMMA. Thus the experiments verified the predictions of the theory and the simulations.

Chapter 6

Conclusions

6.1 Conclusions

Method	PMMA Linewidth	P3HT Linewidth
Rayleigh theory	50 nm	35 nm
Mie theory (extinction)	50 nm	43 nm
Green theory	58 nm	35 nm
FDTD simulations	58 nm	42 nm
AOTF dark field	60 nm	27 nm

Table 6.1: Linewidths calculated for 20 nm gold nanoparticles in PMMA and P3HT for each different method used in this thesis.

The main result of this thesis is that lossy media can narrow linewidths. This conclusion was reached with Rayleigh theory, Mie theory, Green theory, FDTD simulations, and dark field scattering experiments, and has recently been verified independently using a Mie theory approach [169]. Table 6.1 summarizes the results of each of the different methods stated above. The linewidth of P3HT is consistently much

smaller than that of PMMA, and this surprising result was found to be attributed to the large dispersion of P3HT. The effect dispersion had on narrowing the linewidth was clarified with a Green theory analysis, and it was found a strong wavelength dependence for the real and imaginary parts of the permittivity each can narrow the linewidth significantly.

The initial motivation for researching the optical properties of gold nanoparticles in P3HT was to create plasmonic enhanced P3HT OPVs. In this case the narrow absorption cross section of gold in P3HT was detrimental and much of the solar spectrum is not absorbed in these cells. However, another project relating to the advancement of solar cells was undertaken and a theory was developed to explain past experimental results [1]. It was hypothesized that the dark field enhancement seen from gold nanorods near erbium emitters was due to a saturation of 980 nm emission, which results in a population inversion more favourable to emitting 650 nm light [1]. In FDTD simulations where the erbium atom is modelled by a dipole, this behaviour is not seen, and there is minimal far-field enhancement of the dark mode compared to the bright mode. More work needs to be done with this theory in order to prove its validity.

6.2 Comparisons

Compared to the plethora of works relating to plasmonic in non-lossy media, there has not been much effort in understanding the roles of loss and dispersion in relation to the plasmon linewidth, and usually these phenomena are considered separately if at all. This is likely because of the popular belief that loss should be avoided in plasmonics [106, 107] and so it would be unexpected to improve a plasmonic device by adding loss to the system by means of encapsulation by a strongly absorbing material. There have been many works concerned with finding the correct formulas to describe scattering of particles in lossy media [133, 134, 136, 138, 139, 160], but none considered how plasmon resonances were affected. During my PhD at the University of Victoria, under the guidance of my supervisors Professor Reuven Gordon and Professor Alex Brolo, I have published two works based on plasmonics in dispersive lossy media. The first work was a theoretical work which discovered that a plasmon resonance peak could be narrowed in a lossy dispersive medium [191], and the second work involved experiments and further theoretical developments to both verify and understand the results of the first work [166]. Professor Stephen Hughes and Dr. Juanjuan Ren developed the theory and provided working code to calculate the scattering cross section of metal nanoparticles in lossy dispersive media [166]. It seems these works sparked some interest in the nanophotonics community as there have already been two works after our publications which analyzed plasmonic resonances in lossy media.

It has been shown that adding a strongly absorbing medium broadens linewidths, but these works analyzed only materials with constant loss and ignored dispersion [133, 138, 160]. The presence of dispersion can drastically change a plasmon resonance, and was shown to be the reason for the linewidth narrowing for 20 nm gold nanoparticles in P3HT. Lossy materials have been avoided in plasmonics, and here it has been shown that they can achieve desirable qualities for nanoplasmonic devices. This opens up a world of possible materials to use in plasmonic devices that would likely have remained ignored before, potentially leading to new and improved plasmonic devices.

Candidates other than P3HT for plasmonic dispersive lossy materials were analyzed with Green theory calculations with the hopes of finding even narrower plasmon peaks. Five perovskites which had different permittivities over the range of wavelengths from 500-700 nm were investigated. The linewidths calculated for each of these were about double that of P3HT. Although these materials were dispersive, it was found that the dispersion has to be near the plasmon peak to be most effective in narrowing the linewidth. This complicates finding a lossy dispersive material which generates a narrow linewidth; having a lossy dispersive material does not ensure a narrow linewidth. With the understanding of how dispersion can narrow linewidths discussed in this thesis, it seems possible to predict which materials may yield narrow linewidths in plasmonic systems. If we are interested in gold for its stability and large negative permittivity, then we would want to look at plasmonic peaks outside of the

interband transitions of gold. Then we would want the plasmon resonance peak to be roughly between 500 and 800 nm for optical devices. As the negative permittivity of gold goes from -2 to -27 in this range, this means that the real permittivity of the surrounding medium in question must be between 1 and 13.5 to satisfy the Fröhlich condition in this wavelength region, which means most media will produce a plasmon peak in this region. If the material has a dispersive real permittivity that would be ideal to narrow the linewidth even further. Assuming this material is lossy, it is necessary to have dispersion in the loss, or else it would produce a broad peak. Then wherever the plasmon peak occurs, that is where the dispersion in the imaginary permittivity should be most significant. For example, if there was a semiconducting material that, when surrounding gold nanoparticles resulted in a plasmon peak at 700 nm, a sharp band edge at 700 nm would be ideal for minimizing the linewidth. The sharper the band edge the narrower the plasmon peak should be. As constant loss does broaden linewidths, the material would ideally become transparent nearby the plasmon peak, and a sharp band edge material would have this property as well. Although they may be difficult to find, it seems likely other combinations of metals and lossy, dispersive media which will generate narrower linewidths than those seen for P3HT.

The results of theory and experiment in this thesis on linewidths in nanoplasmonics sparked some interest in the community. Mishchenko and Dlugach explicitly showed with theoretical calculations that constant loss in the surrounding medium

greatly broadened linewidths which agreed with our findings on constant loss [160]. However they did not look at the case of dispersive lossy media, where, as was shown here, the linewidth can be significantly narrower than for a non-lossy medium. Khlebtsov created a theory for scattering in lossy media which predicted linewidths for gold in P3HT and PMMA that agreed well with our results [169]. He calculated a linewidth of 33.6 nm for the extinction cross section of 10 nm gold in P3HT and 53.8 nm for PMMA [169]. Furthermore he showed that the scattering cross section scales differently for lossy and non-lossy media. For a lossy medium the scattering cross section scales with the inverse of the size parameter ($x = kan$, where k is the real part of the complex wave number in the absorbing medium, a is the radius of the nanoparticle and n is the complex index of refraction in the absorbing medium) while for non-lossy media it scales with the inverse of the fourth power of the size parameter. He also showed, using his theory, that the scattering cross section can be larger in magnitude for lossy media than for non-lossy media, which is a surprising result. Khlebtsov found that for small particles (below 50 nm) increasing the loss of the surrounding medium increased the magnitude of the scattering peak in the near field. He also discovered that surprisingly, the results of Rayleigh theory did not differ much from his improved electrostatic approximation. Even though Rayleigh theory should not apply in the case of lossy surrounding media, he showed that even for a material as strongly absorbing as P3HT the predictions of Rayleigh theory were accurate for nanoparticles as large as 50 nm. Another recent work of Khlebtsov studied non-

spherical nanoparticles in P3HT to show a further reduction in the linewidth [196]. He investigated gold and silver nanorods and nanodisks in a variety of lossy media. The reduction in linewidth observed between spherical and non-spherical particles in lossy media is expected since it is known that spheres have broader linewidths than any other shape of nanoparticle for non-lossy media. Khlebtsov calculated exceptionally narrow linewidths in the range of 14-20 nm for these non-spherical nanoparticles in lossy media.

The nanophotonics community is still making progress in understanding scattering in lossy non-dispersive media. Recently, Zhai et al. and Dong et al. have published papers that analyzed the scattering and extinction cross sections in lossy non-dispersive media. [197, 198]. They compared the scattering and extinction cross sections of standard Mie theory and a Mie theory modified for use in lossy media [199, 200]. The difference between the cross sections for Mie theory and the modified Mie theory for lossy media was very small; only about 1%. Their results showed that neglecting loss affects the scattering cross section more than the extinction cross section. Dong et al. applied the discrete dipole approximation (DDA) to plasmonics in lossy media and compared the results to a Mie theory adapted for lossy media [198]. In this work, they used non-lossy particles to focus on how the loss of the medium affected the cross sections, although their DDA theory can be applied for the case of a lossy particle as well. The DDA agreed with the modified Mie theory very well for small particle sizes, but this agreement gradually became worse for larger particle sizes. Regardless, the

DDA method they developed will certainly serve as a useful tool to analyze plasmonic lossy media.

6.3 Future Work

Lossy and dispersive plasmonic media have some potential applications in nanotechnology. One idea is to combine loss and gain media to make a nanolaser; a dispersive lossy material with embedded metal nanoparticles could be used to generate a narrow scattering response, while a surrounding gain media could increase the power scattered at the peak wavelength. Dispersive lossy materials may also see applications in SPR sensing where a narrow linewidth is desirable, and allows for greater multiplexing within a given bandwidth [201, 202, 203]. Another idea is to use nano-engineered materials that can have their permittivities adjusted, such as photonic bandgaps or liquid crystals. The permittivities of photonic bandgaps can be greatly altered by changing the dimensions of the devices. They also have large dispersion, which is important for narrow linewidths. The permittivities of liquid crystals can be changed in real time by applying a voltage. In particular, it would be interesting to see how the linewidth changes for gold nanoparticles surrounded in the liquid crystals, as the applied voltage is varied.

Lossy plasmonic media could have applications in biosensing. Recently Popescu and Sharma developed a new plasmonic biosensor to measure hemoglobin concen-

trations in humans [204]. As the authors mention, this is important for diagnosing anemia which can be an indicator of leukemia and other diseases. Popescu and Sharma used a plasmonic sensor which included an alumina layer which is a lossy medium. The inclusion of the layer served to increase light absorption by the nearby analyte layer and also narrow the plasmon peak. They achieved a lower detection limit than a gold and aluminum plasmon sensor which made use of a thin gold layer to stabilize the aluminum and so did not have a lossy alumina layer [205].

Lossy plasmonic media could have applications in solar cells for making narrow-band active layers for use in tandem cells. This idea seems counter-intuitive at first, since for most solar cells a broadband absorber which could absorb most of the incident solar spectrum would be desirable. However, when the linewidth narrows it can be accompanied by an increase in the quality factor. This can be seen from Khlebtsov's work where the near field enhancement in P3HT is larger than in the non-lossy PMMA. With increased near field enhancement there could be much more absorption in solar cells nearby the plasmonic metal nanoparticles. Using an optimized geometry and material for the plasmonic nanoparticles could allow for tailoring the plasmon resonance to a desirable spectral location, resulting in an overall increase in absorption, even though the spectral region of the absorption is reduced. This type of solar cell could be very useful in making a high efficiency tandem solar cell; a solar cell composed of many layers of individual solar cells stacked together, each absorbing a different part of the spectrum.

Khlebtsov has developed an electrostatic approximation, improved electrostatic approximation and a transfer matrix method all of which describe absorption, scattering and extinction of nanoparticles in lossy media. His improved electrostatic and transfer matrix method models agree well with each other and agree with his electrostatic approximation for small particles. The next logical step would be to take more measurements of different shaped nanoparticles in lossy media to see how well these theories agree with experimental measurements. His electrostatic and improved electrostatic theories do match well with our experimental results for gold nanoparticles in P3HT and PMMA, but more measurements can be made to verify the validity of his theories. There should be experimental measurements for silver nanoparticles as well, and spheroidal nanoparticles to verify his theory works different shapes, sizes and constituent metal nanoparticles. The most difficult part of making a theory which describes scattering in lossy media is making sure calculated cross sections have the correct dependence on the distance from the nanoparticle, as this dependence becomes complex when both the scattered light and incident light are progressively absorbed as they travel through the medium. To test the correct dependence exists in the theory, there could be dark field measurements for lossy materials with different film thicknesses. A quick test of Khlebtsov's theories would be to compare the measured extinction spectra of silver nanorods in P3HT. For silver nanorods with a length of 15 nm and a diameter of 10 nm embedded in P3HT, Khlebtsov's improved electrostatic approximation predicts a small broad peak at 650 nm, while for silver

nanorods with a length of 30 nm and a diameter of 10 nm there is a large narrow peak at 800 nm [196]. Khlebtsov's theories also predicted some very narrow resonances for non-spherical gold and silver nanoparticles in P3HT. It would be interesting to verify if the peaks are truly so narrow in reality. In particular, the oblate silver nanoparticle with a 40 nm diameter and 10 nm length in P3HT is predicted to have an extremely narrow 14 nm linewidth.

Appendix A

Additional Information

A large portion of the following text has been adapted from [166].

A.1 Linewidth Dependence on Metal Properties

Here is the derivation of equation 2.4 which relates the linewidth of a LSPR to the dispersion and absorption characteristics of the metal nanoparticle. For this derivation, it is assumed that the surrounding medium is non-lossy and non-dispersive. We start with the Rayleigh equation for the absorption coefficient of a small sphere in a homogeneous surrounding medium. The absorption coefficient is given by

$$K(\omega) = \frac{9\pi n_0^2 C_v \omega}{c} \frac{\epsilon_2}{(\epsilon_1 + 2n_0^2)^2 + \epsilon_2^2}, \tag{A.1}$$

where n_0 is the index of refraction of the surrounding medium, C_v is the density of nanoparticles within the medium, ω is the incident angular frequency of light, c is the speed of light, and ϵ_1 and ϵ_2 are the real and imaginary parts of the permittivity of the spherical nanoparticle respectively. The peak occurs when the plasmon resonance condition is met: $\epsilon_1 = -2n_0^2$ and the absorption coefficient at the peak frequency is

$$K_{max}(\omega^*) = \frac{9\pi n_0^2 C_v \omega^*}{c} \frac{1}{\epsilon_2^*}, \tag{A.2}$$

where a $*$ superscript indicates that the quantity is evaluated at the peak frequency, and ω^* is the peak frequency. The linewidth of the extinction peak can be calculated using these formulas. At the half-max, which is defined to be a frequency shift $d\omega$ from the peak,

$$K(\omega^* + d\omega) = \frac{9\pi n_0^2 C_v(\omega^* + d\omega)}{c} \frac{\epsilon_2}{(\epsilon_1 + 2n_0^2)^2 + \epsilon_2^2} = \frac{1}{2} K_{max} = \frac{9\pi n_0^2 C_v \omega^*}{2c} \frac{1}{\epsilon_2^*} \tag{A.3}$$

Expand ϵ_1 and ϵ_2 in first-order Taylor expansions centered at the peak

$$\epsilon_1(\omega) \approx \epsilon_1^* + \dot{\epsilon_1} \delta\omega \tag{A.4}$$

$$\epsilon_2(\omega) \approx \epsilon_2^* + \dot{\epsilon_2} \delta\omega. \tag{A.5}$$

In the above formulae $\delta\omega$ is the difference from the peak frequency and a $\dot{x}$ represents a derivation with respect to ω followed by an evaluation at ω^*. Using these Taylor expansions yields

$$\frac{9\pi n_0^2 C_v(\omega^* + d\omega)}{c} \frac{\epsilon_2^* + \dot{\epsilon_2} d\omega}{((\epsilon_1^* + \dot{\epsilon_1} d\omega + 2n_0^2)^2 + (\epsilon_2^* + \dot{\epsilon_2} d\omega)^2} = \frac{9\pi n_0^2 C_v \omega^*}{2c} \frac{1}{\epsilon_2^*}. \tag{A.6}$$

Using $\epsilon_1^* = -2n_0^2$ this simplifies to

$$(\omega^* + d\omega) \frac{\epsilon_2^* + \dot{\epsilon_2} d\omega}{(\dot{\epsilon_1} d\omega)^2 + (\epsilon_2^* + \dot{\epsilon_2} d\omega)^2} = \frac{\omega^*}{2\epsilon_2^*}. \tag{A.7}$$

Gathering similar powers of $d\omega$ results in a quadratic equation

$$\left[\dot{\epsilon_2} - \frac{\omega^*}{2\epsilon_2^*}(\dot{\epsilon_1}^2 + \dot{\epsilon_2}^2)\right] d\omega^2 + \left[\epsilon_2^*\right] d\omega + \left[\frac{\omega^* \epsilon_2^*}{2}\right] = 0. \tag{A.8}$$

This equation is difficult to solve directly, but the more simple equation,

$$\left[-\frac{\omega^*}{2\epsilon_2^*}(\dot{\epsilon_1}^2 + \dot{\epsilon_2}^2)\right] d\omega^2 + \left[\frac{\omega^* \epsilon_2^*}{2}\right] = 0 \tag{A.9}$$

can be solved easily. The solution is

$$d\omega = \frac{\epsilon_2^*}{\sqrt{\dot{\epsilon_1}^2 + \dot{\epsilon_2}^2}} \tag{A.10}$$

The linewidth is given by $\Gamma = 2d\omega$ so

$$\Gamma = \frac{2\epsilon_2^*}{\sqrt{\dot{\epsilon_1}^2 + \dot{\epsilon_2}^2}}. \tag{A.11}$$

Of course, this will differ from the actual solution. We can go back and slightly modify the solution for the simplified problem in order to solve the full problem. Let

$$d\omega = \frac{2\epsilon_2^*}{\sqrt{\dot{\epsilon_1}^2 + \dot{\epsilon_2}^2}}(1+\eta) \tag{A.12}$$

Then the equation becomes

$$\left[\frac{\epsilon_2^{*2}\dot{\epsilon_2}}{\dot{\epsilon_1}^2 + \dot{\epsilon_2}^2} - \frac{\omega^*\epsilon_2^*}{2}\right]\eta^2 + \left[\frac{\epsilon_2^{*2}}{\sqrt{\dot{\epsilon_1}^2 + \dot{\epsilon_2}^2}} + \frac{2\epsilon_2^{*2}\dot{\epsilon_2}}{\dot{\epsilon_1}^2 + \dot{\epsilon_2}^2} - \omega^*\epsilon_2^*\right]\eta + \left[\frac{\epsilon_2^{*2}}{\sqrt{\dot{\epsilon_1}^2 + \dot{\epsilon_2}^2}} + \frac{\epsilon_2^{*2}\dot{\epsilon_2}}{\dot{\epsilon_1}^2 + \dot{\epsilon_2}^2}\right] = 0 \tag{A.13}$$

which is a quadratic equation in η. Using the permittivity values for silver, Kreibig found that $\eta < 2 \times 10^{-3}$ [80]. Thus it can be assumed that η is negligible and the formula relating the linewidth of a small metal particle to its permittivities is

$$\Gamma = \frac{2\epsilon_2^*}{\sqrt{\dot{\epsilon_1}^2 + \dot{\epsilon_2}^2}}. \tag{A.14}$$

A.2 Electron-Phonon Relaxation Rate

The electron-phonon relaxation rate is derived here, following the derivation shown in McKay and Rayne [85].

$$P_{\pm}^{\pm}(\vec{k} \rightarrow \vec{k'}) = [\frac{e^2(\vec{E} \cdot \vec{q})^2}{4Vm^2\omega^4}]A^{\pm}(\vec{q}) \times [1 - f(E_{\vec{k'}})]\delta(E_{\vec{k}} - E_{\vec{k'}} \pm \hbar\omega_{\vec{q}} \pm \hbar\omega). \quad \text{(A.15)}$$

This is the probability per unit time of a simultaneous phonon and photon absorption/emission process occurring for a free-electron initially in state $\vec{k}$ and ending in state $\vec{k'}$ after the interaction with a phonon of wave vector $\vec{q}$. The top $\pm$ corresponds to phonon emission $(+)$ and absorption $(-)$ while the corresponds to photon emission and absorption. e is the electron charge, $\vec{E}$ is the external electric field, V is the sample volume, m is the effective mass of an electron, ω is the angular frequency of the photon and ω_q is the angular frequency of the phonon, f is the Fermi distribution function, and $E_{\vec{k}}$ is the energy of a free electron with wave vector $\vec{k}$ and lastly $\delta(x)$ is the Dirac delta function. $A^{\pm}(\vec{q})$ is defined to be:

$$A^{\pm}(\vec{q}) = \frac{Dq^2}{\omega_{\vec{q}}}\begin{pmatrix} n_{\vec{q}} + 1 \\ n_{\vec{q}} \end{pmatrix} \quad \text{(A.16)}$$

where $D = \frac{\pi C^2}{NM}$, C is the coupling constant, N is the atomic density and M is the mass of the ion. To clarify the bracketed term, when a phonon is emitted a factor of $n_{vecq} + 1$ is used and when a phonon is absorbed a factor of n_{vecq} is used.

From the requirement of conservation of momentum, the phonon wave vector must be the difference between the electron wave vector before and after the interaction with the phonon: $\vec{q} = \pm(\vec{k} - \vec{k'})$. The average interaction probability can be found by averaging $P_{\pm}^{\pm}(\vec{k})$ over all possible incident field directions θ, defined as the angle between the field and the direction of the phonon wave vector (the field magnitude simply scales the probability so there is no need to average over the field magnitude), and over all possible phonon wave vectors.

$$P_{\pm}^{\pm}(\vec{k}) = \frac{e^2E^2}{48\pi^2m^2\omega^4}\int_0^{q_0}\int_0^{\pi} q^2A^{\pm}(q)\delta(\frac{\hbar^2q^2}{2m}+\frac{\hbar^2}{m}kq\cos\theta\pm\hbar\omega_{\vec{q}}\pm\hbar\omega)[1-f(E_{\vec{k}+\vec{q}})]q^2dqd\theta \tag{A.17}$$

where $q_0 = (6\pi^2N)^{1/3}$ is the largest wave vector a phonon can have in the Debye model. After integration over θ the average interaction probability for an electron with wave vector $\vec{k}$ simplifies to

$$P_{\pm}^{\pm}(\vec{k}) = \frac{e^2E^2}{48\pi^2m\omega^4\hbar^2k}\int_0^{q_0} q^3A^{\pm}(q)[1 - f(E_{\vec{k}} \mp \hbar\omega_q \mp \hbar\omega)]dq. \tag{A.18}$$

This quantity can further be averaged over all available free electron states to get the average interaction probability per second of all the electrons. The resulting quantity is then the probability per second that an electron in state k is scattered in an electron-phonon reaction, which is by definition the electron-phonon scattering

rate (or equivalently, the inverse of the electron-phonon relaxation time)

$$\frac{1}{\tau_{\pm}^{\pm}} = \frac{\sum_{\vec{k}} P_{\pm}^{\pm}(\vec{k}) f(E_{\vec{k}})}{\sum f(E_{\vec{k}})} \approx \frac{3}{2\zeta} \int P_{\pm}^{\pm}(\vec{k}) f(E_{\vec{k}}) dE_{\vec{k}}. \tag{A.19}$$

Here ζ is the Fermi energy. This is really four different relaxation rates corresponding to the four different possible processes involving simultaneous phonon and photon absorption and emission. Now substitute Eqn. (A.18) into the above equation to get

$$\frac{1}{\tau_{\pm}^{\pm}} = \frac{e^2 E^2}{48\pi^2 m\omega^4 \hbar k_0} \int_0^{q_0} q^3 A^{\pm}(q) G_{\pm}^{\pm}(q) dq \tag{A.20}$$

where k_0 is the Fermi wave number and $G_{\pm}^{\pm}(q)$ is defined to be the following integral

$$G_{\pm}^{\pm}(q) = \frac{3}{2\zeta} \int_0^{\infty} \frac{1}{1 + e^{(E-\zeta)/k_B T}} \frac{e^{(E-\zeta \mp \hbar\omega_q \mp \hbar\omega)/k_B T}}{1 + e^{(E-\zeta \mp \hbar\omega_q)/k_B T}} dE \tag{A.21}$$

This integral can be solved and the result is

$$G_{\pm}^{\pm}(q) = \frac{3}{2\zeta} \frac{\pm\hbar\omega_q \pm \hbar\omega}{e^{(\pm\hbar\omega_q \pm \hbar\omega)/k_B T} - 1}. \tag{A.22}$$

Now there are multiple cases to consider in order to simplify Eq. (A.2). For each of these cases we need to know the power used by the electromagnetic field, which is the difference in the average total number of photons absorbed and created per second

by each scattering process multiplied by the energy per photon.

$$W = \sum_{\pm} \left(\frac{1}{\tau_{-}^{\pm}} - \frac{1}{\tau_{+}^{\pm}} \right) \hbar\omega \tag{A.23}$$

where the sum is over the two possible phonon scattering outcomes; the creation and absorption of a phonon. First when $\hbar\omega << k_B\Theta, k_BT$ which is the classical case,

$$W = \sum_{\pm} \lim_{\hbar\omega\to 0} \left(\frac{1}{\tau_{-}^{\pm}} - \frac{1}{\tau_{+}^{\pm}} \right) \hbar\omega = \sum_{\pm} \frac{e^2E^2}{24\pi^2 m\omega^4 k_0} \int_0^{q_0} q^3 A^{\pm}(q) \frac{\partial G_{-}^{+}}{\partial(\hbar\omega)} dq. \tag{A.24}$$

Using $\omega_q = c_l q$ and c_l is the longitudinal velocity of sound, this equation can be rewritten

$$W = \frac{e^2E^2}{16\pi^2 m\omega^2 k_0} \int_0^{q_0} \frac{\hbar q^5 D}{k_BT} \frac{e^{\hbar c_l q/k_BT}}{(e^{\hbar c_l q/k_B t} - 1)^2} dq. \tag{A.25}$$

Including the Debye temperature $\Theta = \frac{\hbar\omega_q}{k_B} = \frac{\hbar c_l q}{k_B}$ then

$$W = \frac{e^2E^2(k_BT)^5 D}{16\pi^2 m\omega^2 k_0 \zeta \hbar^5 c_l^6} I_5(\Theta/T) \tag{A.26}$$

where $I_5(x)$ is defined as

$$I_5(x) = \int_0^x \frac{z^5 dz}{(e^z - 1)(1 - e^{-z})}. \tag{A.27}$$

Further simplification of the variables leads to

$$W = \frac{9\pi^3 e^2 E^2 \hbar^2 N C^2}{4m\omega^2 (2m)^{1/2} k_B \Theta M} \left(\frac{T}{\Theta}\right)^5 I_5(\Theta/T). \tag{A.28}$$

The relaxation time at high temperatures, tau_{dc} is known to be

$$\frac{1}{\tau_{dc}} = \frac{9\pi^3}{2} \frac{\hbar^2 C^2 N}{(2m)^{1/2} \zeta^{3/2} M k_B \Theta} \left(\frac{T}{\Theta}\right)^5 I_5(\Theta/T) \tag{A.29}$$

Then the relationship between the power taken from the electromagnetic field and the relaxation time is

$$W = \frac{e^2 E^2}{2m\omega^2} \frac{1}{\tau_{dc}}. \tag{A.30}$$

The second simplifying case is when $\hbar\omega >> k_B\Theta, k_B T$ and this is the case most pertinent to nanophotonics, since we are typically looking at high frequencies in the optical regime and at room temperature. With this approximation, G becomes

$$G_-^{\pm}(q) \approx \frac{3\hbar\omega}{2\zeta} \tag{A.31}$$

$$G_+^{\pm}(q) \approx \frac{3\hbar\omega}{2\zeta} e^{-\hbar\omega/k_B T} << G_-^{\pm}(q) \tag{A.32}$$

so then

$$\frac{1}{\tau_-^{\pm}} << \frac{1}{\tau_+^{\pm}} \tag{A.33}$$

and so photon absorption is the dominant process at higher frequencies, which is intuitive. Now the power used by the field becomes

$$W = \frac{e^2E^2\pi C^2}{32\pi^2 m\omega^2\zeta k_0 NMc_l}(\frac{q_0^5}{5}+int_0^{q_0}\frac{2q^4dq}{e^{\hbar c_l q/k_BT}-1} = \frac{e^2E^2}{m\omega^2}\frac{9\pi^3\hbar NC^2}{8\zeta k_0 M}\left(\frac{1}{5}+\int_0\frac{2x^4dx}{e^{x\Theta/T}-1}\right). \tag{A.34}$$

Upon further simplification we get

$$W = \hbar\omega\sum_{\pm}\frac{1}{\tau_-^{\pm}}\frac{e^2E^2}{32\pi^2 m\omega^2\zeta k_0}\sum_{\pm}\int_0^{q_0} q^3A^{\pm}(q)dq. \tag{A.35}$$

Here we introduce a relaxation time

$$\frac{1}{\tau_0} = \frac{9\pi^3}{8}\frac{\hbar^2C^2N}{(2m)^{1/2}\zeta^{3/2}Mk_0\Theta} \tag{A.36}$$

Recall that the relaxation time at high temperatures, tau_{dc} is defined to be

$$\frac{1}{\tau_{dc}} = \frac{9\pi^3}{2}\frac{\hbar^2C^2N}{(2m)^{1/2}\zeta^{3/2}Mk_B\Theta}\left(\frac{T}{\Theta}\right)^5 I_5(\Theta/T) \tag{A.37}$$

so then

$$\frac{1}{\tau_{dc}} = \frac{T}{\Theta}\frac{1}{\tau_0}. \tag{A.38}$$

Now define $z = x\Theta/T$ to get

$$W = \frac{e^2E^2}{2m\omega^2}\frac{1}{\tau_0}\left[\frac{2}{5} + 4\left(\frac{T}{\Theta}\right)^5 \int_0^{\Theta/T} \frac{z^4 dz}{e^z - 1}\right]. \tag{A.39}$$

By comparing to the high temperature/low photon energy scenario, where the energy expended by the field and the relaxation time are related by Eq. (A.2), then Eq. (A.2) for low temperature/high photon energy corresponds to the electron-phonon relaxation time

$$\frac{1}{\tau} = \frac{1}{\tau_0}\left[\frac{2}{5} + 4\left(\frac{T}{\Theta}\right)^5 \int_0^{\Theta/T} \frac{z^4 dz}{e^z - 1}\right]. \tag{A.40}$$

A.3 Finite Thickness Embedding Media

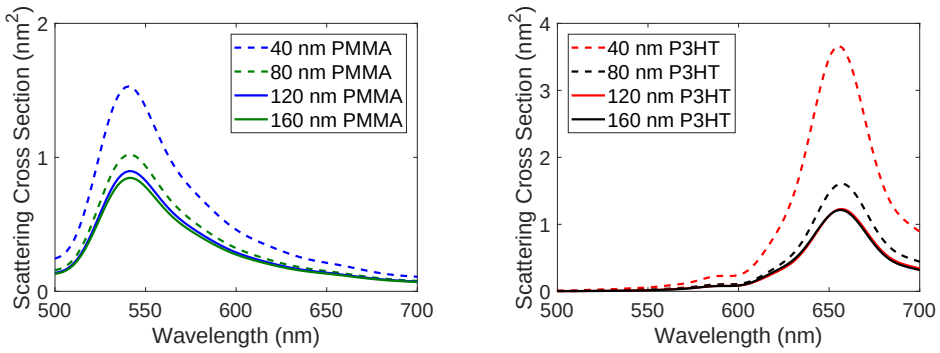

(a) (b)

Figure A.1: FDTD results for the power scattered from a 20 nm gold nanoparticle in films of finite thickness. (a) FDTD results for the power scattered from a 20 nm gold nanoparticle embedded in PMMA films. (b) FDTD results for the power scattered from a 20 nm gold nanoparticle embedded in P3HT films.

Figures A.1 (a) and (b) show the results of FDTD simulations for the scattering cross section of 20 nm gold nanoparticles embedded in films of finite thickness. The

Layer Thickness	Peak	Linewidth
40 nm	541 nm	54 nm
80 nm	541 nm	56 nm
120 nm	541 nm	58 nm
160 nm	541 nm	58 nm

Table A.1: Summary of plasmon peak data from Fig A.1 (a) for a 20 nm gold nanoparticle in layers of PMMA of various thickness.

Layer Thickness	Peak	Linewidth
40 nm	655 nm	42 nm
80 nm	657 nm	42 nm
120 nm	657 nm	42 nm
160 nm	655 nm	42 nm

Table A.2: Summary of plasmon peak data from Fig A.1 (b) for a 20 nm gold nanoparticle in layers of P3HT of various thickness.

goal of these simulations was to find the dependence of the plasmon peak on the thickness of the films. Tables A.1 and A.2 display the peak locations and linewidths for each of these simulations. Table A.1 shows that for PMMA, there is only a small change in the linewidth as the layer thickness is increased. Table A.2 shows that the linewidth for P3HT remains the same over the range of thicknesses analyzed. For both PMMA and P3HT the plasmon peak does not have a strong dependence on the film thickness.

A.4 Nanoparticle Size

Figures A.2 (a) and (b) show the results of Green theory calculations for the normalized scattered power of a single gold nanoparticle in PMMA and in P3HT for different diameters of the gold nanoparticle. Tables A.3 and A.4 show the plasmon peak loca-

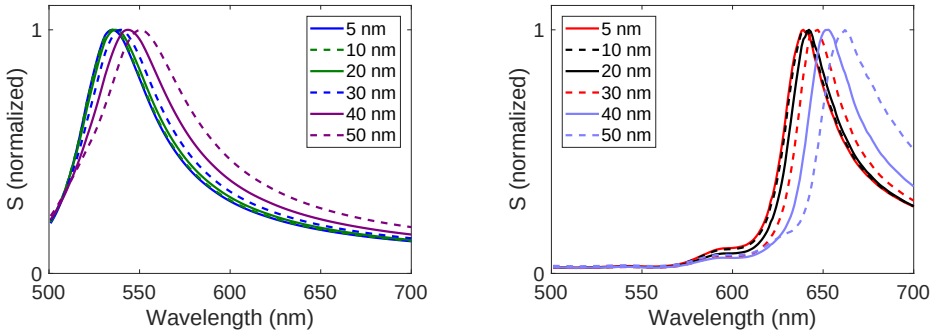

Figure A.2: Green function calculations for scattered power from a single gold nanoparticle in an infinite and homogeneous surrounding medium. In each plot, the numbers in the legend display the gold nanoparticle diameters. (a) Scattering spectrum for gold nanoparticles of varying diameter embedded in PMMA. (b) Scattering spectrum for gold nanoparticles of varying diameter embedded in P3HT.

Nanoparticle size	Peak	Linewidth
5 nm	534 nm	56 nm
10 nm	534 nm	57 nm
20 nm	536 nm	58 nm
30 nm	539 nm	60 nm
40 nm	542 nm	67 nm
50 nm	550 nm	76 nm

Table A.3: Summary of plasmon peak data from Fig A.2 (a) for different size gold nanoparticles in PMMA.

tions and linewidths. For both PMMA and P3HT, the plasmon peaks redshift and the linewidths broaden when the nanoparticle size is increased, so the narrowest linewidth occurs for the smallest nanoparticle. The gradual linewidth broadening is caused by increased radiative damping (plasmon decay via coupling with the radiation field), as the particle size is increased [93, 94]. For both PMMA and P3HT the radiative damping becomes significant for a gold diameter of 30 nm. Surface scattering was not considered in this analysis. Surface scattering causes significant linewidth broad-

Nanoparticle size	Peak	Linewidth
5 nm	636 nm	35 nm
10 nm	636 nm	35 nm
20 nm	639 nm	35 nm
30 nm	644 nm	37 nm
40 nm	650 nm	41 nm
50 nm	659 nm	52 nm

Table A.4: Summary of plasmon peak data from Fig A.2 (b) for a different size gold nanoparticles in P3HT.

ening for small nanoparticles [206, 88]. If surface scattering was included, then the narrowest linewidth would occur for some intermediate particle size where the total damping was minimized.

A.5 Nanoparticle Permittivity

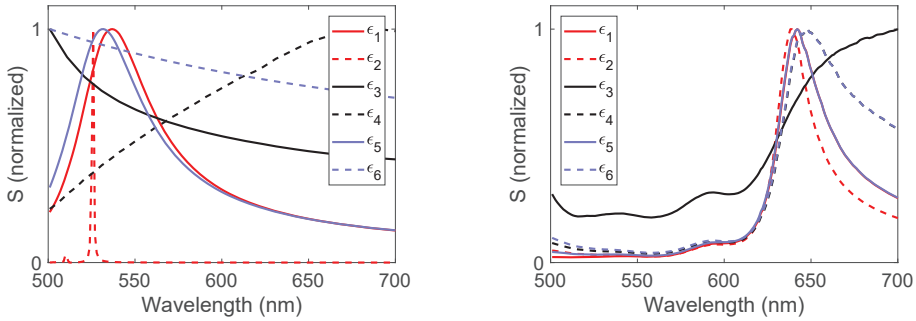

(a) (b)

Figure A.3: Green function spectrum S for various 20 nm metal nanoparticles embedded in infinite and homogeneous PMMA. (a) Scattering spectrum for metal nanoparticles in PMMA. (b) Scattering spectrum for metal nanoparticles in P3HT. Tables A.5 and A.6 show the metal nanoparticle permittivities and summarize the results shown in these figures.

Figures A.3 (a) and (b) show the peaks from various gold-like metals embedded in infinite and homogeneous PMMA and P3HT. Each calculation is done for a single

Permittivity	Peak	Linewidth
$\epsilon_1 = \epsilon_{\text{gold}}$	536 nm	58 nm
$\epsilon_2 = \text{Re}\{\epsilon_{\text{gold}}\}$	525 nm	2 nm
$\epsilon_3 = \text{Im}\{\epsilon_{\text{gold}}\}i$	X	X
$\epsilon_4 = -5.23 + \text{Im}\{\epsilon_{\text{gold}}\}i$	X	X
$\epsilon_5 = \text{Re}\{\epsilon_{\text{gold}}\} + 1.97i$	531 nm	58 nm
$\epsilon_6 = -5.23 + 1.97i$	X	X

Table A.5: Summary of plasmon peaks calculated from Green function spectra for various gold-like metals in infinite and homogeneous PMMA. A row marked with 'X' means there was no plasmon peak for this calculation. The constant values of -5.23 and $1.97i$ were used because at the plasmon peak for gold and PMMA the permittivity of gold is $\epsilon_{\text{gold}} = -5.23 + 1.97i$.

Permittivity	Peak	Linewidth
$\epsilon_1 = \epsilon_{\text{gold}}$	639 nm	35 nm
$\epsilon_2 = \text{Re}\{\epsilon_{\text{gold}}\}$	635 nm	27 nm
$\epsilon_3 = \text{Im}\{\epsilon_{\text{gold}}\}i$	X	X
$\epsilon_4 = -13.3 + \text{Im}\{\epsilon_{\text{gold}}\}i$	647	67
$\epsilon_5 = \text{Re}\{\epsilon_{\text{gold}}\} + 1.02i$	639 nm	35 nm
$\epsilon_6 = -13.3 + 1.02i$	647	68

Table A.6: Summary of plasmon peaks calculated from Green function spectra for various gold-like metals in infinite and homogeneous P3HT. A row marked with 'X' means there was no plasmon peak for this calculation. The constant values of -13.3 and $1.02i$ were used because at the plasmon peak for gold and P3HT the permittivity of gold is $\epsilon_{\text{gold}} = -13.3 + 1.02i$.

20 nm nanoparticle in either PMMA or P3HT. Tables A.5 and A.6 show the nanoparticle permittivities used, and the peak locations and linewidths for each calculation. Three factors significantly affected the linewidth.

Dispersion in the imaginary permittivity of the nanoparticle does not significantly narrow the peak. For plasmons excited with energies below the interband transition of gold (2.4 eV or 517 nm) it is commonly assumed that the dispersion in the imaginary component is negligible compared to the dispersion in the real component, which we verify here [86, 80]. Comparing $\epsilon_1 = \epsilon_{\text{gold}}$ and $\epsilon_5 = \text{Re}\{\epsilon_{\text{gold}}\} + 1.02i$ in Fig. A.3 (a)

which have equal linewidths, and also $\epsilon_1 = \epsilon_{\text{P3HT}}$ and $\epsilon_5 = \text{Re}\{\epsilon_{\text{gold}}\} + 1.02i$ in Fig. A.3 (b) which have equal linewidths, we see the inclusion of the dispersive imaginary part to the nanoparticle permittivity does not change the plasmon peak significantly. Unlike for the surrounding medium analysis in the main paper, there is no steep edge in the plasmon peak due to the dispersive imaginary permittivity of gold. The real permittivity of gold changes much more rapidly than the imaginary permittivity at the plasmon peaks for PMMA and P3HT. Although the dispersion in the imaginary permittivity can alter the plasmon peak very slightly and may cause some degree of linewidth narrowing, it is insignificant compared to the narrowing due to the large real permittivity dispersion. To isolate the effects of dispersion from only the imaginary part of the permittivity, we can compare the results for $\epsilon_4 = -13.3 + \text{Im}\{\epsilon_{\text{gold}}\}i$ and $\epsilon_6 = -13.3 + 1.02i$ from Fig. A.3 (b). The inclusion of the dispersive imaginary part of gold only slightly reduces the linewidth by 1 nm from 68 nm to 67 nm. Also, both $\epsilon_6 = -5.23 + 1.97i$ and $\epsilon_4 = -5.23 + \text{Im}\{\epsilon_{\text{gold}}\}i$ shown in Fig. A.3 (a) do not have plasmon peaks. If the effects of the dispersive imaginary permittivity were significant, there would be a plasmon peak for $\epsilon_4 = -5.23 + \text{Im}\{\epsilon_{\text{gold}}\}i$. Therefore, for a gold nanoparticle, the dispersion in the imaginary permittivity does not contribute significantly to narrowing plasmon linewidths for plasmons below the interband transitions.

Non-dispersive loss in the nanoparticle broadens the linewidth. In Fig. A.3 (a), $\epsilon_2 = \text{Re}\{\epsilon_{\text{gold}}\}$ has an extremely narrow 2 nm peak while the same permittivity

with loss included, $\epsilon_5 = \mathrm{Re}\{\epsilon_{\mathrm{gold}}\} + 1.97i$, has a much broader linewidth of 58 nm. In Fig. A.3 (b), $\epsilon_2 = \mathrm{Re}\{\epsilon_{\mathrm{gold}}\}$ has a 27 nm linewidth and the permittivity $\epsilon_5 = \mathrm{Re}\{\epsilon_{\mathrm{gold}}\}+1.02i$ has a broader 35 nm linewidth. The linewidth is broadened by adding a non-dispersive loss component to the nanoparticle permittivity. The permittivity $\epsilon_2 = \mathrm{Re}\{\epsilon_{\mathrm{gold}}\}$ in PMMA has such a narrow peak because PMMA is also assumed to have no loss, so when the Fröhlich condition is met the scattered power becomes infinite in the quasistatic regime. The reason the peak is not infinite here is because Green theory does not use the quasistatic approximation, so retardation of the field in the nanoparticle leads to radiation damping which will broaden the peak and reduce the scattered power to a finite number. Although having no loss is unphysical, this investigation shows the effectiveness of reducing loss in the nanoparticle for narrowing linewidths.

Dispersion in the real part of the nanoparticle permittivity can narrow linewidths. In Fig. A.3 (a), $\epsilon_1 = \epsilon_{\mathrm{gold}}$ has a peak of 58 nm while there is no plasmon peak for $\epsilon_4 = -5.23 + \mathrm{Im}\{\epsilon_{\mathrm{gold}}\}i$. In Fig. A.3 (b), $\epsilon_1 = \epsilon_{\mathrm{gold}}$ has a linewidth of 35 nm and $\epsilon_4 = -13.3 + \mathrm{Im}\{\epsilon_{\mathrm{gold}}\}i$ has a much broader linewidth of 67 nm. The constant values -5.23 and -13.3 for ϵ_4 in each medium were chosen so that $\epsilon_4 = \epsilon_1$ at the plasmon peak. Thus, the drastic changes in linewidth are due to the large dispersion in the real permittivity of gold, so dispersion in the real permittivity can narrow plasmon linewidths.

A large magnitude of the real permittivity of the nanoparticle can narrow linewidths.

In Figs. A.3 (a) and (b), $\epsilon_3 = \mathrm{Im}\{\epsilon_{\mathrm{gold}}\}i$ do not have plasmon peaks because there is no negative real permittivity (the real component of the permittivity is set to 0). As the magnitude of the permittivity increases to the value at the plasmon peak, the peak gradually narrows. The magnitude of the real permittivity of the metal nanoparticle determines where the plasmon peak is located in the electromagnetic spectrum. Metals commonly used in nanoplasmonics, such as gold and silver, have a large dispersive real permittivity below the plasma frequency. Therefore, a large magnitude in the nanoparticle permittivity can narrow linewidths by shifting the plasmon peak into a regime where there is a large dispersion in the real permittivity of the metal.

A.6 P3HT Scattering Data

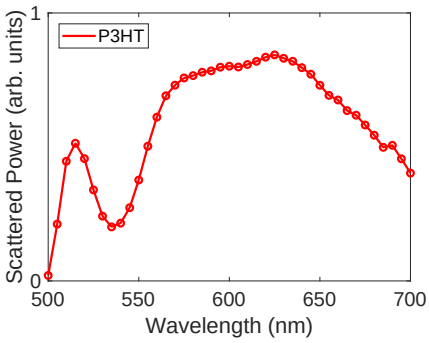

Figure A.4: Scattered power spectrum from a 120 nm layer of P3HT. The red circles are experimental measurements taken in 5 nm increments.

Figure A.4 shows the scattering data from a 120 nm layer of P3HT without any gold nanoparticles. The measurements were taken using the same AOTF dark field microscope described in the main paper. There was no narrow peak at 650 nm as there

was for 120 nm P3HT with embedded 20 nm gold nanoparticles. This data shows that the 650 nm scattering peak present for gold in P3HT is not due to fluorescence or scattering from the P3HT layer.

A.7 Un-normalized Scattering Spectra

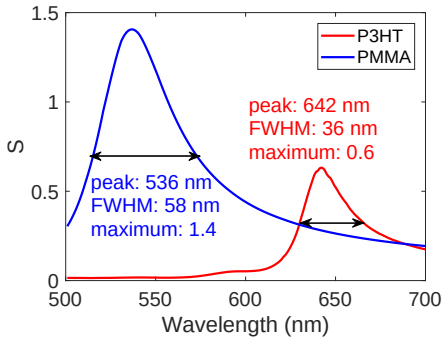

Figure A.5: Green theory scattered power for PMMA and P3HT without normalization.

Here we see the scattering without normalization. Similar results were obtained using numerical simulations with COMSOL, however accounting for the propagation through the absorbing medium complicates the analysis.

A.8 Kramers-krönig Relations

The Kramers-krönig relations were derived nearly a century ago [140, 141]. If we have a complex number $\epsilon = \epsilon_1(\omega) + \epsilon_2(\omega)$ where ϵ_1 and ϵ_2 are real functions of ω, then the

Kramers-krönig relations allow for expressing ϵ_1 in terms of ϵ_2 or vice-versa.

$$\epsilon_1(\omega) = \frac{1}{\pi} P \int_{-\infty}^{\infty} \frac{\epsilon_2(\omega')}{\omega' - \omega} d\omega' \tag{A.41}$$

$$\epsilon_2(\omega) = -\frac{1}{\pi} P \int_{-\infty}^{\infty} \frac{\epsilon_1(\omega')}{\omega' - \omega} d\omega' \tag{A.42}$$

where P is the Cauchy principal value. The Kramers-krönig relations are a general phenomenon and link the imaginary and real parts of a complex impulse function which is assumed to be causal. As long as causality holds, then the Kramers-krönig relations can be applied. For example, in optics, the Kramers-krönig relations can apply to the permittivity, index of refraction, and reflectivity. This has important implications in optics. If we have a complex permittivity, ϵ, then the Kramers-krönig relations link the lossy component to the refractive component. So two seemingly completely independent processes are actually related, and the Kramers-krönig relations connect the lossy and refractive components. This means that only reflectivity or absorption measurements can be made, and if one is known for a broad wavelength range, the other is also known. This effectively halves the work of experimentalists trying to accurately determine the permittivity of materials.

Bibliography

[1] Mirali Seyed Shariatdoust, Adriaan L Frencken, Ali Khademi, Amirhossein Alizadehkhaledi, Frank CJM van Veggel, and Reuven Gordon. Harvesting dual-wavelength excitation with plasmon-enhanced emission from upconverting nanoparticles. *ACS Photonics*, 5(9):3507–3512, 2018.

[2] drinking-cup. https://www.britishmuseum.org/collection/object/H_1958-1202-1.

[3] Donald M Eigler and Erhard K Schweizer. Positioning single atoms with a scanning tunnelling microscope. *Nature*, 344(6266):524–526, 1990.

[4] Richard A Shelby, David R Smith, and Seldon Schultz. Experimental verification of a negative index of refraction. *Science*, 292(5514):77–79, 2001.

[5] Optimisation of sers for glucose sensing. https://www.edinst.com/optimisation-of-sers-for-glucose-sensing/.

[6] Optical tweezers tutorial. https://www.thorlabs.com/newgrouppage9.cfm?objectgroup_id=10

[7] Harry A Atwater and Albert Polman. Plasmonics for improved photovoltaic devices. *Materials for sustainable energy*, pages 1–11, 2011.

[8] Norio Taniguchi. On the basic concept of nanotechnology. *Proceeding of the ICPE*, 1974.

[9] Richard P Feynman. There's plenty of room at the bottom. *Engineering and science*, 23(5), 1959.

[10] Stefan Alexander Maier. *Plasmonics: Fundamentals and Applications*. Springer Science & Business Media, 2007.

[11] Nader Engheta. Circuits with light at nanoscales: optical nanocircuits inspired by metamaterials. *Science*, 317(5845):1698–1702, 2007.

[12] David J Bergman and Mark I Stockman. Surface plasmon amplification by stimulated emission of radiation: quantum generation of coherent surface plasmons in nanosystems. *Phys. Rev. Lett.*, 90:027402, 2003.

[13] Xianzhong Chen, Yu Luo, Jingjing Zhang, Kyle Jiang, John B Pendry, and Shuang Zhang. Macroscopic invisibility cloaking of visible light. *Nat. Commun.*, 2(1):1–6, 2011.

[14] C Zhou, MR Deshpande, MA Reed, L Jones, and JM Tour. Nanoscale metal/self-assembled monolayer/metal heterostructures. *App. Phys. Lett.*, 71(5):611–613, 1997.

[15] Jingwei Bai, Xing Zhong, Shan Jiang, Yu Huang, and Xiangfeng Duan. Graphene nanomesh. *Nat. Nanotechnol.*, 5(3):190–194, 2010.

[16] Bingliu Zhang, Hongbo Tan, Weiguo Shen, Gelong Xu, Baoguo Ma, and Xiaoli Ji. Nano-silica and silica fume modified cement mortar used as surface protection material to enhance the impermeability. *Cem. Concr. Compos.*, 92:7–17, 2018.

[17] Michael FL De Volder, Sameh H Tawfick, Ray H Baughman, and A John Hart. Carbon nanotubes: present and future commercial applications. *science*, 339(6119):535–539, 2013.

[18] Martin Kaltenbrunner, Matthew S White, Eric D Głowacki, Tsuyoshi Sekitani, Takao Someya, Niyazi Serdar Sariciftci, and Siegfried Bauer. Ultrathin and lightweight organic solar cells with high flexibility. *Nat. Commun.*, 3(1):1–7, 2012.

[19] Ricky K Soong, George D Bachand, Hercules P Neves, Anatoli G Olkhovets, Harold G Craighead, and Carlo D Montemagno. Powering an inorganic nanodevice with a biomolecular motor. *Science*, 290(5496):1555–1558, 2000.

[20] Yu Cheng, Anna C Samia, Joseph D Meyers, Irene Panagopoulos, Baowei Fei, and Clemens Burda. Highly efficient drug delivery with gold nanoparti-

cle vectors for in vivo photodynamic therapy of cancer. *J. Am. Chem. Soc.*, 130(32):10643–10647, 2008.

[21] James F Hainfeld, Henry M Smilowitz, Michael J O'Connor, Farrokh Avraham Dilmanian, and Daniel N Slatkin. Gold nanoparticle imaging and radiotherapy of brain tumors in mice. *Nanomedicine*, 8(10):1601–1609, 2013.

[22] Betty YS Kim, James T Rutka, and Warren CW Chan. Nanomedicine. *N. Engl. J. Med.*, 363(25):2434–2443, 2010.

[23] Yuanjie Pang and Reuven Gordon. Optical trapping of a single protein. *Nano Lett.*, 12(1):402–406, 2012.

[24] Katrin Kneipp, Yang Wang, Harald Kneipp, Lev T. Perelman, Irving Itzkan, Ramachandra R. Dasari, and Michael S. Feld. Single molecule detection using surface-enhanced raman scattering (sers). *Phys. Rev. Lett.*, 78:1667–1670, Mar 1997.

[25] Hyungsoon Im, Huilin Shao, Yong Il Park, Vanessa M Peterson, Cesar M Castro, Ralph Weissleder, and Hakho Lee. Label-free detection and molecular profiling of exosomes with a nano-plasmonic sensor. *Nat. biotechnol.*, 32(5):490–495, 2014.

[26] Reto B Schoch, Jongyoon Han, and Philippe Renaud. Transport phenomena in nanofluidics. *Rev. Mod. Phys.*, 80(3):839, 2008.

[27] Alexandre G Brolo, Reuven Gordon, Brian Leathem, and Karen L Kavanagh. Surface plasmon sensor based on the enhanced light transmission through arrays of nanoholes in gold films. *Langmuir*, 20(12):4813–4815, 2004.

[28] Daniel R Solli and Bahram Jalali. Analog optical computing. *Nat. Photonics*, 9(11):704–706, 2015.

[29] Mehmet Fatih Yanik, Shanhui Fan, Marin Soljačić, and John D Joannopoulos. All-optical transistor action with bistable switching in a photonic crystal cross-waveguide geometry. *Opt. Lett.*, 28(24):2506–2508, 2003.

[30] Xiangyu Dong, Xiaoxia Wu, Guangyu Sun, Yuan Xie, Helen Li, and Yiran Chen. Circuit and microarchitecture evaluation of 3d stacking magnetic ram (mram) as a universal memory replacement. In *2008 45th ACM/IEEE Design Automation Conference*, pages 554–559. Institute of Electrical and Electronics Engineers, 2008.

[31] Tae-Ho Kim et al. Full-colour quantum dot displays fabricated by transfer printing. *Nat. Photonics*, 5(3):176–182, 2011.

[32] 2020's statistical review on nanotechnology publications. https://statnano.com/news/68509/2020%E2%80%99s-Statistical-Review-on-Nanotechnology-Publications.

[33] Nni supplement to the president's 2021 budget. https://www.nano.gov/2021BudgetSupplement.

[34] Sumio Iijima. Helical microtubules of graphitic carbon. *Nature*, 354(6348):56–58, 1991.

[35] Philip Petersen, Grigory Tikhomirov, and Lulu Qian. Information-based autonomous reconfiguration in systems of interacting dna nanostructures. *Nat. Commun.*, 9(1):1–10, 2018.

[36] Roshdi Rashed. A pioneer in anaclastics: Ibn sahl on burning mirrors and lenses. *Isis*, 81(3):464–491, 1990.

[37] Max Planck. On the law of the energy distribution in the normal spectrum. *Ann. Phys.*, 4(553):1–11, 1901.

[38] AB Arons and MB Peppard. Einstein's proposal of the photon concept—a translation of the annalen der physik paper of 1905. *Am. J. Phys.*, 33(5):367–374, 1965.

[39] Jonathan A Scholl, Ai Leen Koh, and Jennifer A Dionne. Quantum plasmon resonances of individual metallic nanoparticles. *Nature*, 483(7390):421, 2012.

[40] Arthur Ashkin. Acceleration and trapping of particles by radiation pressure. *Phys. Rev. Lett.*, 24(4):156, 1970.

[41] Abhay Kotnala and Reuven Gordon. Double nanohole optical tweezers visualize protein p53 suppressing unzipping of single dna-hairpins. *Biomed. Opt. Express*, 5(6):1886–1894, 2014.

[42] Frank C Spano and Carlos Silva. H- and j-aggregate behavior in polymeric semiconductors. *Annu. Rev. Phys. Chem.*, 65:477–500, 2014.

[43] WQ Hu, EJ Liang, P Ding, GW Cai, and QZ Xue. Surface plasmon resonance and field enhancement in #-shaped gold wires metamaterial. *Opt. Express*, 17(24):21843–21849, 2009.

[44] Shuming Nie and Steven R Emory. Probing single molecules and single nanoparticles by surface-enhanced raman scattering. *Science*, 275(5303):1102–1106, 1997.

[45] XiaoQiang Zhang, Walter J Salcedo, Mohammad M Rahman, and Alexandre G Brolo. Surface-enhanced raman scattering from bowtie nanoaperture arrays. *Surf. Sci.*, 676:39–45, 2018.

[46] Mathieu L Juan, Maurizio Righini, and Romain Quidant. Plasmon nano-optical tweezers. *Nat. Photonics*, 5(6):349, 2011.

[47] Yuanjie Pang and Reuven Gordon. Optical trapping of a single protein. *Nano Lett.*, 12(1):402–406, 2011.

[48] Brian J Roxworthy, Kaspar D Ko, Anil Kumar, Kin Hung Fung, Edmond KC Chow, Gang Logan Liu, Nicholas X Fang, and Kimani C Toussaint Jr. Application of plasmonic bowtie nanoantenna arrays for optical trapping, stacking, and sorting. *Nano Lett.*, 12(2):796–801, 2012.

[49] Bo Liedberg, Claes Nylander, and Ingemar Lunström. Surface plasmon resonance for gas detection and biosensing. *Sens. Actuators*, 4:299–304, 1983.

[50] AV Kabashin, P Evans, S Pastkovsky, W Hendren, GA Wurtz, R Atkinson, R Pollard, VA Podolskiy, and AV Zayats. Plasmonic nanorod metamaterials for biosensing. *Nat. Mater.*, 8:867, 2009.

[51] Mark I Stockman. Nanoplasmonic sensing and detection. *Science*, 348:287–288, 2015.

[52] Yijun Tang, Xiangqun Zeng, and Jennifer Liang. Surface plasmon resonance: an introduction to a surface spectroscopy technique. *J. Chem. Educ.*, 87(7):742–746, 2010.

[53] Aftab Ahmed and Reuven Gordon. Single molecule directivity enhanced raman scattering using nanoantennas. *Nano Lett.*, 12(5):2625–2630, 2012.

[54] Alexandre G Brolo. Plasmonics for future biosensors. *Nat. Photonics*, 6(11):709, 2012.

[55] Weibo Cai, Ting Gao, Hao Hong, and Jiangtao Sun. Applications of gold nanoparticles in cancer nanotechnology. *Nanotechnol., Sci. Appl.*, 1:17, 2008.

[56] Matthew D Arnold and Richard J Blaikie. Subwavelength optical imaging of evanescent fields using reflections from plasmonic slabs. *Opt. Express*, 15(18):11542–11552, 2007.

[57] Joseph W Nelson, Greta R Knefelkamp, Alexandre G Brolo, and Nathan C Lindquist. Digital plasmonic holography. *Light: Sci. Appl.*, 7(1):52, 2018.

[58] Changtao Wang, Ping Gao, Zeyu Zhao, Na Yao, Yanqin Wang, Ling Liu, Kaipeng Liu, and Xiangang Luo. Deep sub-wavelength imaging lithography by a reflective plasmonic slab. *Opt. Express*, 21(18):20683–20691, 2013.

[59] N Engheta, A Alù, and A Salandrino. Nanocircuit elements, nano-transmission lines and nano-antennas using plasmonic materials in the optical domain. In *IWAT 2005. IEEE International Workshop on Antenna Technology: Small Antennas and Novel Metamaterials, 2005*, pages 165–168. Institute of Electrical and Electronics Engineers, 2005.

[60] Stefan A Maier and Harry A Atwater. Plasmonics: localization and guiding of electromagnetic energy in metal/dielectric structures. *J. Appl. Phys. (Melville, NY, U. S.)*, 98(1):10, 2005.

[61] Ekmel Ozbay. Plasmonics: merging photonics and electronics at nanoscale dimensions. *Science*, 311(5758):189–193, 2006.

[62] Nader Engheta, Alessandro Salandrino, and Andrea Alù. Circuit elements at optical frequencies: nanoinductors, nanocapacitors, and nanoresistors. *Phys. Rev. Lett.*, 95:095504, 2005.

[63] François Auzel. Upconversion and anti-stokes processes with f and d ions in solids. *Chem. Rev. (Washington, DC, U. S.)*, 104:139–174, 2004.

[64] Stefan Schietinger, Thomas Aichele, Hai-Qiao Wang, Thomas Nann, and Oliver Benson. Plasmon-enhanced upconversion in single $nayf_4$: $yb_3 + /er_3+$ codoped nanocrystals. *Nano lett.*, 10:134–138, 2009.

[65] Wounjhang Park, Dawei Lu, and Sungmo Ahn. Plasmon enhancement of luminescence upconversion. *Chem. Soc. Rev.*, 44:2940–2962, 2015.

[66] CK Hong and L Mandel. Theory of parametric frequency down conversion of light. *Phys. Rev. A*, 31:2409, 1985.

[67] Maciej Lewenstein, Ph Balcou, M Yu Ivanov, Anne L'huillier, and Paul B Corkum. Theory of high-harmonic generation by low-frequency laser fields. *Phys. Rev. A*, 49:2117, 1994.

[68] Seungchul Kim, Jonghan Jin, Young-Jin Kim, In-Yong Park, Yunseok Kim, and Seung-Woo Kim. High-harmonic generation by resonant plasmon field enhancement. *Nature (London)*, 453:757, 2008.

[69] Bernd Metzger, Lili Gui, Jaco Fuchs, Dominik Floess, Mario Hentschel, and Harald Giessen. Strong enhancement of second harmonic emission by plasmonic resonances at the second harmonic wavelength. *Nano lett.*, 15:3917–3922, 2015.

[70] Michele Celebrano et al. Mode matching in multiresonant plasmonic nanoantennas for enhanced second harmonic generation. *Nat. Nanotechnol.*, 10:412, 2015.

[71] Barry P Rand, Peter Peumans, and Stephen R Forrest. Long-range absorption enhancement in organic tandem thin-film solar cells containing silver nanoclusters. *J. Appl. Phys. (Melville, NY, U. S.)*, 96(12):7519–7526, 2004.

[72] Vivian E Ferry, Jeremy N Munday, and Harry A Atwater. Design considerations for plasmonic photovoltaics. *Adv. Mater.*, 22(43):4794–4808, 2010.

[73] Matthew R Jones, Kyle D Osberg, Robert J Macfarlane, Mark R Langille, and Chad A Mirkin. Templated techniques for the synthesis and assembly of plasmonic nanostructures. *Chemical Reviews*, 111(6):3736–3827, 2011.

[74] Marco Notarianni, Kristy Vernon, Alison Chou, Muhsen Aljada, Jinzhang Liu, and Nunzio Motta. Plasmonic effect of gold nanoparticles in organic solar cells. *Sol. Energy*, 106:23–37, 2014.

[75] Jan Becker, Inga Zins, Arpad Jakab, Yuriy Khalavka, Olaf Schubert, and Carsten Sönnichsen. Plasmonic focusing reduces ensemble linewidth of silver-coated gold nanorods. *Nano Lett.*, 8(6):1719–1723, 2008.

[76] Yizhuo Chu, Ethan Schonbrun, Tian Yang, and Kenneth B Crozier. Experimental observation of narrow surface plasmon resonances in gold nanoparticle arrays. *Applied Physics Letters*, 93(18):181108, 2008.

[77] Yongkang Gao, Zheming Xin, Qiaoqiang Gan, Xuanhong Cheng, and Filbert J Bartoli. Plasmonic interferometers for label-free multiplexed sensing. *Optics express*, 21(5):5859–5871, 2013.

[78] Leif J Sherry, Shih-Hui Chang, George C Schatz, Richard P Van Duyne, Benjamin J Wiley, and Younan Xia. Localized surface plasmon resonance spectroscopy of single silver nanocubes. *Nano Lett.*, 5(10):2034–2038, 2005.

[79] Stephan Link and Mostafa A El-Sayed. Size and temperature dependence of the plasmon absorption of colloidal gold nanoparticles. *J. Phys. Chem. B*, 103(21):4212–4217, 1999.

[80] U Kreibig. Small silver particles in photosensitive glass: their nucleation and growth. *Appl. Phys. (Berlin)*, 10(3):255–264, 1976.

[81] RN Gurzhi. Mutual electron correlations in metal optics. *Sov. Phys. JETP*, 8(4):673–675, 1959.

[82] WE Lawrence and JW Wilkins. Electron-electron scattering in the transport coefficients of simple metals. *Phys. Rev. B*, 7(6):2317, 1973.

[83] GR Parkins, WE Lawrence, and RW Christy. Intraband optical conductivity σ (ω, t) of cu, ag, and au: Contribution from electron-electron scattering. *Phys. Rev. B*, 23(12):6408, 1981.

[84] T Holstein. Theory of transport phenomena in an electron-phonon gas. *Ann. Phys. (Amsterdam, Neth.)*, 29(3):410–535, 1964.

[85] J A McKay and J A Rayne. Temperature dependence of the infrared absorptivity of the noble metals. *Phys. Rev. B*, 13(2):673, 1976.

[86] Gregory V Hartland. Optical studies of dynamics in noble metal nanostructures. *Chemical reviews*, 111(6):3858–3887, 2011.

[87] Carolina Novo, Daniel Gomez, Jorge Perez-Juste, Zhenyuan Zhang, Hristina Petrova, Maximilian Reismann, Paul Mulvaney, and Gregory V Hartland. Contributions from radiation damping and surface scattering to the linewidth of

the longitudinal plasmon band of gold nanorods: a single particle study. *Phys. Chem. Chem. Phys.*, 8(30):3540–3546, 2006.

[88] U Kreibig and LJSS Genzel. Optical absorption of small metallic particles. *Surf. Sci.*, 156:678–700, 1985.

[89] Martin G Blaber, Matthew D Arnold, and Michael J Ford. Search for the ideal plasmonic nanoshell: the effects of surface scattering and alternatives to gold and silver. *J. Phys. Chem. C*, 113(8):3041–3045, 2009.

[90] Marcos M Alvarez, Joseph T Khoury, T Gregory Schaaff, Marat N Shafigullin, Igor Vezmar, and Robert L Whetten. Optical absorption spectra of nanocrystal gold molecules. *J. Phys. Chem. B*, 101(19):3706–3712, 1997.

[91] H Hövel, S Fritz, A Hilger, U Kreibig, and Michael Vollmer. Width of cluster plasmon resonances: bulk dielectric functions and chemical interface damping. *Phys. Rev. B*, 48(24):18178, 1993.

[92] Colleen L Nehl, Nathaniel K Grady, Glenn P Goodrich, Felicia Tam, Naomi J Halas, and Jason H Hafner. Scattering spectra of single gold nanoshells. *Nano Lett.*, 4(12):2355–2359, 2004.

[93] A Wokaun, JP Gordon, and PF Liao. Radiation damping in surface-enhanced raman scattering. *Phys. Rev. Lett.*, 48:957, 1982.

[94] Th Kokkinakis and K Alexopoulos. Observation of radiative decay of surface plasmons in small silver particles. *Phys. Rev. Lett.*, 28(25):1632, 1972.

[95] Mingzhao Liu, Matthew Pelton, Philippe Guyot-Sionnest, et al. Reduced damping of surface plasmons at low temperatures. *Phys. Rev. B*, 79(3):035418, 2009.

[96] C Hendrich, J Bosbach, F Stietz, F Hubenthal, T Vartanyan, and F Träger. Chemical interface damping of surface plasmon excitation in metal nanoparticles: a study by persistent spectral hole burning. *Appl. Phys. B: Lasers Opt.*, 76(8):869–875, 2003.

[97] Benjamin Foerster, Anneli Joplin, Katharina Kaefer, Sirin Celiksoy, Stephan Link, and Carsten Sönnichsen. Chemical interface damping depends on electrons reaching the surface. *ACS nano*, 11(3):2886–2893, 2017.

[98] Andrew J Therrien, Matthew J Kale, Lin Yuan, Chao Zhang, Naomi J Halas, and Phillip Christopher. Impact of chemical interface damping on surface plasmon dephasing. *Faraday Discuss.*, 214:59–72, 2019.

[99] Lev Davidovich Landau. *Oscillations of an Electron Plasma*. US Atomic Energy Commission, 1946.

[100] John Dawson. On landau damping. *Phys. Fluids*, 4(7):869–874, 1961.

[101] DD Ryutov. Landau damping: half a century with the great discovery. *Plasma Phys. Controlled Fusion*, 41(3A):A1, 1999.

[102] JH Malmberg and CB Wharton. Collisionless damping of electrostatic plasma waves. *Phys. Rev. Lett.*, 13(6):184, 1964.

[103] Martin Perner, P Bost, U Lemmer, G Von Plessen, J Feldmann, Ulrich Becker, Martin Mennig, M Schmitt, and H Schmidt. Optically induced damping of the surface plasmon resonance in gold colloids. *Phys. Rev. Lett.*, 78(11):2192, 1997.

[104] Justus C Ndukaife, Vladimir M Shalaev, and Alexandra Boltasseva. Plasmonics—turning loss into gain. *Science*, 351:334–335, 2016.

[105] Israel De Leon and Pierre Berini. Spontaneous emission in long-range surface plasmon-polariton amplifiers. *Phys. Rev. B*, 83(8):081414, 2011.

[106] Jacob B Khurgin. How to deal with the loss in plasmonics and metamaterials. *Nat. Nanotechnol.*, 10:2, 2015.

[107] Paul R West, Satoshi Ishii, Gururaj V Naik, Naresh K Emani, Vladimir M Shalaev, and Alexandra Boltasseva. Searching for better plasmonic materials. *Laser Photonics Rev.*, 4:795–808, 2010.

[108] Xin Guo, Yaoguang Ma, Yipei Wang, and Limin Tong. Nanowire plasmonic waveguides, circuits and devices. *Laser Photonics Rev.*, 7(6):855–881, 2013.

[109] Jana Olson, Sergio Dominguez-Medina, Anneli Hoggard, Lin-Yung Wang, Wei-Shun Chang, and Stephan Link. Optical characterization of single plasmonic nanoparticles. *Chem. Soc. Rev.*, 44(1):40–57, 2015.

[110] Shunping Zhang, Li Chen, Yingzhou Huang, and Hongxing Xu. Reduced linewidth multipolar plasmon resonances in metal nanorods and related applications. *Nanoscale*, 5(15):6985–6991, 2013.

[111] Ugo Fano. Effects of configuration interaction on intensities and phase shifts. *Phys. Rev.*, 124(6):1866, 1961.

[112] Wei Cao, Ranjan Singh, Ibraheem AI Al-Naib, Mingxia He, Antoinette J Taylor, and Weili Zhang. Low-loss ultra-high-q dark mode plasmonic fano metamaterials. *Opt. Lett.*, 37:3366–3368, 2012.

[113] Dmitry Khlopin, Frédéric Laux, William P Wardley, Jérôme Martin, Gregory A Wurtz, Jérôme Plain, Nicolas Bonod, Anatoly V Zayats, Wayne Dickson, and Davy Gérard. Lattice modes and plasmonic linewidth engineering in gold and aluminum nanoparticle arrays. *J. Opt. Soc. Am. B*, 34(3):691–700, 2017.

[114] VG Kravets, F Schedin, and AN Grigorenko. Extremely narrow plasmon resonances based on diffraction coupling of localized plasmons in arrays of metallic nanoparticles. *Phys. Rev. Lett.*, 101:087403, 2008.

[115] Wei Zhou and Teri W Odom. Tunable subradiant lattice plasmons by out-of-plane dipolar interactions. *Nat. Nanotechnol.*, 6:423, 2011.

[116] Yang Shen et al. Plasmonic gold mushroom arrays with refractive index sensing figures of merit approaching the theoretical limit. *Nat. Commun.*, 4:2381, 2013.

[117] Bowen Liu et al. A plasmonic sensor array with ultrahigh figures of merit and resonance linewidths down to 3 nm. *Adv. Mat.*, 30:1706031, 2018.

[118] Ali Sobhani, Alejandro Manjavacas, Yang Cao, Michael J McClain, F Javier Garcia de Abajo, Peter Nordlander, and Naomi J Halas. Pronounced linewidth narrowing of an aluminum nanoparticle plasmon resonance by interaction with an aluminum metallic film. *Nano Lett.*, 15(10):6946–6951, 2015.

[119] Guang-Can Li, Yong-Liang Zhang, Jing Jiang, Yu Luo, and Dang Yuan Lei. Metal-substrate-mediated plasmon hybridization in a nanoparticle dimer for photoluminescence line-width shrinking and intensity enhancement. *ACS nano*, 11(3):3067–3080, 2017.

[120] Arif E Cetin and Hatice Altug. Fano resonant ring/disk plasmonic nanocavities on conducting substrates for advanced biosensing. *ACS nano*, 6(11):9989–9995, 2012.

[121] MA Noginov, G Zhu, M Bahoura, J Adegoke, CE Small, BA Ritzo, VP Drachev, and VM Shalaev. Enhancement of surface plasmons in an ag aggregate by optical gain in a dielectric medium. *Optics Lett.*, 31(20):3022–3024, 2006.

[122] K Sathiyamoorthy, KV Sreekanth, R Sidharthan, VM Murukeshan, and Bengang Xing. Surface plasmon enhancement in gold nanoparticles in the presence

of an optical gain medium: an analysis. *J. Phys. D: Appl. Phys.*, 44(42):425102, 2011.

[123] Lijun Meng, Ding Zhao, Yuanqing Yang, F Javier García De Abajo, Qiang Li, Zhichao Ruan, and Min Qiu. Gain-assisted plasmon resonance narrowing and its application in sensing. *Phys. Rev. Appl.*, 11(4):044030, 2019.

[124] Nikolay I Zheludev, SL Prosvirnin, N Papasimakis, and VA Fedotov. Lasing spaser. *Nat. Photonics*, 2(6):351, 2008.

[125] MA Noginov, G Zhu, AM Belgrave, Reuben Bakker, VM Shalaev, EE Narimanov, S Stout, E Herz, T Suteewong, and U Wiesner. Demonstration of a spaser-based nanolaser. *Nature*, 460(7259):1110–1112, 2009.

[126] Mark I Stockman. Brief history of spaser from conception to the future. *Adv. Photonics*, 2(5):054002, 2020.

[127] Vladimir Kochergin, Lauren Neely, Chih-Yu Jao, and Hans D Robinson. Aluminum plasmonic nanostructures for improved absorption in organic photovoltaic devices. *Appl. Phys. Lett.*, 98(13):73, 2011.

[128] Marina Stavytska-Barba, Michael Salvador, Abhishek Kulkarni, David S Ginger, and Anne Myers Kelley. Plasmonic enhancement of raman scattering from the organic solar cell material p3ht/pcbm by triangular silver nanoprisms. *J. Phys. Chem. C*, 115(42):20788–20794, 2011.

[129] Abhishek P Kulkarni, Kevin M Noone, Keiko Munechika, Samuel R Guyer, and David S Ginger. Plasmon-enhanced charge carrier generation in organic photovoltaic films using silver nanoprisms. *Nano Lett.*, 10(4):1501–1505, 2010.

[130] Gustav Mie. Die optischen eigenschaften kolloider goldlösungen. *Colloid Polym. Sci.*, 2(5):129–133, 1907.

[131] Gustav Mie. Beiträge zur optik trüber medien, speziell kolloidaler metallösungen. *Ann. Phys. (Berlin, Ger.)*, 330(3):377–445, 1908.

[132] WC Mundy, JA Roux, and AM Smith. Mie scattering by spheres in an absorbing medium. *J. Opt. Soc. Am. A*, 64(12):1593–1597, 1974.

[133] Craig F Bohren and Daya P Gilra. Extinction by a spherical particle in an absorbing medium. *J. Colloid Interface Sci.*, 72(2):215–221, 1979.

[134] AN Lebedev, M Gartz, U Kreibig, and O Stenzel. Optical extinction by spherical particles in an absorbing medium: application to composite absorbing films. *Eur. Phys. J. D*, 6(3):365–373, 1999.

[135] I Wayan Sudiarta and Petr Chylek. Mie-scattering formalism for spherical particles embedded in an absorbing medium. *J. Opt. Soc. Am. A*, 18(6):1275–1278, 2001.

[136] Qiang Fu and Wenbo Sun. Mie theory for light scattering by a spherical particle in an absorbing medium. *Appl. Opt.*, 40(9):1354–1361, 2001.

[137] Ping Yang et al. Inherent and apparent scattering properties of coated or uncoated spheres embedded in an absorbing host medium. *Appl. Opt.*, 41(15):2740–2759, 2002.

[138] Gorden Videen and Wenbo Sun. Yet another look at light scattering from particles in absorbing media. *Appl. Opt.*, 42(33):6724–6727, 2003.

[139] Michael I Mishchenko. Electromagnetic scattering by a fixed finite object embedded in an absorbing medium. *Opt. Express*, 15(20):13188–13202, 2007.

[140] R de L Kronig. On the theory of dispersion of x-rays. *J. Opt. Soc. Am. A*, 12(6):547–557, 1926.

[141] Hendrik Anthony Kramers. La diffusion de la lumiere par les atomes. In *Atti Cong. Intern. Fisica (Transactions of Volta Centenary Congress) Como*, volume 2, pages 545–557, 1927.

[142] Richard P Feynman, Robert B Leighton, and Matthew Sands. *The Feynman Lectures on Physics, Vol. I: The New Millennium Edition: Mainly Mechanics, Radiation, and Heat*, volume 1. Basic Books, 2011.

[143] Min Hu, Carolina Novo, Alison Funston, Haining Wang, Hristina Staleva, Shengli Zou, Paul Mulvaney, Younan Xia, and Gregory V Hartland. Dark-field microscopy studies of single metal nanoparticles: understanding the factors that

influence the linewidth of the localized surface plasmon resonance. *J. Mater. Chem.*, 18(17):1949–1960, 2008.

[144] Hyeon-Ho Jeong, Andrew G Mark, Mariana Alarcón-Correa, Insook Kim, Peter Oswald, Tung-Chun Lee, and Peer Fischer. Dispersion and shape engineered plasmonic nanosensors. *Nat. Commun.*, 7(1):1–7, 2016.

[145] Paul Drude. Zur elektronentheorie der metalle. *Ann. Phys. (Berlin, Ger.)*, 306(3):566–613, 1900.

[146] Peter B Johnson and R W Christy. Optical constants of the noble metals. *Phys. Rev. B*, 6:4370, 1972.

[147] HS Sehmi, Wolfgang Langbein, and EA Muljarov. Optimizing the drude-lorentz model for material permittivity: Method, program, and examples for gold, silver, and copper. *Phys. Rev. B*, 95(11):115444, 2017.

[148] Mohamed Kadi, Assia Smaali, and Ratiba Outemzabet. Analysis of optical and related properties of tin oxide thin films determined by drude-lorentz model. *Surf. Coat. Technol.*, 211:45–49, 2012.

[149] Jun Shibayama, Ryoji Ando, Akifumi Nomura, Junji Yamauchi, and Hisamatsu Nakano. Simple trapezoidal recursive convolution technique for the frequency-dependent fdtd analysis of a drude–lorentz model. *IEEE Photonics Technol. Lett.*, 21(2):100–102, 2008.

[150] Dmitriy V Likhachev, Natalia Malkova, and Leonid Poslavsky. Modified tauc–lorentz dispersion model leading to a more accurate representation of absorption features below the bandgap. *Thin Solid Films*, 589:844–851, 2015.

[151] Nidhi Sharma, Angela Joy, Akhilesh Kumar Mishra, and Rajneesh Kumar Verma. Fuchs sondheimer–drude lorentz model and drude model in the study of spr based optical sensors: A theoretical study. *Opt. Commun.*, 357:120–126, 2015.

[152] Yong Sun, Brian Edwards, Andrea Alù, and Nader Engheta. Experimental realization of optical lumped nanocircuits at infrared wavelengths. *Nat. Mat.*, 11(3):208–212, 2012.

[153] WR Premasiri, DT Moir, MS Klempner, N Krieger, G Jones, and LD Ziegler. Characterization of the surface enhanced raman scattering (sers) of bacteria. *J. Phys. Chem. B*, 109(1):312–320, 2005.

[154] Eric C Le Ru, Evan Blackie, Matthias Meyer, and Pablo G Etchegoin. Surface enhanced raman scattering enhancement factors: a comprehensive study. *J. Phys. Chem. C*, 111(37):13794–13803, 2007.

[155] Jeffrey N Anker, W Paige Hall, Olga Lyandres, Nilam C Shah, Jing Zhao, and Richard P Van Duyne. Biosensing with plasmonic nanosensors. *World Sci. Ser. Nanosci. Nanotechnol.*, pages 308–319, 2010.

[156] K R Catchpole, , and Albert Polman. Plasmonic solar cells. *Opt. Express*, 16(26):21793–21800, 2008.

[157] Arthur Ashkin and James M Dziedzic. Optical trapping and manipulation of viruses and bacteria. *Science*, 235(4795):1517–1520, 1987.

[158] T Klar, M Perner, S Grosse, G Von Plessen, W Spirkl, and J Feldmann. Surface-plasmon resonances in single metallic nanoparticles. *Phys. Rev. Lett.*, 80:4249, 1998.

[159] C Sönnichsen, T Franzl, T Wilk, G Von Plessen, and J Feldmann. Plasmon resonances in large noble-metal clusters. *New J. Phys.*, 4:93, 2002.

[160] Michael I Mishchenko and Janna M Dlugach. Plasmon resonances of metal nanoparticles in an absorbing medium. *OSA Continuum*, 2:3415–3421, 2019.

[161] Lord Rayleigh. *On the Scattering of Light by Small Particles*, volume 41. Taylor & Francis 41, 447–451, 1871.

[162] Richard Gans. Über die form ultramikroskopischer goldteilchen. *Ann. Phys. (Berlin, Ger.)*, 342(5):881–900, 1912.

[163] Arthur L Aden and Milton Kerker. Scattering of electromagnetic waves from two concentric spheres. *J. Appl. Phys.*, 22(10):1242–1246, 1951.

[164] Thibault Honegger, K Berton, E Picard, and D Peyrade. Determination of clausius–mossotti factors and surface capacitances for colloidal particles. *Appl. Phys. Lett.*, 98(18):181906, 2011.

[165] A Lakhtakia. On extinction in a homogeneous chiral medium. *Optik*, 99:35–39, 1994.

[166] Ryan Peck, Ali Khademi, Juanjuan Ren, Stephen Hughes, Alexandre G Brolo, and Reuven Gordon. Plasmonic linewidth narrowing by encapsulation in a dispersive absorbing material. *Phys. Rev. Res.*, 3(1):013014, 2021.

[167] Cole Van Vlack, Philip Trøst Kristensen, and Stephen Hughes. Spontaneous emission spectra and quantum light-matter interactions from a strongly coupled quantum dot metal-nanoparticle system. *Phys. Rev. B*, 85:075303, 2012.

[168] Maurizio Dapor. Appendix g: The kramers–kronig relations and the sum rules. In *Transport of Energetic Electrons in Solids*, pages 175–178. Springer, 2017.

[169] Nikolai G Khlebtsov. Extinction, absorption, and scattering of light by plasmonic spheres embedded in an absorbing host medium. *Phys. Chem. Chem. Phys.*, 23(40):23141–23157, 2021.

[170] Philipp Löper, Michael Stuckelberger, Bjoern Niesen, Jérémie Werner, Miha Filipič, Soo-Jin Moon, Jun-Ho Yum, Marko Topič, Stefaan De Wolf, and Christophe Ballif. Complex refractive index spectra of $ch_3nh_3pbi_3$ perovskite

thin films determined by spectroscopic ellipsometry and spectrophotometry. *J. Phys. Chem. Lett.*, 6(1):66–71, 2015.

[171] Jérémie Werner, Gizem Nogay, Florent Sahli, Terry Chien-Jen Yang, Matthias Bräuninger, Gabriel Christmann, Arnaud Walter, Brett A Kamino, Peter Fiala, Philipp Löper, et al. Complex refractive indices of cesium–formamidinium-based mixed-halide perovskites with optical band gaps from 1.5 to 1.8 ev. *ACS Energy Lett.*, 3(3):742–747, 2018.

[172] Ching W Tang. Multilayer organic photovoltaic elements, 1979. US Patent 4,164,431.

[173] Ching W Tang. Two-layer organic photovoltaic cell. *Appl. Phys. Lett.*, 48(2):183–185, 1986.

[174] NS Sariciftci, L Smilowitz, AJ Heeger, and F Wudl. Semiconducting polymers (as donors) and buckminsterfullerene (as acceptor): photoinduced electron transfer and heterojunction devices. *Synth. Met.*, 59(3):333–352, 1993.

[175] Gang Yu, Jun Gao, Jan C Hummelen, Fred Wudl, and Alan J Heeger. Polymer photovoltaic cells: enhanced efficiencies via a network of internal donor-acceptor heterojunctions. *Science*, 270(5243):1789–1791, 1995.

[176] Lingxian Meng et al. Organic and solution-processed tandem solar cells with 17.3% efficiency. *Science*, 361(6407):1094–1098, 2018.

[177] Andreas Distler, Christoph J Brabec, and Hans-Joachim Egelhaaf. Organic photovoltaic modules with new world record efficiencies. *Prog. Photovoltaics*, 29(1):24–31, 2021.

[178] William Shockley and Hans J Queisser. Detailed balance limit of efficiency of p-n junction solar cells. *J. Appl. Phys.*, 32(3):510–519, 1961.

[179] Kunta Yoshikawa et al. Silicon heterojunction solar cell with interdigitated back contacts for a photoconversion efficiency over 26%. *Nat. Energy*, 2(5):1–8, 2017.

[180] Naeimeh Torabi, Abbas Behjat, Yinhua Zhou, Pablo Docampo, Ryan J Stoddard, Hugh W Hillhouse, and Tayebeh Ameri. Progress and challenges in perovskite photovoltaics from single-to multi-junction cells. *Mater. Today Energy*, 12:70–94, 2019.

[181] Akshay Rao and Richard H Friend. Harnessing singlet exciton fission to break the shockley–queisser limit. *Nat. Rev. Mater.*, 2(11):1–12, 2017.

[182] Masafumi Yamaguchi et al. Novel materials for high-efficiency iii–v multi-junction solar cells. *Sol. Energy*, 82(2):173–180, 2008.

[183] Alexis De Vos. Detailed balance limit of the efficiency of tandem solar cells. *J. Phys. D: Appl. Phys.*, 13(5):839, 1980.

[184] Suren A Gevorgyan, Morten V Madsen, Bérenger Roth, Michael Corazza, Markus Hösel, Roar R Søndergaard, Mikkel Jørgensen, and Frederik C Krebs.

Lifetime of organic photovoltaics: status and predictions. *Adv. Energy Mater.*, 6(2):1501208, 2016.

[185] William R Mateker and Michael D McGehee. Progress in understanding degradation mechanisms and improving stability in organic photovoltaics. *Adv. Mater. (Weinheim, Ger.)*, 29(10):1603940, 2017.

[186] Roar Søndergaard, Markus Hösel, Dechan Angmo, Thue T Larsen-Olsen, and Frederik C Krebs. Roll-to-roll fabrication of polymer solar cells. *Mater. Today*, 15(1-2):36–49, 2012.

[187] Gang Li, Rui Zhu, and Yang Yang. Polymer solar cells. *Nat. Photonics*, 6(3):153–161, 2012.

[188] Masahiro Hiramoto, Hiroshi Fujiwara, and Masaaki Yokoyama. p-i-n like behavior in three-layered organic solar cells having a co-deposited interlayer of pigments. *J. Appl. Phys.*, 72(8):3781–3787, 1992.

[189] Stephen R Forrest. The path to ubiquitous and low-cost organic electronic appliances on plastic. *Nature*, 428(6986):911–918, 2004.

[190] Mcgehee Group. http://web.stanford.edu/group/mcgehee/transfermatrix/.

[191] Ryan L Peck, Alexandre G Brolo, and Reuven Gordon. Absorption leads to narrower plasmonic resonances. *J. Opt. Soc. Am. B*, 36:F117–F122, 2019.

[192] Lukasz Janasz, Dorota Chlebosz, Marzena Gradzka, Wojciech Zajaczkowski, Tomasz Marszalek, Klaus Müllen, Jacek Ulanski, Adam Kiersnowski, and Wojciech Pisula. Improved charge carrier transport in ultrathin poly (3-hexylthiophene) films via solution aggregation. *J. Mater. Chem. C*, 4:11488–11498, 2016.

[193] Mina Baghgar, Joelle A Labastide, Felicia Bokel, Ryan C Hayward, and Michael D Barnes. Effect of polymer chain folding on the transition from h- to j-aggregate behavior in p3ht nanofibers. *J. Phys. Chem. C*, 118:2229–2235, 2014.

[194] Edwards T Niles, John D Roehling, Hajime Yamagata, Adam J Wise, Frank C Spano, Adam J Moulé, and John K Grey. J-aggregate behavior in poly-3-hexylthiophene nanofibers. *J. Phys. Chem. Lett.*, 3:259–263, 2012.

[195] Robert D Deegan, Olgica Bakajin, Todd F Dupont, Greb Huber, Sidney R Nagel, and Thomas A Witten. Capillary flow as the cause of ring stains from dried liquid drops. *Nature*, 389(6653):827–829, 1997.

[196] Nikolai G Khlebtsov. Extinction and scattering of light by nonspherical plasmonic particles in absorbing media. *J. Quant. Spectrosc. Radiat. Transfer*, page 108069, 2022.

[197] Jinan Zhai, Lanxin Ma, Wenbin Xu, and Linhua Liu. Effect of host medium absorption on the radiative properties of dispersed media consisting of optically soft particles. *Journal of Quantitative Spectroscopy and Radiative Transfer*, 254:107206, 2020.

[198] Jian Dong, Wenjie Zhang, and Linhua Liu. Discrete dipole approximation method for electromagnetic scattering by particles in an absorbing host medium. *Opt. Express*, 29(5):7690–7705, 2021.

[199] Michael I Mishchenko and Ping Yang. Far-field lorenz–mie scattering in an absorbing host medium: theoretical formalism and fortran program. *J. Quant. Spectrosc. Radiat. Transfer*, 205:241–252, 2018.

[200] Michael I Mishchenko, Janna M Dlugach, James A Lock, and Maxim A Yurkin. Far-field lorenz–mie scattering in an absorbing host medium. ii: Improved stability of the numerical algorithm. *J. Quant. Spectrosc. Radiat. Transfer*, 217:274–277, 2018.

[201] Chenxu Yu and Joseph Irudayaraj. Multiplex biosensor using gold nanorods. *Anal. Chem. (Washington, DC, U. S.)*, 79:572–579, 2007.

[202] Jakub Dostálek, Hana Vaisocherová, and Jiří Homola. Multichannel surface plasmon resonance biosensor with wavelength division multiplexing. *Sens. Actuators, B*, 108:758–764, 2005.

[203] RG Sobral-Filho, AM Brito-Silva, M Isabelle, A Jirasek, JJ Lum, and AG Brolo. Plasmonic labeling of subcellular compartments in cancer cells: multiplexing with fine-tuned gold and silver nanoshells. *Chem. Sci.*, 8:3038–3046, 2017.

[204] Vasile A Popescu and Anuj K Sharma. New plasmonic biosensors for determination of human hemoglobin concentration in blood. *Sensing and Imaging*, 21(1):1–13, 2020.

[205] Ashish Bijalwan and Vipul Rastogi. Gold–aluminum-based surface plasmon resonance sensor with a high quality factor and figure of merit for the detection of hemoglobin. *Appl. Opt.*, 57(31):9230–9237, 2018.

[206] L Genzel, TP Martin, and U Kreibig. Dielectric function and plasma resonances of small metal particles. *Zeitschrift für Physik B Condensed Matter*, 21(4):339–346, 1975.